MULTIPHYSICS MODELING OF THE SPARK PLASMA SINTERING (SPS) PROCESS

BY

MUHAMMAD LUQMAN

A Thesis Presented to the

DEANSHIP OF GRADUATE STUDIES

KING FAHD UNIVERSITY OF PETROLEUM & MINERALS

DHAHRAN, SAUDI ARABIA

In Partial Fulfillment of the
Requirements for the Degree of

MASTER OF SCIENCE

In

MECHANICAL ENGINEERING

MARCH 2014

KING FAHD UNIVERSITY OF PETROLEUM & MINERALS

DHAHRAN- 31261, SAUDI ARABIA

DEANSHIP OF GRADUATE STUDIES

This thesis, written by **Mr. MUHAMMAD LUQMAN** under the direction of his thesis advisor and approved by his thesis committee, has been presented and accepted by the Dean of Graduate Studies, in partial fulfillment of the requirements for the degree of **MASTER OF SCIENCE IN MECHANICAL ENGINEERING.**

Dr. NOUARI SAHEB

(Advisor)

Dr. ABUL FAZL M. ARIF
(Member)

Dr. ZUHAIR MATTOUG GASEM
Department Chairman

Dr. SYED SOHAIL AKHTAR
(Member)

Dr. SALAM A. ZUMMO
Dean of Graduate Studies

30/2/14

Date

Dedicated to my beloved parents, sisters and brothers.

ACKNOWLEDGMENTS

All praise belongs to ALLAH, the Almighty, who created the universe and sustains it; and Durud and Salam be on the last of all the prophets (صلي الله عليه وسلم) who made the truth prevail over falsehood and provided humanity with guidance for all times.

I sincerely acknowledge the support and facilities provided by King Fahd University of Petroleum & Minerals, Dhahran, Saudi Arabia.

I would like to express my deepest appreciation to my thesis advisor Dr. Nouari Saheb for his moral support and sincere advices; he continually and persuasively conveyed a spirit of adventure in regard to research. In addition to my advisor, I'm also grateful to my thesis committee members, Prof. Abul Fazl Muhammad Arif and Dr. Syed Sohail Akhtar for their valuable contributions, guidance, support and encouragement throughout my research. Furthermore, special thanks are due to Dr. Abbas Saeed Hakeem for his guidance and support in the experimental work.

I would also like to express my deepest gratitude to the faculty members of the Mechanical Engineering Department at KFUPM. Moreover, I'm deeply indebted to Mr. Abdullatif Hashmi and Mr. Sadaqat for their support and cooperation in the experimental work.

I would also like to express my sincere appreciation to my colleagues in the Mechanical Engineering department, especially Mr. Abdul Azeem & Mr. Najm-ul-Qadir for helping me in different aspects of the thesis' work. Additionally, I'd like to acknowledge my friends Waleed, Awais, Waseem, Umer, Nasir, Saad Khan, Hassaan and Uneb. Without their help, it would have been impossible for me to finish my M.S. study.

Last, but not the least, I would like to thank my parents for their endless love and support, who although far away from me, always close to my thoughts and heart. I would also like to thank my sisters and brothers for their moral support and encouragement.

TABLE OF CONTENTS

LIST OF FIGURES

LIST OF TABLES

NOMENCLATURE

A_{cr}	Material constant
C_p	Specific heat
P_L	Effective sintering stress
Q	Volumetric heat sources
$\dot{e}$	Shrinkage rate
k_T	Thermal conductivity
$\vec{q}$	Heat flux vector
r_o	Average particle radius
$\dot{\gamma}$	Shape change rate
δ_{ij}	Kronekar's delta
$\dot{\varepsilon}$	Steady-state creep rate
ε_{ij}	Strain rate components
σ_{ij}	Externally applied stress
B	Burger's vector
D	Diffusivity
E	Electric field intensity
J	*E*lectric current density
k	Boltzman's constant
n	Material constant
h	Heat transfer coefficient
T	Absolute temperature
t	Time
V	Electric potential
V_o	Applied voltage
W	Equivalent strain rate
α	Surface energy
λ	Electrical conductivity
μ	Shear modulus
ρ	Mass density
$\sigma(W)$	Effective stress
φ	Normalized shear viscosity modulus
ψ	Normalized bulk viscosity modulus
ε_r	Relative permittivity
ε_o	Permittivity of free space
∇T	Temperature gradient

ABSTRACT

Full Name : Muhammad Luqman

Thesis Title : Multi-Physics Modeling Of The Spark Plasma Sintering (SPS) . Process

Major Field : Mechanical Engineering

Date of Degree : March, 2014

Spark plasma sintering (SPS) is defined as a processing technique, which sinters materials using electric current in conjunction with uniaxial pressure. It offers several advantages over conventional techniques like achievement of near-theoretical density and nanocrystalline morphology in extremely shorter sintering durations, avoidance of abnormal grain growth, and clean sample surfaces due to interaction with gaseous plasma. However, the major drawbacks of SPS which are not observed in conventional sintering techniques include difficulty in sintering complex-shaped or large-sized samples, relatively large degree of inhomogeneity in mechanical properties, and charge accumulation especially in insulating powders. Hence in order to achieve the best processing results, it is obligatory to grasp a firm understanding of the kinetics of SPS process. Since experimental methods do not facilitate the in-situ measurement of sintering temperature, pressure, and relative density, one has to rely on computational techniques in order to get a better understanding of the process kinetics. These computational techniques are utilized in predicting the structure-property relationship of the material being sintered, and optimization of the process parameters in order to achieve the best mechanical properties without presence of inhomogeneity. The main

objective of the computational work done in this study is to develop a coupled electrical–thermal–mechanical Finite Element Model of the SPS process. This model has been used to study two different classes of materials – aluminum (an electrical conductor), and alumina (an electrical insulator), where a range of aspect ratios has been considered for each disk-shaped sample. In order to validate the results obtained via computational analysis, a small-scale experimental study is also conducted to determine the relationship between SPS process-parameters and the mechanical properties of sintered sample. Comparison of the results obtained from the computational model with those achieved from the experimental study, indicate that almost all the process parameters as well as mechanical properties are characterized by inhomogeneity within the sintered samples.

ملخص الرسالة

الاسم الكامل : محمد لقمان

عنوان الرسالة : متعدد الفيزياء نمذجة البلازما التكلس سبارك (SPS). عملية

التخصص : الهندسة الميكانيكية

تاريخ الدرجة العلمية : مارس 2014

يتم تعريف تكليس شرارة البلازما (SPS) كأسلوب معالجة، والتي تكلس المواد باستخدام التيار الكهربائي بالتزامن مع الضغط أحادي المحور. أنها توفر العديد من المزايا أكثر من التقنيات التقليدية مثل تحقيق الكثافة شبه النظرية، وتشكل البلورات النانونية في فترات تكليس قصيرة للغاية، متجنبة نمو الحبوب الغير طبيعية، وسطوح العينات النظيفة بسبب التفاعل مع غازات البلازما. ومع ذلك، فإن العوائق الرئيسية لتكليس شرارة البلازما التي لم تلاحظ في تقنيات التكليس التقليدية تشمل صعوبة في تكليس العينات ذو الاشكال المعقدة أو كبيرة الحجم، نسبيا درجة عالية من عدم التجانس في الخصائص الميكانيكية، وتراكم الشحنات خاصة في عزل المساحيق. وبالتالي من أجل تحقيق أفضل النتائج المعالجة، يجب الامساك بالفهم الراسخ لحركية تكليس شرارة البلازما. و بما أن الطرق التجريبية لا تسهل قياس درجة الحرارة و الضغط و الكثافة النسبية للتكليس أثناء اجراء التجربة، على المرء الاعتماد على التقنيات الحاسوبية من أجل الحصول على فهم أفضل للعملية الحركية. وتستخدم هذه التقنيات الحاسوبية في التنبؤ بعلاقة مميزات البنية للمواد الجاري تكليسها ، والاستفادة المثلى من معايير العملية من أجل تحقيق أفضل الخواص الميكانيكية في غياب عدم التجانس. الهدف الرئيسي من هذا العمل الحسابي في هذه الدراسة هو تطوير عناصر محدودة مقترنة كهربائيا وحراريا وميكانيكيا باستخدام عملية تكليس شرارة البلازما. وقد استخدم هذا النموذج لدراسة فئتين مختلفتين من المواد - الألومنيوم (موصل كهربائي) والألومينا (عازل كهربائي), حيث تم اعتبار مجموعة ذو نسب مختلفة من نسب العرض للطول لكل عينة على شكل القرص. من أجل التحقق من صحة النتائج التي تم الحصول عليها عن طريق التحليل الحسابي، أجرت دراسة تجريبية على نطاق ضيق لتحديد العلاقة بين عملية المتغيرات لتكليس شرارة البلازما والخواص الميكانيكية للعينة المتكلسة.

المقارنة بين النتائج تم الحصول عليها من النموذج الحسابي مع تلك التي تحققت من دراسة تجريبية، تشير إلى أن جميع المتغيرات وكذلك الخواص الميكانيكية تتميز بعدم التجانس في حدود العينات المتكلسة.

CHAPTER 1

INTRODUCTION

Spark Plasma Sintering (SPS) is a sintering technique which incorporates both uniaxial pressure and application of electric current to accelerate the sintering process. This technique offers various advantages over conventional sintering methods, e.g., faster heating rate, shorter sintering time, higher rate of powder densification, achievement of grain size in the nanocrystalline regime and near-theoretical density, cleanliness of near-surface particles by plasma ions, and avoidance of abnormal grain growth. The foremost advantage of SPS is achievement of near-theoretical density during sintering of ceramic powders characterized by high melting point and lower self-diffusion rate due to the existence of covalent bonding. However, the major disadvantage of this technique is the existence of thermal and mechanical gradient along the sample cross-section due to high heating rates, especially in case of ceramic and polymeric powders which are characterized by low values of electrical and thermal conductivity.

The fundamental mechanism of SPS is not well known. However, it is hypothesized that the interaction of electric current with the particles results in micro-sparks, which eventually leads to the removal of surface impurities and accelerates the surface and grain-boundary diffusion kinetics. A number of mathematical models, simulating the effect of SPS process parameters on the density evolution of the sample, have been proposed and implemented in Finite Element-based softwares including ABAQUS, ANSYS, CFD and COMSOL Multiphysics. In the present work, COMSOL Multiphysics has been used to simulate the electrical, thermal and mechanical

gradients along the cross-section of aluminum and alumina powders, sintered using the SPS process under a variety of heating rates.

1.1 SPARK PLASMA SINTERING (SPS)

1.1.1 Instrumentation

The SPS machine is composed of a uniaxial press, vacuum chamber (or controlled atmosphere), two punch electrodes, a die, a DC pulse generator, a controller/computing unit, and sensors to monitor the temperature, pressure and punch position. A generalized schematic highlighting the primary SPS instrumentation is shown in Figure 1.

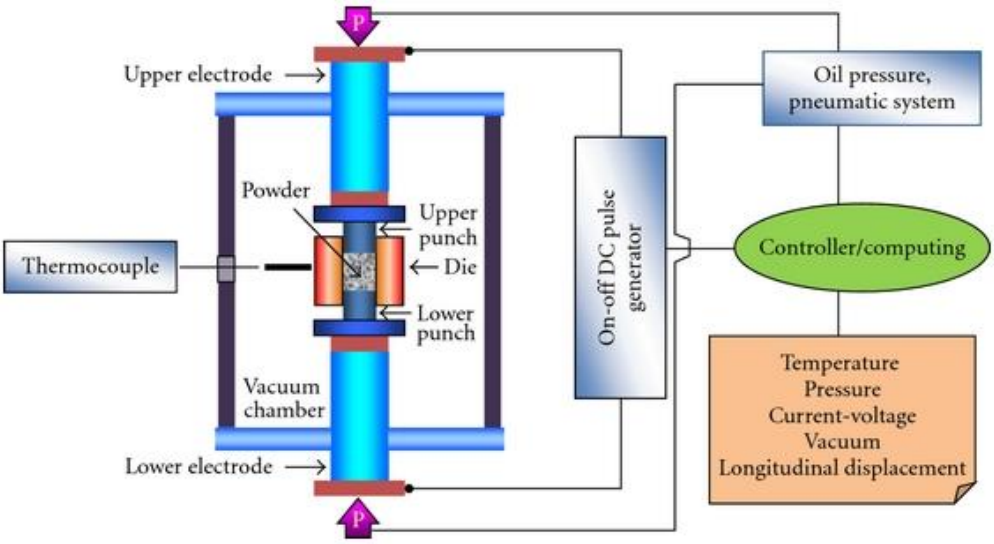

Figure 1: Schematic of SPS Process [1]

1.1.2 Sintering procedure

In SPS process, an electrical current is applied concurrently with a uniaxial mechanical pressure to sinter/consolidate powders for specific applications with preferred density and configuration. The applied mechanical load and electrical current can be kept

constant during the course of the sintering cycle, or can be varied during the subsequent densification stages. The powder to be sintered is placed in a die and then heated via application of electrical current. For electrically conducting powders, the following types of dies can be used:

- Electrically conducting die,
- Electrically insulating die (as the powder itself guarantees the electrical circuit closure), or
- A conducting die having non-conducting coating on the interior surface.

For insulating powders, the die material must be conducting in order to fulfill the requirement of a closed electrical circuit to initiate the sintering process. For the same reason, all the other components of the system, i.e., electrodes, blocks, spacers, and plungers etc. need to be made of an electrically conducting material, e,g. stainless steel, copper, graphite, etc.

1.1.3 Electrical transport in SPS process

The flow of electrical charge through the die-specimen system in SPS process relies primarily on the power supply characteristics, and thus can be characterized by different intensities and waveforms. However, irrespective of the waveform of the electrical current, the root mean squared value of the instantaneous intensity of the applied current can be expressed as:

$$I_{RMS} = \sqrt{\frac{1}{\tau}\int_{t}^{t+\tau} I^2(t)dt}$$

Where; "*I*" denotes the instantaneous current, and "*t*" represents the sampling time. Generally, in case of DC power supply, the applied voltage can be only a few volts (e.g. 0-10 V) and the current can be a several thousand Amperes (e.g. 1000-10,000 A). In case of pulsed DC power supply, the ON and OFF timings are usually in the range of a few milliseconds. The different types of pulse patterns that can be observed in the DC power supply are shown in Figure 2.

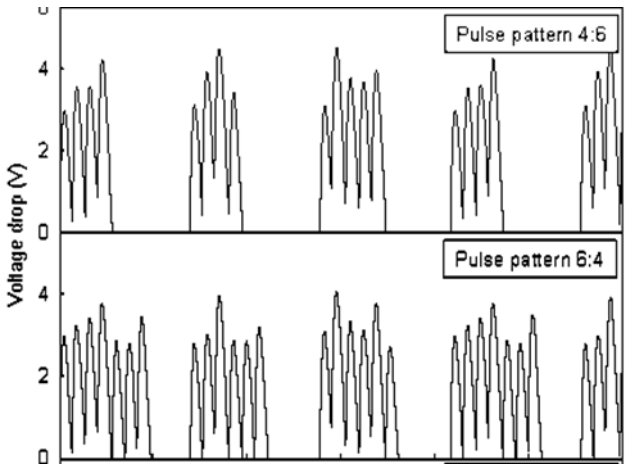

Figure 2: Different pulse patterns in pulsed DC power supply [2]

1.1.4 Heating mechanism in SPS process

The foremost difference between heating mechanism in SPS process and other sintering techniques is that internal heat generation occurs exclusively due to the Joule effect of the DC current. The total heat generation in SPS process is a combination of two components:

a. Heat generation in the die and punches, and

b. Heat generation in the sample

In case of a conducting powder sample, the sample is heated both by the heat generated in the sample itself as well as by conduction of heat from electrodes and the

die. However, insulating powders are heated only by the conduction of the heat generated in the dies and the electrodes.

Although, the true mechanism of heat generation in SPS is still unclear, the heat generated in SPS is hypothetically attributed to the micro-spark discharge (plasma heating) in the gaps between neighboring powder particles, resulting in neck formation, which establishes a path for the conduction of electrical current through the particles. It is then followed by Joule heating, originating from the resistance of the material to the electrical current flowing through it, resulting in the coarsening of the grains (see Figure 3). As this heat generation has a localized character and almost uniform distribution, it allows rapid temperature rise and drop, which prohibits coarsening (growth) of the material grains.

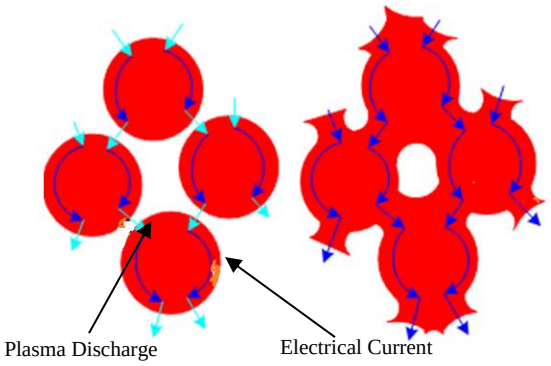

Figure 3: SPS Sintering mechanism; Plasma heating (left), & Joule heating (right) [3]

It is worth mentioning here that the only heat generation mechanism in the SPS process which is supported by experimental validation is the Joule effect. All other phenomena that are associated with the current flow – plasma formation, generation of sparks, high local temperature at the contact surfaces of the particles, etc. – may take

place simultaneously with the Joule effect as secondary mechanisms, but lack experimental evidence [4].

1.1.5 Loading mechanism in SPS process

The mechanical load, in SPS process, is usually applied uniaxially. However, a few experimental setups have recently incorporated the application of isostatic or quasi-isostatic pressure to the sample during sintering. SPS machines capable of applying ultra-high isostatic pressures up to 8 GPa have been marketed during the last few years.

Plastic deformation of the powder particles due to applied pressure, combined with surface-, bulk-, and grain-boundary diffusion, result in the densification of the powder compact to over 99% of its theoretical density, as shown in Figure 4. This increase in the density has been observed to be accompanied by corresponding increase in the electrical conductivity of the sample [5].

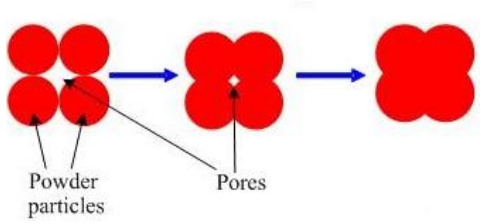

Figure 4: Densification mechanism in SPS [3]

1.1.6 Advantages of SPS

The major advantages of SPS process over conventional sintering methods can be summarized as:

- Quicker heating rate,
- Reduced sintering temperature,

- Minimum holding time,
- Possibility to consolidate difficult-to-sinter-powders,
- No need of cold compaction,
- No need of sintering aids,
- Less sensitivity to initial powders' characteristics,
- Possibility of production of fully sintered parts with near-theoretical density,
- Near-net shape production of parts,
- Minimal rejection rates of sintered parts, and
- Significant comparative advancements in the properties of sintered materials.

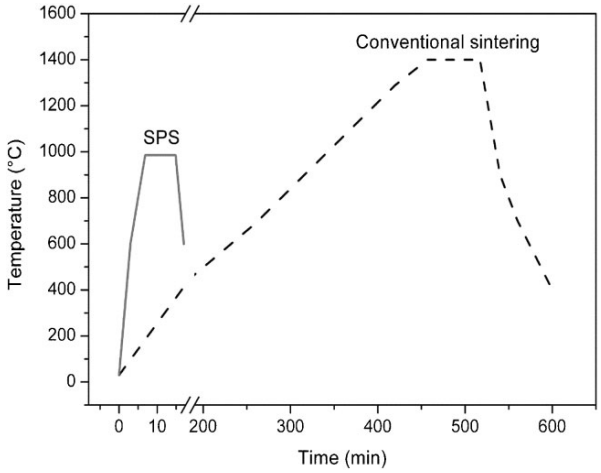

Figure 5: Comparison of sintering time and temp. of SPS and conventional sintering [6]

Particularly, shorter sintering times and lower sintering temperatures facilitate the sintering of metastable and/or nanocrystalline powders to near-theoretical density, with cleaned grain boundaries and negligible retention of metastability or grain growth [2]. The possibility of production of near-net shape parts using SPS process, coupled with minimal rejection rates, is an indication of significant cost savings owing to generation of minimum material scrap, and negligible subsequent machining

requirements. Most importantly, this cost-effectiveness is supplemented by the production of high quality parts at lower processing costs. In addition, SPS has demonstrated substantial potential for swift transfer of technology from the lab-scale to the commercial scale.

1.1.7 Difficulties in SPS process

SPS, besides offering extremely competitive advantages over the conventional methods, poses certain drawbacks as well. One of the problems experienced in SPS process is the attainment of uniform electrical conductance through the sample, and hence the achievement of an even temperature distribution. The temperature distribution in the sample is dependent upon the current distribution, which is in turn relies heavily on the degree of material homogeneity inside the powder sample. In addition, large spatial density variations, particularly at the initiation of current flow, can cause localized overheating or, sometimes, even sample melting. Hence, the majority of powder samples to be sintered are compacted in either cylindrical or rectangular shapes, which leads to minimal density variations during the SPS process. It is also noteworthy to indicate that even in the consolidation of parts having even thickness in the perpendicular direction of the applied uniaxial pressure, difficulties are faced in achieving uniform temperature distribution.

1.1.8 Differences between conventional and non-conventional sintering mechanisms

In SPS process, the rate of heating depends on the geometry of the sample-die assembly, its electrical and thermal properties, and the electrical power supply. Heating rates as high as 1000 K/min have been reported which eventually result in

variation of processing time from a few seconds to several minutes, depending on the part size, type of material, equipment capacity, and configuration.

In conventional sintering techniques, the die is heated by radiation (or sometimes convection as well, if applicable) from the surrounding furnace through external heating elements. Hence, the sample is heated by the conduction of heat from the external surface of the die to the sample, which necessitates longer sintering times to achieve a feasible value of sintered density. Moreover, a huge amount of heat is expected to be wasted since a very small volume of sample is heated indirectly from a comparatively much larger volume of the outside high temperature environment. In contrast, the only source of heat generation in SPS is the die-specimen system, thus facilitating highly controlled heat transfer to the powder sample with minimal losses, especially when the electrical current is applied for a very short span of time (order of milliseconds), or the die is made of an electrically insulating material.

1.2 MOTIVATION

It can be concluded from the foregoing discussion that the various advantages offered by the SPS process over conventional sintering techniques are counteracted by drawbacks such as non-uniform distribution of stress and temperature in sintered bodies, especially those having large sizes and/or complex shapes. Hence, a comprehensive understanding of the sources which lead to the thermal and mechanical gradients along the cross-sections of spark-plasma sintered parts is required, in order to produce large complex-shaped parts with homogeneous microstructures and mechanical properties. However, owing to the limitation of in-situ monitoring of the dynamics of the SPS process, ever-increasing research efforts are currently being

expanded in order to exploit appropriate computational methods for effective simulation of sintering kinetics. The majority of research studies conducted so far has, however, focused primarily on the dynamics of the SPS process itself; a negligible amount of literature exists which supports the simulation of SPS specifically for parts with large size and/or complex geometries.

1.3 OBJECTIVES

The major objectives of this study can be outlined as:

1. Develop a multi-Physics Model for SPS process with the capability of predicting electrical, thermal and structural parameters of the process.
2. Validate the model using previously published works and/or experimental studies.
3. Use the developed model to study the effect of geometrical parameters on SPS process.

CHAPTER 2

LITERATURE REVIEW

On SPS process, uptill now, there are numerous modeling attempts available in literature. Most of them were aimed for two purposes: 1) to study the role of the assumed parameters on the process and (2) to explain the findings in this method for the processing of different materials. Thus, an important objective of these studies was to provide a basic understanding of the SPS process [2]. In addition, recently some simulation studies are aimed at the optimization and control of the process parameters as well as how to use the process for more shapes and sizes of the products.

In modeling studies, scientists and researchers used many different approaches: some used mathematical methods only [4-5] while others used some commercially available softwares like ANSYS [6-8], ABAQUS [9-11], MATLAB [7], COMSOL Multiphysics [13-19], etc for modeling the SPS process.

A significant number of modeling studies have been carried out in recent years. Models of the SPS technique can be sub-divided into several sub-models each covering a different physics of the process. These include the electrical, thermal, and structural models. The following sections discuss the state of the art for each of these models.

2.1 THERMAL-ELECTRICAL MODELING

Several different attempts have been made to develop numerical and computational models covering the thermal and electrical aspects of SPS. They are discussed below in chronological order in the following paragraphs.

Raichenko and Chernikova [8] and Raichenko et al. [9] described the joule heat generation and the accompanied heat transfer quantitatively in a punch-sample-punch system without a die. They took into account only axial (1D) thermal balances which were coupled by using continuity boundary conditions at interface contacts (see Figure 6).

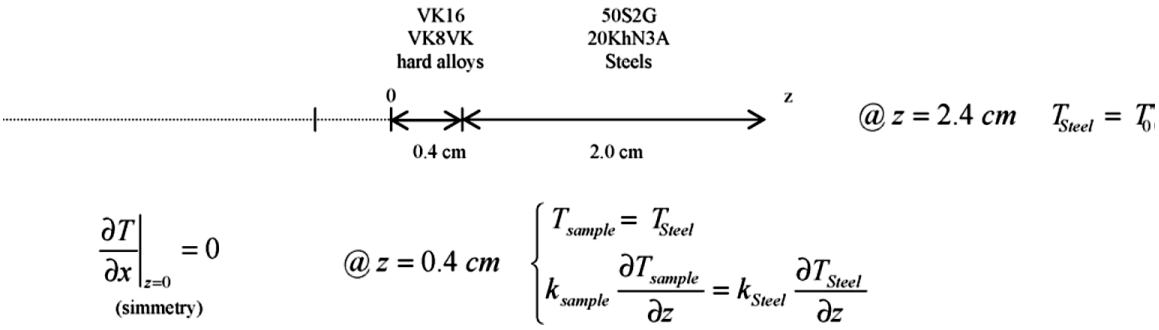

Figure 6: Integration domain and boundary conditions of the model proposed by Raichenko and Chernikova [9].

Also, to obtain the analytical solution of the model, they assumed thermo-physical properties (like thermal conductivity, thermal capacity, density and electric resistivity) and the current density to be constant. Moreover, in their studies, they calculated the temperature for a solid-state process under the conditions: 1) the side surfaces to be thermally insulated and 2) there were no contact effects. Also, they didn't consider shrinkage and thermal expansion in the direction of current passage. In their

conclusions they mentioned that the temperature depends not only on the axial coordinates but also on the radial coordinates [8].

Yoneya et. al. [10] presented a 2D numerical model (depicted in Figure 7 – i.e. die, sample and the portion of punches that is inside the die) based on the method of fundamental solutions, coupled with the Fourier transformation, to address current density and Joule heat distribution in the die (graphite) and specimen (copper) (see Figure 7). Their aim was to obtain temperature and electric potential profile in the pulse discharged sintering process. In this study, they found that the temperature in the system is controlled by the heat conductance from the punch, where a large Joule heat generation is observed due to its least cross-sectional area, without depending on the sample properties. They also reported that the calculated temperature in the sample is relatively uniform. In addition, they found that the higher the electrical conductivity of the sample, the more concentrated will be the electric current density in the sample and hence the current flow will be reduced in the die accordingly.

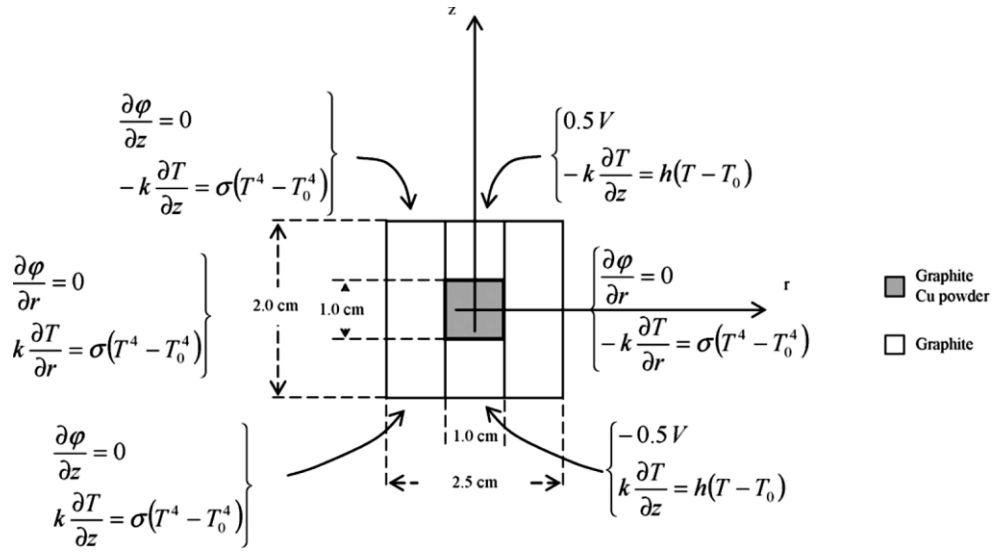

Figure 7: Integration domain and boundary conditions of the model proposed by Yoneya and Ikeshoji [10]

Yucheng et. al [11] presented 1D and 2D mathematical models in cylindrical coordinate system for sintering in SPS to calculate the temperature distribution in the sample at steady state. They used constant thermo-physical properties, continuity boundary conditions at interfaces and TiB2/BN as exemplary sample material considering its electrical conductivity almost equal to the die made of graphite thereby ignoring the difference in the current density in the system. Their analysis was based on the steady state conditions. From their study they reported that there exists the temperature difference in the sample which can be reduced by increasing the thermal conductivity of the sample. They also reported a qualitative agreement between the model and the experimental data.

Keum et. al. [12] modeled relatively high temperature gradient in radial direction for the SPS of Alumina powder (electrically insulator) compact of 2 cm diameter in steady state. They used FEM to solve thermal balance with joule heat generation and heat

conduction to get the temperature distribution only in the radial direction. In their model, they haven't provided the system geometry and thermo-physical properties. They also haven't stated the boundary conditions clearly. They also have calculated the grain growth of sintering powder using Monte Carlo simulations on the basis of temperature distribution. In their case study, they found that the temperature at the sample's center is always less than the outer surface. They attributed this observation to the electric resistivities of the sample and the die causing the flow of current to adapt its path accordingly. Therefore, in such cases the sample is basically heated by the conduction of heat from the die. Matsugi et. al [13] compared the behavior of pre-sintered Alumina (electrically insulator) and Titanium (electrically conductor) powders in SPS at steady state with that of the model developed for the system depicted in Figure 8. They used Finite Difference Method to develop their model. This is the first ever model which incorporated the applied mechanical load in their model. They used the thermal balance, the Joule heat generation and the heat conduction coupled with the conservation of the current density for the system. They used effective thermo-physical properties (determined from the corresponding full dense material properties and some empirical functions – functions of temperature and applied pressure) to incorporate the effect of the varying relative density of the compact.

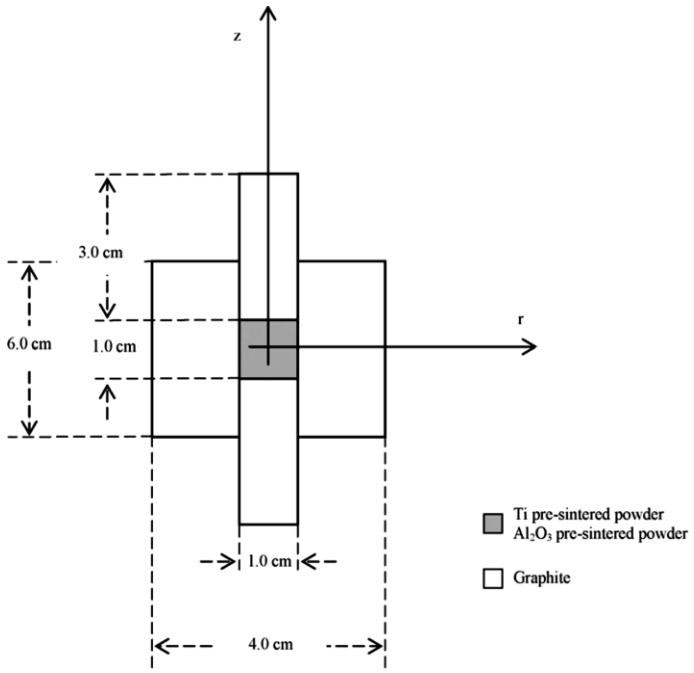

Figure 8: Integration domain of the model proposed by Matsugi et al [13]

Zavaliangos et. al. [14] conducted experiments supported by Finite Element simulations using ABAQUS to characterize the temperature distribution in the die/punch/sample setup and also its evolution during SPS. In their experiments, they used a pressure of 15 MPa and a pulsed DC having a square wave pattern of 36 ms ON and 6 ms OFF. In FE Simulations, they used evacuated chamber and hence they considered the radiation to be the only heat transfer mode. They also incorporated the thermal and electrical contact resistances at the interfaces for imperfect contacts. In their comparison of the simulated results with the experimental ones, they reported a good agreement between them. They found significant temperature gradients in the sample in the radial as well as axial directions. They also reported that the highest temperature is experienced at the punches while the minimum is at the outer surface of the die. Also, they found increase in temperature difference between maximum and minimum temperatures with increase in temperature.

Vanmeensel et. al. [15] modeled temperature distribution and current density in the die/punch/sample setup in SPS using FE calculations supported by in-situ thermal and electrical input data. Using ANSYS along with some other FE code, they performed case studies for an electrically insulator material (ZrO2) and an electrically conductor material (TiN). They used graphite sheets in all the contacts to ensure them to be conductive electrically as well as thermally. They found that the radial temperature gradient was much larger in case of the electrically conducting material as compared to the one that is electrically insulator material. Their study comprised of the thermal-electrical phenomenon only. They used temperature dependent properties for the materials and validated their results using experiments. Tamburini et. al. [16] carried out modeling and experimental analyses to investigate temperature and current distributions in SPS for two different classes of materials; one electrically being highly conductive (copper) whiles other highly insulating (alumina). They used finite volume CFD-ACE+ software package and evaluated current and heat generation gradients for both cases in the radial as well as in the axial directions. They used ideal contacts (i.e. zero resistance) at all the interfaces and the sample material in both cases was considered to be fully dense thereby resulting in zero mechanical displacement in the assembly. As expected, they found that the alumina sample didn't carry any current and so, was thermally heated from the die. They reported that the radial gradients result in significant differences in temperature between the surface of the graphite die and its center which is in agreement with experimental measurements. They also concluded that the axial gradients do have influence on the product's homogeneity.

Yucheng et. al. [17] presented a numerical model of SPS for the temperature field which was based on the simplification of the temperature rising process. They reported that the highest temperature region in the system is in the punch and therefore the heat flows from the punches to the die and the sample. Moreover, the temperature at the center of the sample is much higher than the temperature at the edges in the radial direction while in the axial direction, the temperature of the center was found to be lower than the edges of the sample. They also reported that as the sintering process proceeds, the temperature difference increases till the end of the heating phase. McWilliams et. al. [5] implemented a fully coupled thermal-electrical model of the SPS system in ABAQUS. This model considered conduction, convection, and radiation heat transfer mechanisms. They considered the temperature dependent electrical and thermal conductivities for both the specimen (Tungsten) and tooling (graphite) materials in their study. They considered specimen as a fully dense material. They carried out a parametric study of the geometries of the die and the punch. Their aim was to quantify the effect of each on the thermal and electrical gradients in the system and to maximize the performance of the machine with respect to maximum achievable temperature and energy efficiency. They didn't include the effect of pulses in their simulations. They concluded from their results that the gradients developed during SPS are complex and are dependent on the exact system configuration. Also, they did parametric study on a cylindrical as well as rectangular specimen and explored the gradients present in the sample. They found that the power required to achieve a given temperature at the specimen's center has a direct relationship with the

height of the die (see Figure 9). It is because of the fact that the height of the die has a direct relationship with the volume to be heated for sintering.

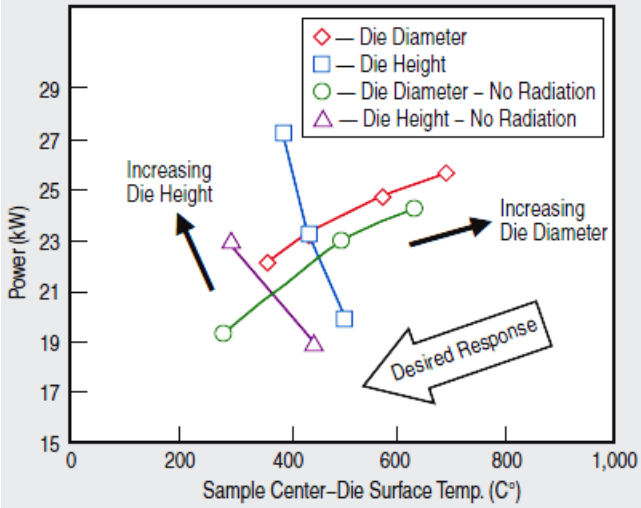

Figure 9: Simulation results for die diameter and die height at a sample center temperature of 1,800°C. Solid points represent simulations including radiation, and hollow points are simulation results with die wall radiation blocked. [5]

In 2006, Oleysky et. al. [18] developed a constitutive model for SPS in which they incorporated various mechanisms of material transport. They analyzed jointly the contributions of external load, sintering stress (surface tension) and electromigration to sintering shrinkage. They reported that the electromigration-related material flux can be a significant component of the electric-current-accelerated diffusion. They also designed an SPS mechanism transport map for aluminum powder. They validated their results in terms of shrinkage kinetics by comparison with the experimental data on SPS of Alumina powder. Maizza et. al. [19] developed a FE model (using COMSOL Multiphysics' AC/DC Module) for SPS which included a moving mesh technique to account for the change in the contact resistance due to punch sliding and sintering

shrinkage. They did their study (for WC) using a constant pressure of 20 MPa and three different currents, 1900, 2100 and 2700 A to investigate the effects of the heating rate on the hardness and microstructure in the radial direction. They established a direct relationship between the compact microstructure and both the heating rate and the sintering temperature. Huang et. al. [20] did their study (only thermal) using WC-12 wt% Co powder mixtures doped with VC. They supported their experiments by FE simulations using ANSYS to simulate the temperature distribution in SPS of WC-Co powder and to optimize the set-up in order to minimize the thermal gradients. They used fully dense materials in their simulations. They reported that using an insulation of carbon felt surrounding the graphite die set-up can homogenize the radial temperature gradient inside the sintering powder.

Recently, Voisin et. al. [21] conducted a very good study comprising of two very important aspects: the direct sintering of near-net shape and large samples and homogeneity and control of temperature in the samples. They addressed the temperature evaluation and its homogeneity in the samples consolidated by the SPS process. Their aim was to achieve good microstructural homogeneity along with full densification. For this purpose they sintered samples of different sizes, the largest sample being 100mm in diameter and 60mm in height, using three different facilities which were differing by their size and shape. They used a structural change, activated in a TiAl alloy, as an indicator of the temperature of the sample and used COMSOL – an FEM based commercial software – to evaluate the temperature in the set-up at each point. In their FEM studies, they considered only thermal and electrical aspects using the code developed by Mondalek et. al. [22]. They reported a good agreement b/w

simulated and experimental results. They found better homogeneity in the samples prepared in larger machines or when alumina discs are used to isolate the sample. On the basis of this expertise in temperature control, they densified complex shaped samples (see Figure 10) successfully.

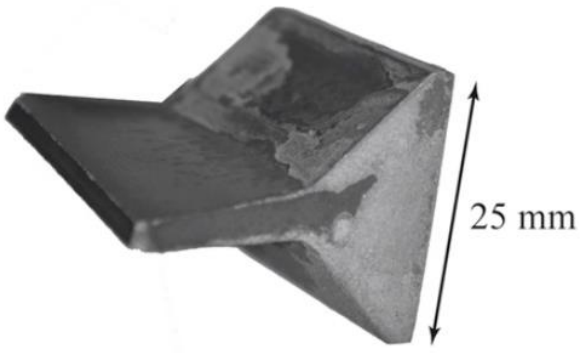

Figure 10: Complex shaped part sintered by Spark Plasma Sintering [21]

Pavia et. al. [23] investigated the controlling parameters of the SPS process using measurements of voltage, current and temperature at different points of the system. In their studies they found that the thermal conductivity and the electrical resistivity of all the elements are key parameters. These parameters strongly affect the current in the system, and hence the distribution of temperature in the whole SPS system. Giuntini et. al. [24] presented a paper which demonstrates the application of a 3D coupled thermal, electrical and mechanical FE macro-scale model of SPS to SPS tooling overheating – a real problem faced during SPS process. They analyzed the overheating phenomenon by varying the tooling geometry; by modeling numerous tooling arrangements involving step-wise increasing radii of disk-shape spacers. The main objective of their study was to obtain spatial temperature distributions in the SPS system including dies, punches and spacers; to identify the peak temperatures and their

respective timing, and to propose a better SPS tooling arrangement which eliminates the overheating problem. They considered heat transfer, joule heating, mechanical conditions, and densification in their model, utilizing COMSOL. They carried out the application of a FE method to a wide range of SPS processes, along with more specific optimization of the SPS tooling design while dealing with overheating phenomena.

2.2 STRUCTURAL MODELING

Cincotti et. al. [25] addressed the modeling of SPS apparatus using COMSOL Multiphysics. Initially they considered the SPS behavior of the system with the absence of powders permitting the detailed analysis of the system from the electrical point of view. They did their studies using cylindrical shaped specimen having isotropic material properties and ignored the contact resistances in their studies. They also highlighted the importance of taking root mean squared electric current for the quantitative determination of the Joule's effect. Wang et al. [26] in addition to elucidating the temperature and electrical potential distributions, also simulated the stress distribution in SPS experiments and found that stress gradients, which depended on materials' properties (coefficient of thermal expansion, CTE, and modulus), were larger than thermal gradients. Stress gradients, both in the vertical and in the radial directions, were found to be significant, especially for materials with a high CTE, which indicates that simple calculations of stress on the basis of the force and sample area may not be valid. A finite element model was developed to simulate three-way coupling of thermal, electrical and mechanical behavior of electrical current activated sintering. In addition to the direct simulation of the evolution of electrical potential and temperature in the system, the model is capable of simultaneously calculating the

displacement fields and the stress distributions. Experimentally measured temperatures were found to be in excellent agreement with simulations. The displacement and stress distributions were found to depend on the material properties. In the copper system, owing to its large thermal expansion, the steady-state vertical stress has a gradient of 33% across the sample at a 1000 A current input (700 ^{o}C); the radial and angular stresses are significant and have larger gradients.

McWilliams et. al. [27] investigated the effect of conduction path on the evolution of density and reported that the sintering behavior of sample in SPS can can be affected by the variation in its local density. Grasso et. al. [28] investigated the effects of applied pressure on the distribution of temperature in the die-punch-sample graphite system by combining computational and experimental studies. From their results, they inferred that the temperature difference between the outer surface of the die and the sample, and the peak temperature progressively decrease with increase in applied pressure from 5 to 80 MPa. They attributed this behavior to the strong variation in the thermal and electrical contact resistances at the punch/die interface due to punch Poisson deformation. They also investigated the effect of pressure on the homogeneity of tungsten carbide sample sintered with SPS, experimentally as well as by modeling. In their studies, they discussed the effect of pressure on residual porosity, grain growth and hardness distributions in the radial directions. They took into account the change in the contact resistance due to shrinkage in the sample and the concomitant punch sliding. They also reported that increase in the sintering pressure results in a decrease in the sintering temperature.

The literature review done in this work is summarized in the following table:

Table 1: Summary of the literature review.

S. No	Author, Year	Analysis Method/ Software		Physics				Material's assumptions				Geometry		Results		
			Transient	T	E	M		Material Used	Structural behavior	Properties		Size	Shape	E	T	M
						Stress	Shrinkage			Temp. dependent	Structure dependent					
1	Raichenko et. al., 1989	Mathematical	Yes	Yes	No	No	No	VK16 hard alloy	Pore free	No	No	No	No	No	Yes	No
2	Yoneya et. al., 2001	Numerical	Yes	Yes	Yes	No	No	Copper	---	Yes	---	No	No	Yes	Yes	---
3	W. Yucheng et. al., 2002	Mathematical	Yes	Yes	No	No	No	---	---	---	---	No	No	No	Yes	---
4	K. Matsugi et. al., 2003	Finite Diff. Method	No	Yes	Yes	No	No	Titanium & Alumina	---	Yes	---	No	No	No	Yes	No
5	K. Vanmeensel et. al., 2005	ANSYS	Yes	Yes	Yes	No	No	TiN & ZrO2	---	Yes	---	No	No	Yes	Yes	No
6	A. Cincotti et. al., 2007	COMSOL Multiphysics	Yes	Yes	Yes	No	No	Graphite	Isotropic, elastic	Yes	No	No	No	Yes	Yes	No
7	B. McWilliams et. al., 2008	ABAQUS	Yes	Yes	Yes	Yes	Yes	WC-Co	Fully dense	No	No	No	No	No	Yes	Yes
8	G. Antou et. al., 2008	COMSOL Multiphysics	Yes	Yes	Yes	Yes	No	ZrC, ZrCO	Fully dense	Yes	No	No	No	Yes	Yes	Yes
9	F. Mechighel et. al., 2008	COMSOL Multiphysics	Yes	Yes	Yes	Yes	No	Copper & Alumina	Elastic	Yes	No	No	No	Yes	Yes	Yes

10	D. Tiwari et. al., 2009	MATLAB + ABAQUS	Yes	Yes	Yes	No	No	Graphite	---	Yes	No	No	No	Yes	Yes	No
11	N. Chennoufi et. al., 2009	---	Yes	Yes	Yes	No	No	Ni-Ti	Dense solid	Yes	No	No	No	Yes	Yes	No
12	G. Maizza et. al., 2009	COMSOL Multiphysics	Yes	Yes	Yes		Yes	WC	Porous	Yes	No	No	No	Yes	Yes	Yes
13	S. Muñoz et. al., 2010	ANSYS	Yes	Yes	Yes	Yes	No	Alumina, Copper	Elastic, Solid	Yes	No	No	No	Yes	Yes	Yes
14	P. Mondalek et. al., 2010	CimLib	Yes	Yes	Yes	No	No	TiAl & Alumina	---	Yes	No	No	No	Yes	Yes	No
15	G.Mol´enat et. al., 2010	COMSOL Multiphysics	Yes	Yes	Yes	No	No	TiAl, Alumina & SiC	---	Yes	No	No	No	No	Yes	No
16	C. Wang et. al, 2010	COMSOL Multiphysics	Yes	Yes	Yes	Yes	Yes	Alumina	Elastic, Solid	Yes	Yes	Yes (only radius)	No	No	Yes	Yes
17	C. Wolff et. al., 2011	ABAQUS	Yes	Yes	Yes	No	Yes	Lead & Boron	Porous, Elastic-thermo-visco-plastic	No	Yes	No	No	No	Yes	Yes
18	Y. Song et.al., 2011	MARC	Yes	Yes	Yes	Yes	Yes	Iron	Thermal visco-plastic	No	Yes	No	No	Yes	Yes	Yes
19	T. Voisin et. al., 2012	COMSOL Multiphysics	Yes	Yes	Yes	No	No	TiAl	---	---	---	Yes	Yes	No	Yes	Yes
20	S. Wei et. al., 2012	---	Yes	Yes	Yes	Yes	No	FGM (Ti, TiB)	Isotropic dense solid	Yes	No	No	No	No	Yes	Yes

21	E. A. Olevsky et. al., 2012	COMSOL Multiphysics	Yes	Yes	Yes	Yes	Yes	Alumina	Porous, viscous	Yes	Yes	Yes (constant h/r)	No	Yes	Yes	Yes (shrinkage only)
22	S. Muñoz et. al., 2012	ANSYS	Yes	Yes	Yes	Yes	No	Alumina, Molybdenum	isotropic dense elasitc solid	Yes	No	Yes (only radius)	No	Yes	Yes	No
23	A. Pavia et. al., 2013	COMSOL Multiphysics	Yes	Yes	Yes	No	No	Alumina, Manganese	Fully dense	Yes	No	No	No	Yes	Yes	No
24	***Luqman***	***COMSOL Multiphysics***	***Yes***	***Yes***	***Yes***	***Yes***	***No***	***Aluminum, Alumina***	***isotropic, elastic solid***	***Yes***	***No***	***Yes (height wise)***	***No***	***Yes***	***Yes***	***Yes***

The main contribution of this study will be in 1) the studies regarding the distribution of different physical quantities (computational as well as experimental quantities) in the axial direction, & 2) the study of different parameters with respect to the size of the sample.

CHAPTER 3

EXPERIMENTAL STUDY

3.1 INTRODUCTION

Our experimental study consisted of sintering of some adequate number of samples using SPS followed by its study using SEM, and micro-hardness tester. Our aim of this experimental study was to know the homogeneity in microstructure and in the hardness at different positions (in axial as well as the radial direction) in the sample. The reason for this is that that the microstructure and mechanical properties of materials are representative of the sintering parameters.

In our study, we have used two materials: pure aluminum and pure alumina. The study starts with the characterization of the received materials followed by their spark plasma sintering. The sintered samples were then tested with micro-hardness tester and Scanning Electron Microscopy. The experimental work is carried out using the facilities available at the department of Mechanical Engineering and Center of Excellence in NanoTechnology (CENT) at KFUPM. The details of this work follow in the following paragraphs.

3.2 EXPERIMENTAL TECHNIQUES

3.2.1 Particles' Size Analysis

The particles' size analysis was done using Dynamic Light Scattering (DLS) technique incorporated in equipment from Microtrac (Turbotrac). The basic principle of DLS: the sample is illuminated by a laser beam and the fluctuations of the scattered light are

detected at a known scattering angle "θ" by a fast photon detector. From a microscopic point of view the particles scatter the light and thereby imprint information about their motion. Analysis of the fluctuation of the scattered light thus yields information about the particles. Experimentally, one characterizes intensity fluctuations by computing the intensity correlation function, whose analysis provides the diffusion coefficient of the particles (also known as diffusion constant). The diffusion coefficient "D" is then related to the radius "R" of the particles by means of the Stokes-Einstein Equation:

$$D = \frac{kT}{6\pi R\eta}$$

Where; "k" is the Boltzmann-constant, "T" the temperature and "η" the viscosity.

3.2.2 X-Ray Diffraction

X-Ray diffraction analysis is basically carried out to identify the phases and its proportion present in the sample. X-Ray Diffraction analysis was carried out using the desktop X-Ray Diffractometer from Rigaku, Japan. The principle of X-Ray Diffraction is briefly explained in the following lines:

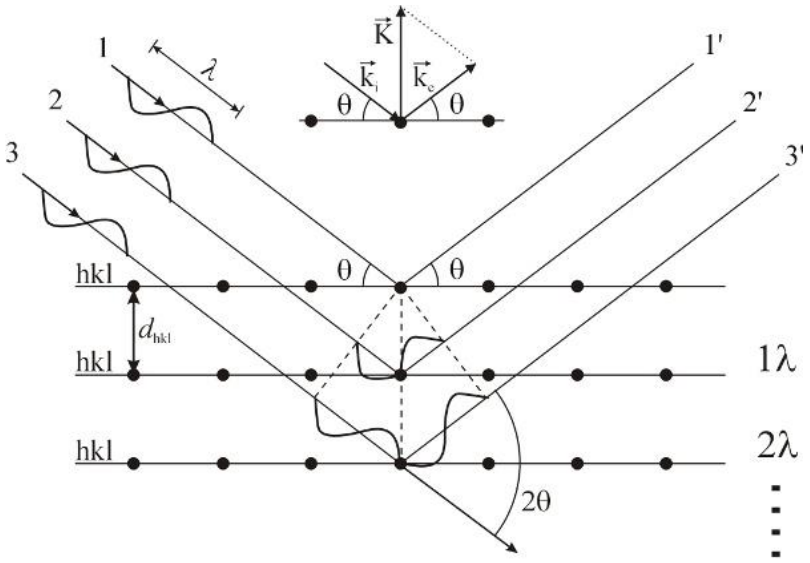

Figure 11: Schematic of X-Rays diffraction

X-rays are electromagnetic radiations with their wavelength in the order of magnitude of the interatomic distances in solids. Therefore, X-rays are frequently applied to study the internal (crystalline) structure of materials. An X-ray beam impinging on a crystal is scattered in all directions by the atoms of the crystal. In some directions, an increased intensity is observed due to the constructive interference of the scattered waves. The conditions for constructive interference are easily derived from the simple geometrical picture for the scattering of an X-ray beam by planes of atoms in a crystal (see Figure 11). Imagine the X-ray beam of wavelength "*λ"*, incident on the crystal at an angle "*θ"* with respect to equidistant "*hkl"* lattice-planes, with interplanar distance "d_{hkl}". Constructive interference will be observed only for those X-rays that are reflected from the lattice planes at the specular angle i.e. if the path length difference between X-rays scattered from different *hkl*-planes is an integral multiple of the wavelength. This condition is summarized in the Bragg law:

$$n\lambda = 2d_{hkl}\sin\theta$$

Where "n" is any integer, "λ" is the X-rays' wavelength, "d_{hkl}" is the interplanar distances and "θ" is the angle of diffraction. Furthermore, X-ray diffraction can be conveniently used to determine the average size of the nano-crystallites[1] in nano-crystalline bulk materials. For this, Paul Scherrer gave an equation known as Scherrer equation [29]. This equation is

$$L = \frac{K\lambda}{\beta . cos\theta}$$

Where "L" is the crystallite size, "λ" is the X-rays' wavelength, "β" is the full width half maximum (FWHM) and K is the Scherrer constant (~ 0.9). In our case, the radiation used was Cu-Kα having wavelength (λ) of 0.15418 nm.

3.2.3 Micro-hardness Testing

The term "micro-hardness" or "micro-indentation hardness" is employed to describe the hardness testing of materials with low applied loads. In this method, a diamond indenter of specific geometry is impressed into the surface of the test specimen using a known applied test load of 1 to 1000 gf. This testing can be used to observe changes in hardness on the microscopic scale. The two most commonly used micro-hardness tests are:

- Vickers hardness test (HV)
- Knoop hardness test (HK)

[1] Crystallite size is different than that of the particle size: a particle may be made up of several different crystallites. In addition, crystallite size often matches grain size, but there are exceptions.

In our experimental study, we used Vickers method. In this testing, the hardness number is calculated by measuring both the diagonals of the indent and then the average value is used to compute the Vickers number (see Figure 12). Mathematically;

$$HV = \frac{0.1891F}{d^2}$$

Where, "*F*" is the applied load and "*d*" represents the diagonal length of the indent.

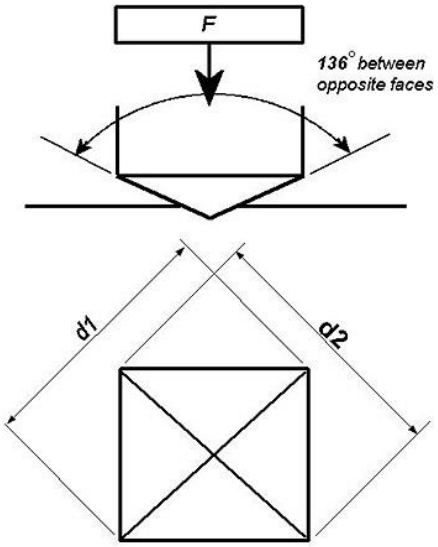

Figure 12: Schematic of micro-hardness test.

3.2.4 Scanning Electron Microscope

The Scanning Electron Microscope (SEM) uses a focused beam of high-energy electrons to generate a variety of signals at the surface of solid specimens. Accelerated electrons in an SEM carry significant amounts of kinetic energy, and this energy is dissipated as a variety of signals produced by electron-sample interactions (see Figure 13) when the incident electrons are decelerated in the solid sample. Among others, our concerned signals are Secondary Electrons (SE). Secondary electrons are most valuable for showing morphology and topography on samples. As far as the emission of secondary electrons is

concerned, during the scanning of the sample by the electron beam, high-energy electrons from the incident beam interact with valence electrons of the sample atoms. The valence electrons are released from the atom and emerge from the surface, often after traveling through the sample.

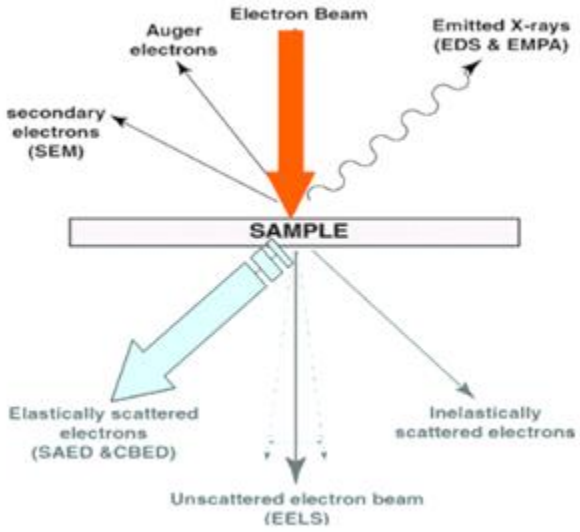

Figure 13: Electron-sample interactions.

3.3 RAW MATERIALS

Pure Aluminum powder purchased from Alpoco Ltd. and pure Alumina from Suzhou Fuer Import & Export Trade Co., Ltd were used in the experimental study. These materials were characterized using DLS, SEM and XRD. The results of these procedures are explained in the following paragraphs.

3.3.1 Aluminum powder

The aluminum powder is characterized by equiaxed particles with a narrow size-range as shown by the normal distribution of particle size in Figure 14. The average particle size of the pure aluminum powder is about 42 microns. A representative powder microstructure is shown in Figure 15. Agglomeration is not generally observed in the

powder, as the neighboring metal particles are characterized by similar charges. The powder is observed to be free of contamination as shown by the clean particle surfaces in the microstructure. Particles are observed to be in the micrometer size range, which is an indication of the necessity of a relatively higher sintering temperature and/or longer sintering time for achieving near-theoretical density, since nanometer-sized particles are characterized by faster sintering kinetics as compared to micrometer-sized ones.

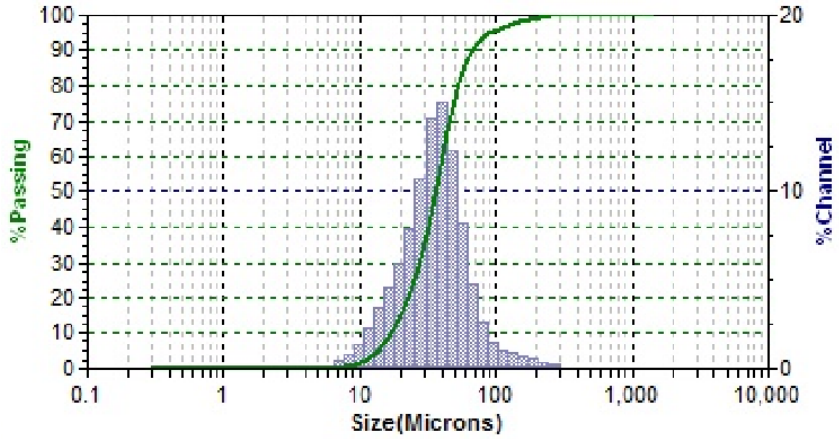

Figure 14: Particle size distribution of as-received aluminum powder.

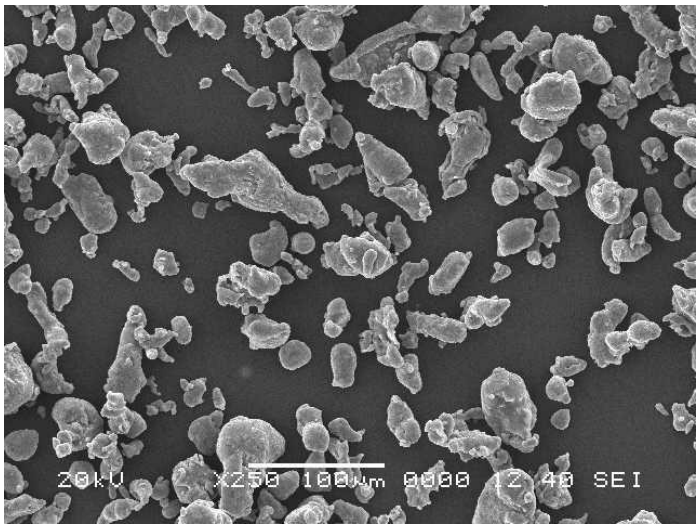

Figure 15: Microstructure of as-received aluminum powder.

The XRD spectrum of as received pure aluminum powder is shown in Figure 16. This graph shows that the powder is highly crystalline in nature. Moreover, from XRD data, the average crystallite size (calculated from the Scherrer's equation explained in section 3.2.2) of aluminum powder was found 52nm. On comparison of this crystallite size with the results from DLS, it is found that the XRD analysis revealed significantly smaller size. It is perhaps because of the agglomeration found in the powder (a particle may contain many crystallites – DLS gives particle size while XRD gives crystallite size).

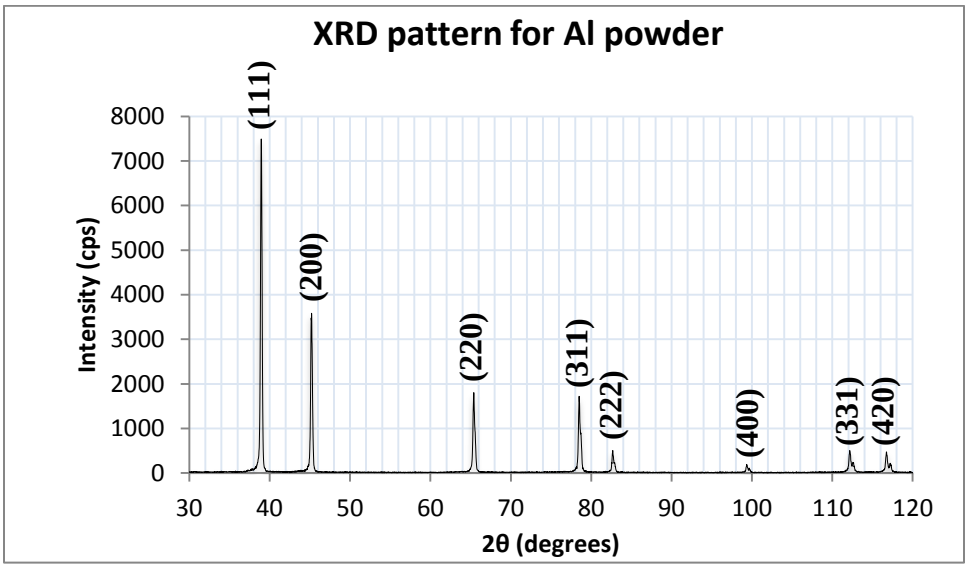

Figure 16: XRD spectrum of as received Aluminum powder

3.3.2 Alumina powder

Alumina powder is characterized by dendrite-shaped (irregular) particles which is an indication of different growth rates of particles in different directions during powder production. The powder is characterized by a wide range of particle-size as also validated by the particle size distribution shown in Figure 17. The average particle size of the pure alumina powder was about twelve microns. A high degree of particle agglomeration is observed in the powder, which is probably because of the existence of weak Columbic

forces between the Al^{+3} and O^{-2} species in the neighboring particles. The irregularity present in particle shape is also expected to result in the observed high degree of particle agglomeration, since equiaxed particles are generally known to resist particle aggregation. The microstructure of alumina powder is shown in Figure 18. The powder is observed to be free of contamination as shown by the clean particle surfaces in the microstructure. Moreover, particles are observed to be in the micrometer size range, which means that they will require higher sintering temperature or longer sintering time for achieving near-theoretical density, as observed earlier in case of aluminum powder.

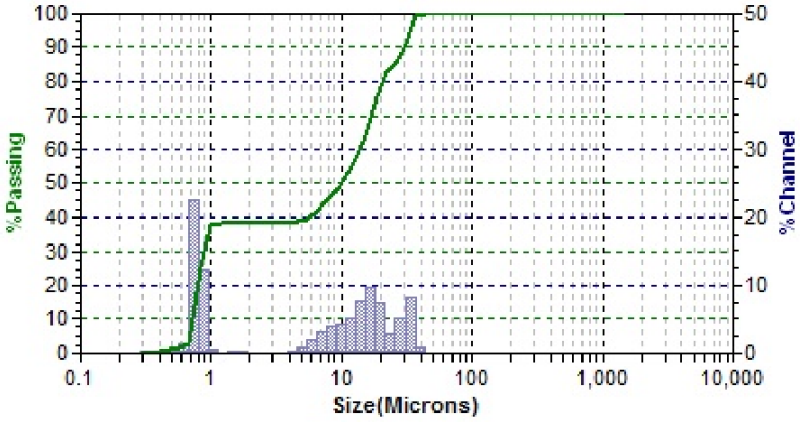

Figure 17 : Particle size distribution of as-received alumina powder.

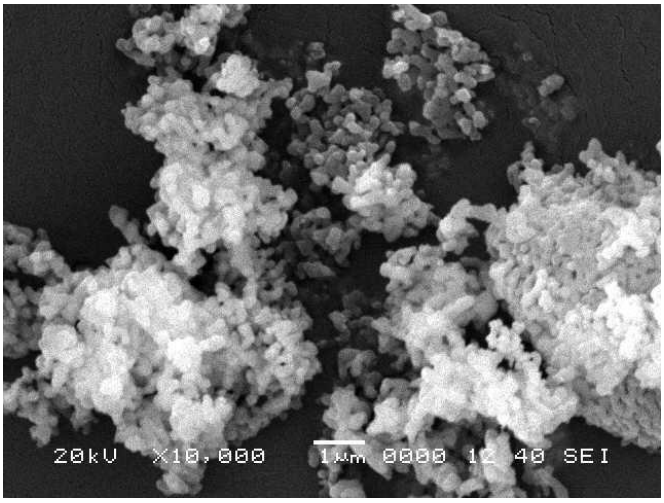

Figure 18: Microstructure of as-received alumina powder.

The XRD spectrum of as received pure alumina is shown in Figure 19. This graph shows that the material is highly crystalline. Moreover, from XRD data, the average crystallite size (calculated from the Scherrer's equation explained in section 3.2.2) was found to be 47nm. On comparison of this crystallite size with the results from DLS, it is found that the XRD analysis revealed significantly smaller size of the powder particles. The reason is same as that of the explained one for aluminum in section 3.3.1.

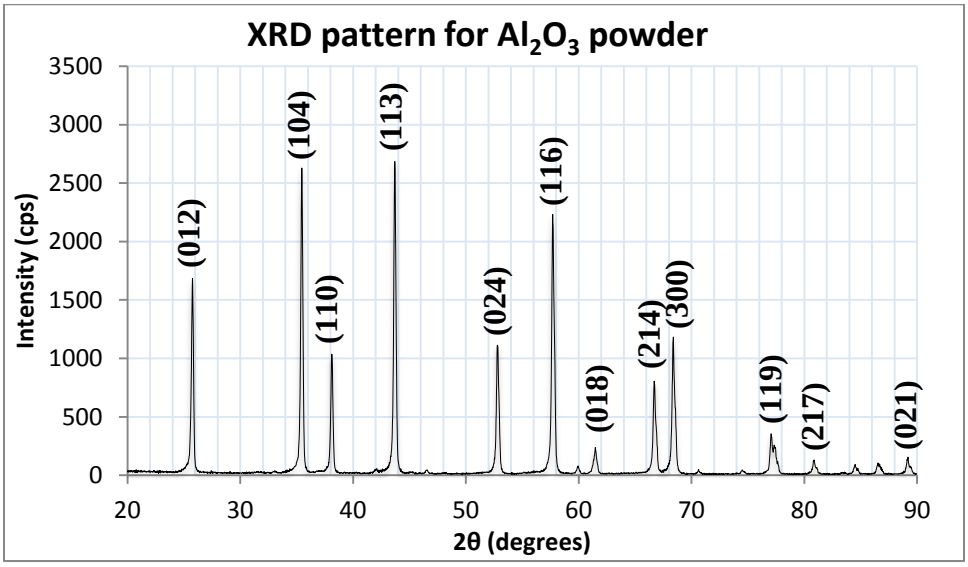

Figure 19: XRD spectrum of as received Alumina powder.

3.4 SPARK PLASMA SINTERING (SPS)

Pure aluminum and alumina powders (as received) were sintered using spark plasma sintering machine, type HP D 5/2, model SE-607 from FCT group, Systeme GmbH. The machine has the capability to sinter at very high temperatures (max. 2500 ^{o}C) and with very high heating rates (max. 400 ^{o}C/min). The powders were sintered to investigate the hardness and microstructure at various positions within the sintered samples. In our study, we used graphite die and punches having diameter of 30mm. We also used a sheet of graphite on the inner side of the die and also above and below the sample to avoid any sticking between the die-punches system and the sample. To avoid any leakage of powder

from the clearance between the punches and the die, they were assembled with almost tight fit condition. This condition is also necessary for the smooth flow of current through the die. Our target thickness of the sintered sample was 5mm.

The machine was operated at 5mm/min of force application rate. In case of aluminum, 4:1 pulse pattern with two 10ms pulse ON time followed by one 5ms pulse OFF time was used while for alumina 1:1 pulse pattern with one 1ms pulse ON time followed by one 1ms pulse OFF time was used. In addition, in both the cases ultra-high vacuum was used. For temperature measurement, K-type thermocouple – inserted in the hole located in the die – is used along with the pyrometer (especially in the case of alumina).

In our study, three samples for each material were sintered for the repetition of the mentioned experiments. In case of aluminum, the sintering temperature was 500 ^{o}C and a pressure of 20MPa (14kN force applied on 30mm die). Moreover, in case of alumina, the sintering temperature was 1500 ^{o}C and the applied pressure was 23 MPa (16kN force applied on 30mm die).

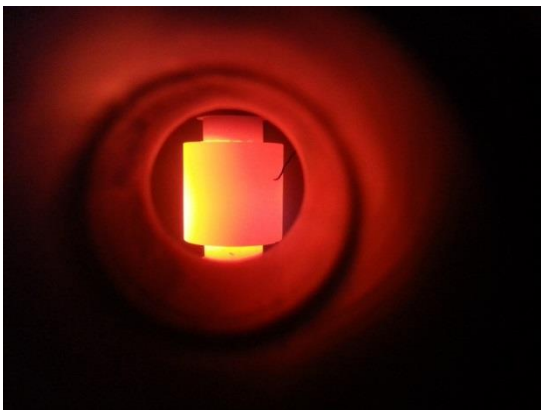

Figure 20: Die-punch system during sintering of alumina samples

3.5 RESULTS

The results which we have got in our experimental study are explained in the following paragraphs.

3.5.1 Sample Preparation

After SPS, the sintered samples were cut into two halves with the help of diamond wheel cutter. Each of them was then mounted in the thermoset plastic for further analysis. After mounting, the aluminum samples were grinded and polished using different grade sand papers and alumina suspension. In case of alumina, the sample was grinded with 74 and 20 micron diamond wheel followed by polishing with diamond suspension of 6 and 1 microns. The sample was final polished with alumina suspension. After polishing, the samples were etched to reveal the microstructure clearly. At the end, the samples were coated with a thin layer of gold to give better resolution for electron microscopy.

3.5.2 Hardness Test

In this study, micro-hardness testing of the sintered samples was done using Vicker's MMT-3 digital micro-hardness tester, Buehler, USA. In each sample, the readings were recorded at forty five positions (see Figure 21) using diamond indenter with 300gf load in case of aluminum and 2000gf in case of alumina, applied for 12sec.

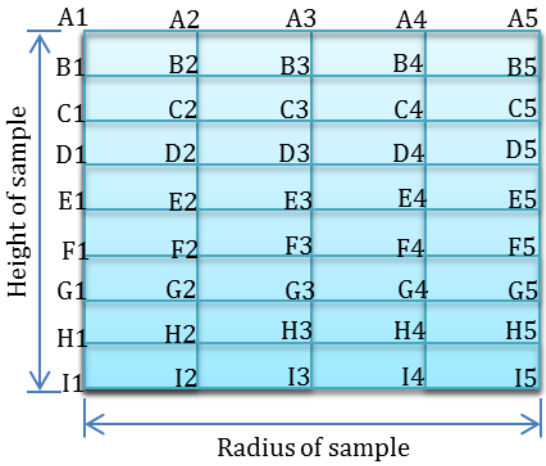

Figure 21: Positions of the hardness test

From results, in the case of aluminum, it is observed that radially hardness is almost uniform but at the edge, the hardness shows decreasing trend (see Figure 22). In addition, this decrease is more in the axially distal planes as compared to the planes near to the center. In axial direction (from Figure 23), the hardness is symmetric about the central "*rθ*" plane and is overall decreasing along either direction. There is an exception in the plane at the edge of the sample, where it shows increasing trend along either side of the central "*rθ*" plane. Furthermore, the average hardness of the sintered sample is around 24 on Vicker's hardness scale. It is reported by M. O. Bodunrin et. al., [30] that the hardness of the aluminum is around 40 VH which is higher than that in our case. This is because of the fact that the sintered sample is not fully dense.

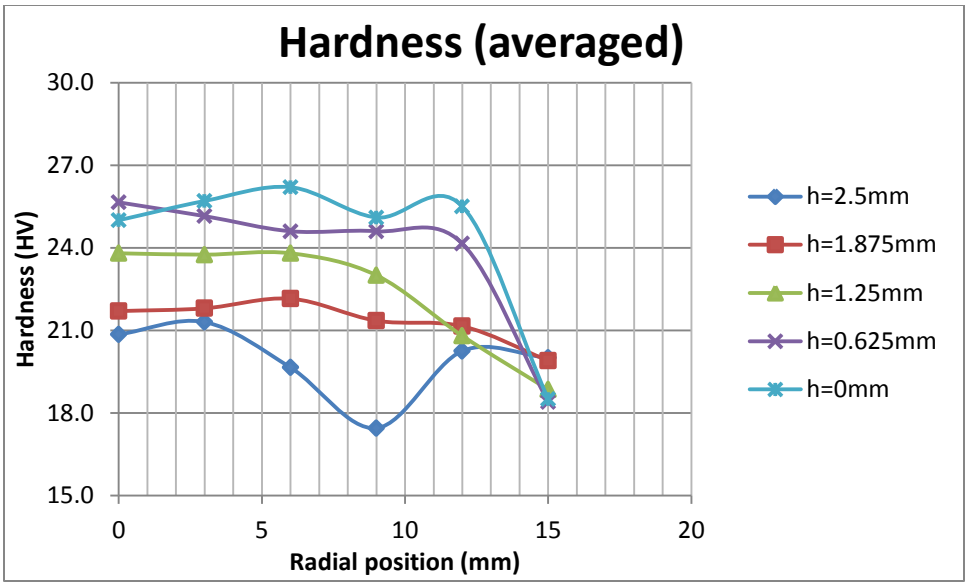

Figure 22: Hardness (HV) along the radius at different heights in aluminum sample

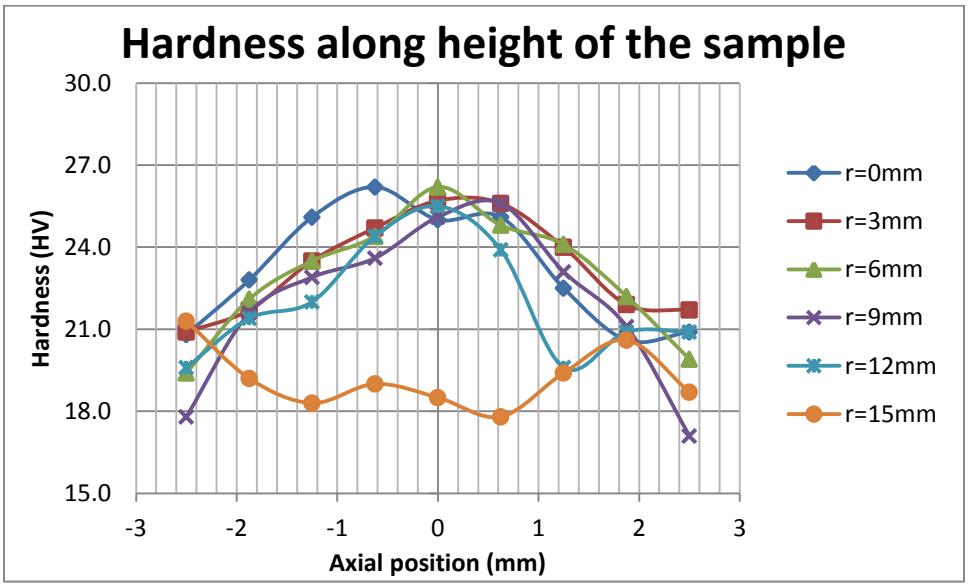

Figure 23: Hardness (HV) along the height at different radial positions in aluminum sample

In case of alumina, in radial (see Figure 24) as well as axial (see Figure 25) direction, the hardness gives some non-uniform fluctuating trend in all the planes. But overall the hardness is increasing along the radial direction.

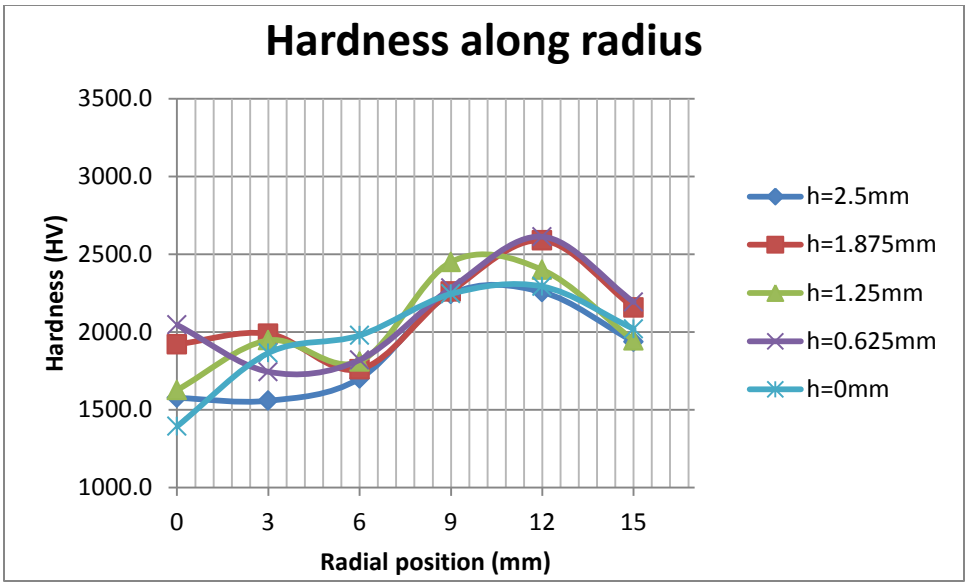

Figure 24: Hardness (HV) along the radius at different heights in alumina sample

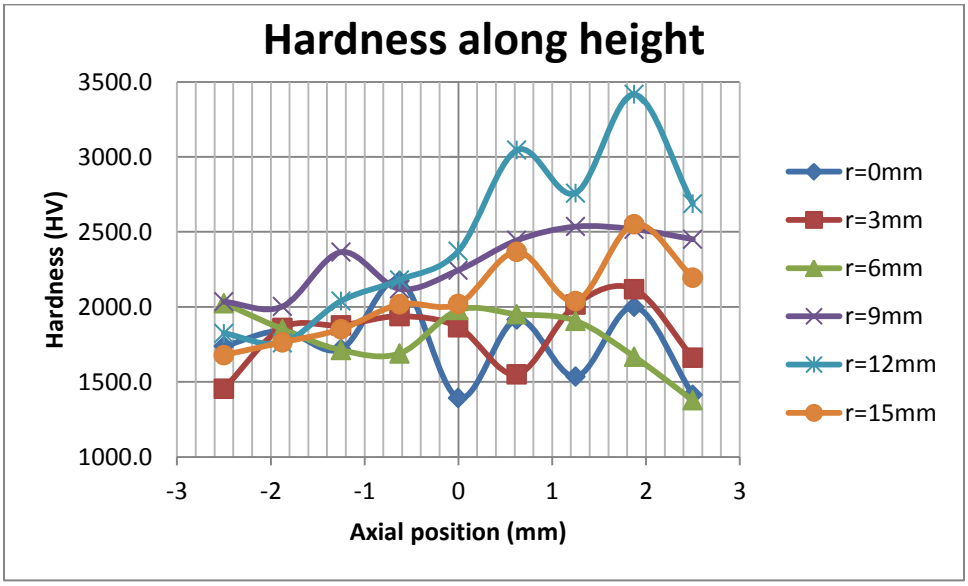

Figure 25: Hardness (HV) along the height at different radial positions in alumina sample

3.5.3 Microstructure

The SEM gives a detailed high resolution qualitative analysis and helps in better understanding of the microstructure. JEOL JSM 6400 SEM was used to examine the morphology of the sintered samples at different locations within the sample. This analysis

was carried out at high voltage in high vacuum state. SEM images were recorded at different magnifications and positions within the polished surface (see Figure 26 & Figure 27). In SEM analysis, it revealed that the microstructure is uniform in general and porosity is observed at all the positions in the sample with little variation in the quantity.

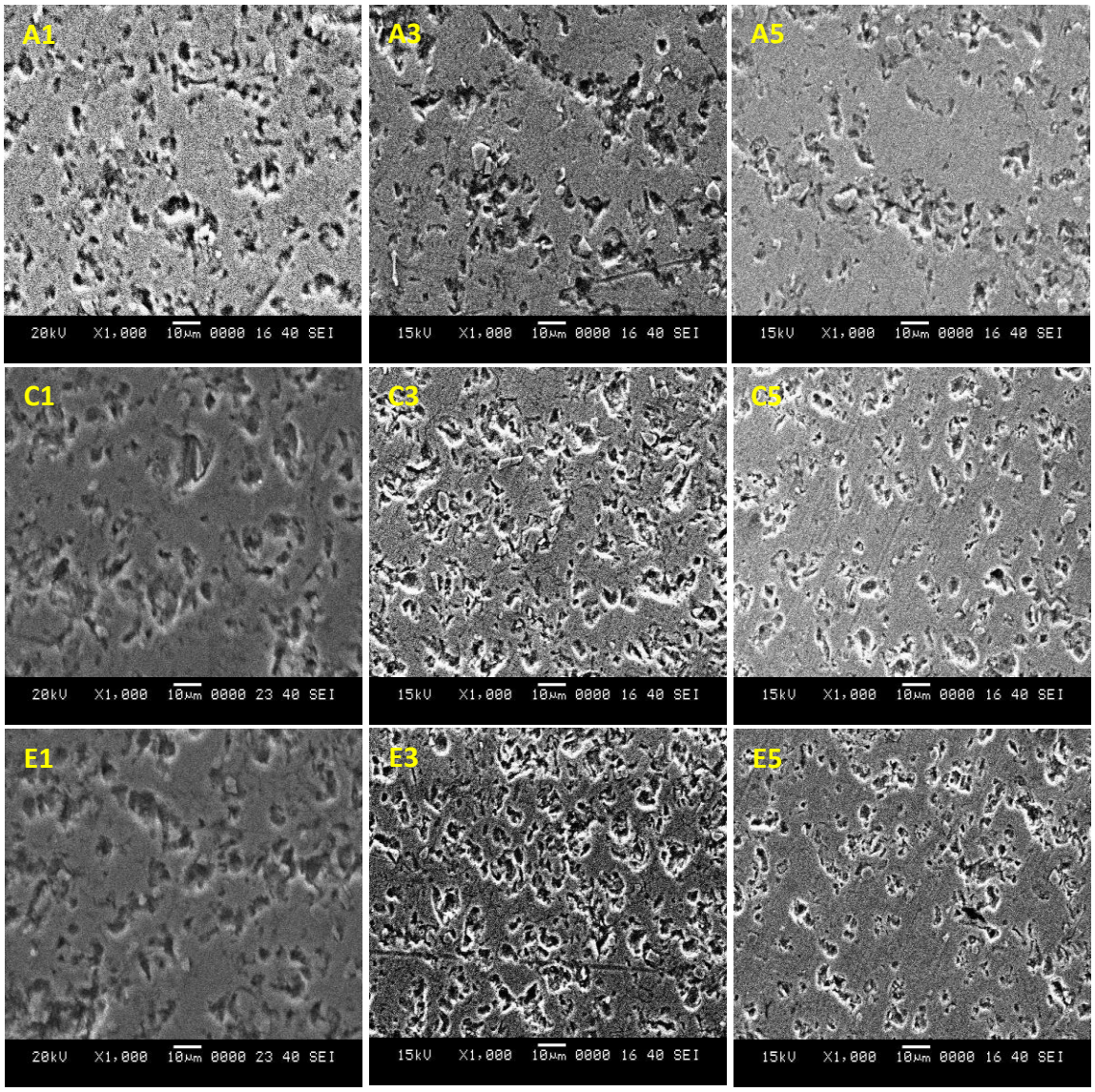

Figure 26: SEM micrographs of the aluminum sample at 1000x magnification at different locations: A1, A3, A5, C1, C3, C5, E1, E3, & E5

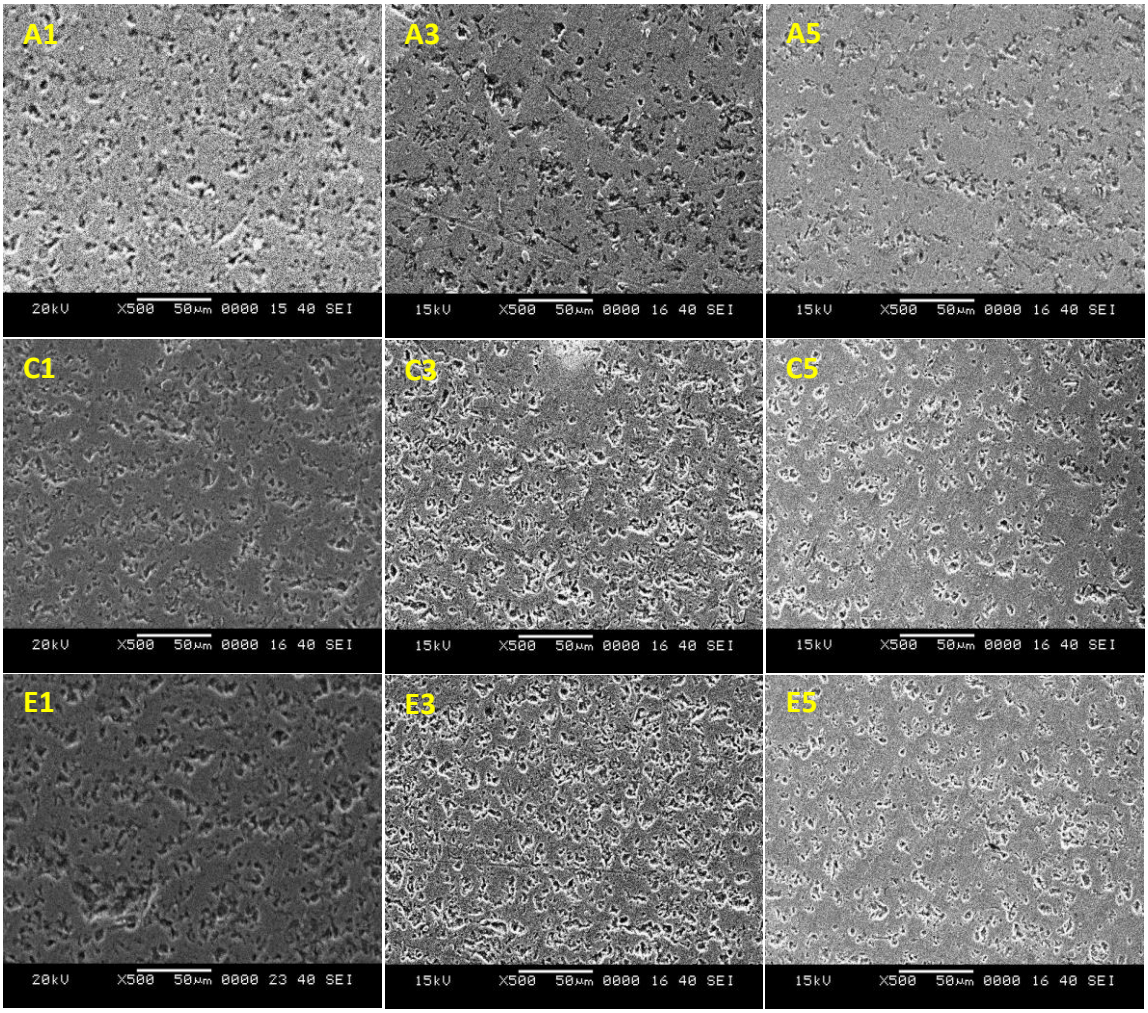

Figure 27: SEM micrographs of the aluminum sample at 500x magnification at different locations: A1, A3, A5, C1, C3, C5, E1, E3, & E5

CHAPTER 4

ELECTRICAL-THERMAL MODEL

For the modeling of SPS process, we need to solve two physical models: an electrical-thermal (Joule heating) model, & a structural (solid mechanics) model. In this chapter, our focus will be the electrical-thermal modeling of the SPS.

4.1 INTRODUCTION

The purpose of the electrical-thermal model is to calculate the temperature evolution in the die-punch- sample system. The basic phenomenon behind this is the Joule's heating – being the only source of heat generation in the system – in which the electrical current generates heat when it passes through any material having some electrical resistance. So, the heat generated, and hence the temperature, in the system is a very strong function of the applied electrical parameters. Therefore, the accuracy of the electrical-thermal model is very significant in accurate thermal behavior prediction of the system.

As far as the electrical-thermal modeling of the Spark Plasma Sintering process is concerned, several different attempts have been made. Scientists and investigators used different approaches to model the electrical-thermal behavior of the system but the overall background of the principles of physics used is almost the same i.e. the Joule heating effect. Some of them used only mathematical and analytical methods for solution while others used different platforms/languages like FORTRAN, MATLAB, ANSYS, ABAQUS and COMSOL Multiphysics. In our model, we used COMSOL Multiphysics to simulate the SPS process. In the following paragraphs the developed model will be explained in adequate detail.

4.2 THE MODEL

4.2.1 Mathematical Model

In the SPS process, there is a strong coupling between electrical and the thermal field because of the Joule's heating phenomena. In the following lines, the mathematical equations which govern this process are discussed according to its use in the COMSOL Multiphysics package.

Joule heating model

The *Joule Heating Model* node uses the heat equation for conduction – basically conservation of energy – in solids and an interacting electric current. It uses the following version of the heat equation as the mathematical model for heat transfer in solids:

$$\rho C_P \frac{\partial T}{\partial t} + \rho C_P u.\nabla T = \nabla.(k_t \nabla \mathrm{T}) + Q \tag{1}$$

In this case, the volumetric heat source "*Q"* comes from the electric current and is added in the *Electromagnetic Heat Source* node.

For an electrically conductive medium, the electric charge conservation can be expressed by

$$\nabla.J = Q_j \tag{2}$$

The electrical field may also be expressed as a gradient of the electrical potential "*V*" as

$$\mathrm{E} = -\nabla \mathrm{V} \tag{3}$$

The other equations used in the Joule heating are:

$$J = \sigma E + \frac{\partial D}{\partial t} + J_e \tag{4}$$

$$J = (\sigma + \varepsilon_o \varepsilon_r \frac{\partial}{\partial t}) E + J_e \tag{5}$$

Electric Field

The default electrical conductivity "σ" (SI unit: S/m) is taken from the material properties. The Constitutive relation that describes the macroscopic properties of the medium (relating the electric displacement "*D*" with the electric field "*E*") and the applicable material properties, such as the relative permittivity[2] (the value of the relative permittivity is defined in the material properties) is given by:

$$D = \varepsilon_0 \varepsilon_r E \tag{6}$$

Heat Conduction

The value of the thermal conductivity "*k"* (SI unit: W/(m·K)) is described in material properties. The thermal conductivity describes the relationship between the heat flux vector "*q"* and the temperature gradient "∇T". This relationship is known as Fourier's law of heat conduction and is given as:

$$q = -k \nabla T \tag{7}$$

Thermodynamics

The values of "C_p" (SI unit: J/(kg·K)) and the ρ (SI unit: kg/m^3) are defined in Table 2.

[2] it is the ratio of the amount of electrical energy stored in a material by an applied voltage, relative to that stored in a vacuum – it's a unitless quantity

Electromagnetic Heat source

The *Electromagnetic Heat Source* is a default node in the Joule Heating multiphysics interface. It adds the resistive heating (or ohmic heating) caused by the electric current according to Joule's first law. This node represents the source term "Q" (W/m^3) in the heat equation implemented by the *Joule Heating Model node*; see equation (1). The Joule's first law is stated as:

$$Q = J.E \tag{8}$$

Boundary Electromagnetic Heat Source

The *Boundary Electromagnetic Heat Source* feature maps the electromagnetic surface losses as a heat source on the boundary (SI unit: W/m^2) in the heat transfer part of the model. The mathematical equation governing this phenomenon is:

$$-n.(-k\nabla T) = Q_{sh} \tag{9}$$

Electric insulation

The *Electric Insulation* node adds electric insulation as a boundary condition, which means that no electric current flows into the boundary. At interior boundaries, it means that no current can flow through the boundary and that the electric potential is discontinuous across the boundary. The mathematical equation for this phenomenon is:

$$-n.J = 0 \tag{10}$$

Thermal Insulation

The Thermal Insulation node is the default boundary condition for all heat transfer interfaces. It models a well-insulated boundary with no heat flux across the boundary, mathematically;

$$n.(k\nabla T) = 0 \tag{11}$$

This condition specifies where the domain is well insulated. Intuitively this equation says that the temperature gradient across the boundary must be zero. For this to be true, the temperature on one side of the boundary must equal the temperature on the other side. Because there is no temperature difference across the boundary, heat cannot transfer across it.

Electric Potential

The *Electric Potential* node provides an electric potential "*V"* as the boundary condition. Since the electric potential is being solved for in the interface, the value of the potential is typically defined at some part of the geometry – in our model at the top surface of the punch.

$$V = V_0 \tag{12}$$

Ground 1

The *Ground node* is a boundary condition that implements ground as the boundary condition. Ground means that there is a zero potential on the boundary. In our model, it is applied at the bottom surface of the lower punch. Mathematically;

$$V = 0 \tag{13}$$

Continuity

The *Continuity* node provides continuity in the field variables across a boundary between parts in an assembly where a pair has been created. The *continuity* condition is only suitable for pairs where the boundaries match. In our model, it has been applied at all the contacts in the model.

Convective cooling

The *Convective Cooling* node adds the following heat flux contribution to its boundaries:

$$h.(T_{ext} - T)$$

4.2.2 Model in COMSOL Multiphysics

Geometry:

The schematic of the SPS process is presented in Figure 28. This system comprises of two punches, one die and a sample. The dimensions of the system are shown in Table 2.

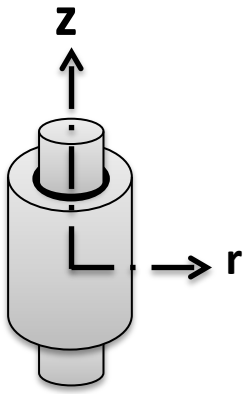

Figure 28: Schematic of the die-punch-specimen system in SPS process.

Table 2: Dimensions of the used geometry

	Diameter (mm)	Height (mm)
Die	30	130
Punches	30	70
Sample	30	Variable (10-100)

The SPS model developed in COMSOL's environment is axisymmetric (because all the components are cylindrical) as shown in Figure 29. The total number of domains in the developed model is four: "*r1*" is the die, "*r2*" & "*r3*" are punches, and "*r4*" is the sample.

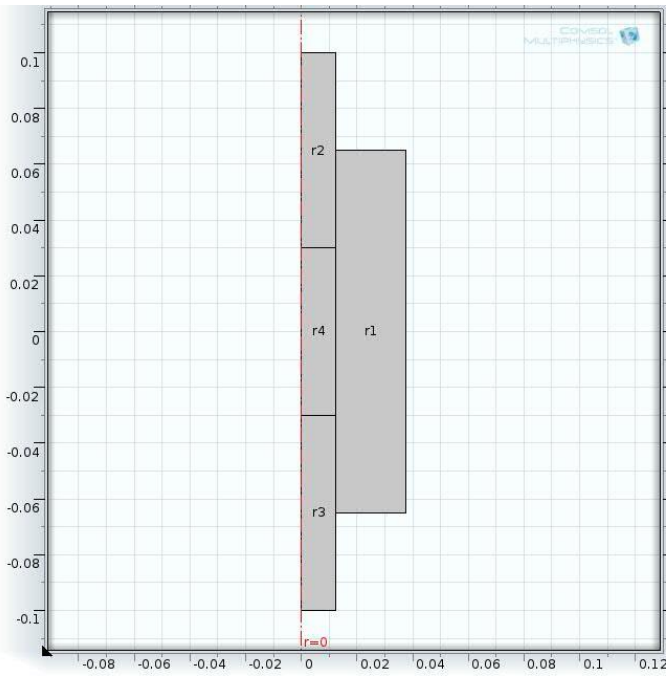

Figure 29: Model Geometry in COMSOL Multiphysics environment.

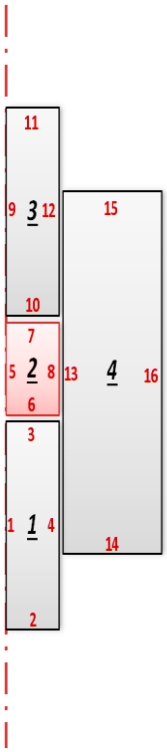

Figure 30: Domains and boundaries in the model.

Applied Conditions

The boundary conditions that are applied in the developed model are:

Voltage: DC voltage which is a function of time (see Figure 31) having its maximum value of 1.2 Volts is applied at boundary # 11 – the top boundary of the upper punch – (see Figure 30).

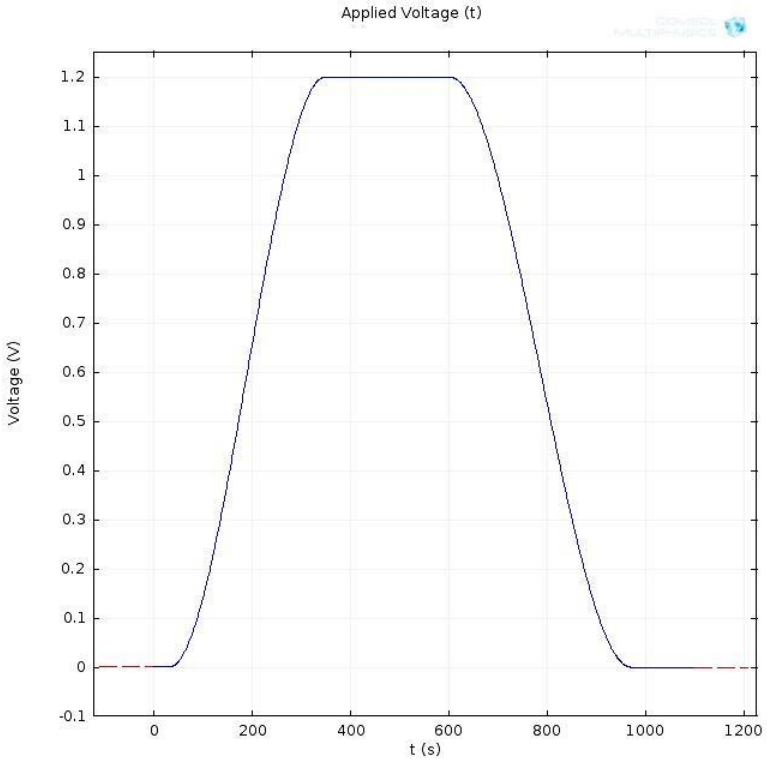

Figure 31: The Applied voltage

Ground: The ground i.e. V=0 is applied at boundary # 2 – bottom of the lower punch – see Figure 30.

Convective cooling: Convective cooling condition with heat transfer coefficient of 20 $Wm^{-2}K^{-1}$ is applied at boundaries # 14, 15 & 16 i.e. outer surfaces of the die.

Electric Insulation: This condition is applied at all the external boundaries (14, 15, & 16) as there is no electric current leakage there.

The Mesh

The mesh that we used in our analysis varied in different simulations depending upon the convergence: we used mapped and free triangular mesh (see Figure 32). The number of

elements varied with the variation in the thickness of the sample. For the simulation without any sample, the details of the used mesh are as given below:

Number of vertex elements: 16

Number of boundary elements: 5462

Number of elements: 16370

Number of degrees of freedom solved for: 76412.

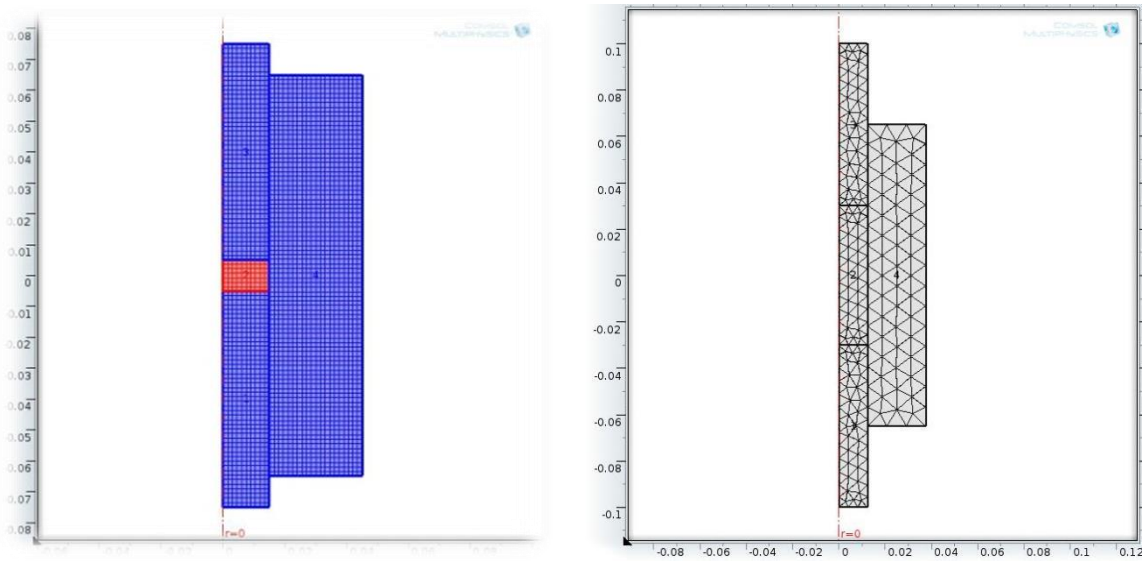

Figure 32: Meshes used in the model: Left) mapped, & Right) triangular.

Materials

The punches and the die are usually made up of graphite. The sample can be of different materials – in our case it is Aluminum in (case-I) and Alumina (case-II). The thermo-physical properties of these materials are shown in Table 2.

Table 3: Thermo-physical properties of the materials used in the study

Properties	**Graphite**	**Aluminum**	**Alumina**
Thermal conductivity ($W.m^{-1}.K^{-1}$)	98.83917 - 0.03660498 T + 5.535419E-6 T^2	39.646 + 1.684 T - 0.0054134T^2 + 8.4313E-6T^3 - 6.537E-9T^4 + 2.002E-12T^5	5.5 + 34.5exp{-0.0033(T - 273.15)}
Electrical conductivity ($S.m^{-1}$)	1/(6.6049E-14 T^2 + 1.329580E-9 T + 5.219500E-6)	1/(6.619834E-17T^3 - 8.192563E-14T^2 + 1.451201E-10T - 1.037048E-08)	0.25E-8
Density ($kg.m^{-3}$)	1768	2736.893-0.006011681T - 7.012444E-4T^2 + 1.3582E-6T^3 - 1.367828E-9T^4 + 5.177991E-13T^5	3900
Relative permittivity	(0.75328 + 8.27761E-6 T)	1.7	10
Heat capacity at constant pressure ($J.kg^{-1}.K^{-1}$)	(310.5 + 1.7 T)	595.6585 + 1.513029T - 0.002070065T^2 + 1.303608E-6T^3	1044.6 + 0.1742T – 2.796E7T^2
Young's modulus (Pa)	200E9	7.659324E10 + 2007396.0T - 186458.4T^2 + 419.2175T^3 - 0.3495083T^4	300E9
Poisson's ratio	0.3	0.3238668 + 3.754548E-6T + 2.213647E-7T^2 - 6.565023E-10T3 + 4.21277E-13T^4 + 3.1705E-16T^5	0.22
Coefficient of thermal expansion (K^{-1})	8.0E-6	15E-6	5.494E-4 + 4.504E-7T – 8.682E-11T^2

4.3 RESULTS & DISCUSSION

In this study, COMSOL Multiphysics software is used to simulate the SPS process. The model comprised of four domains – a die, a sample and two punches. They were assembled using identity pairs at all the matching boundaries.

4.3.1 General Observations about the whole system

Current density distribution

From the results, it is observed that current is passing through all the domains of the system because of the continuity of the field. Also, it is noticed that the current density is higher in the sample as compared to the die (see Figure 33 & Figure 34). It is because of the fact that the electrical conductivity of the material is higher in the sample than that of the die thereby providing less resistant path to the current. In addition, it is also found that the current density is higher in that region of the punch, in axial direction, which is not in contact with the die (see Figure 33 & Figure 34). The reason for this is that that the current doesn't have any path to distribute in the said region and when it enters the region which is in contact with the die, it distributes in the die and results in the reduction of the current density in the punch. It is also noticed, from the comparison of Figure 33 and Figure 34, that the gradient in current density decreases with increase in the thickness/height of the sample i.e. the current density gradient has inverse relationship with the aspect ratio (l/r) of the sample.

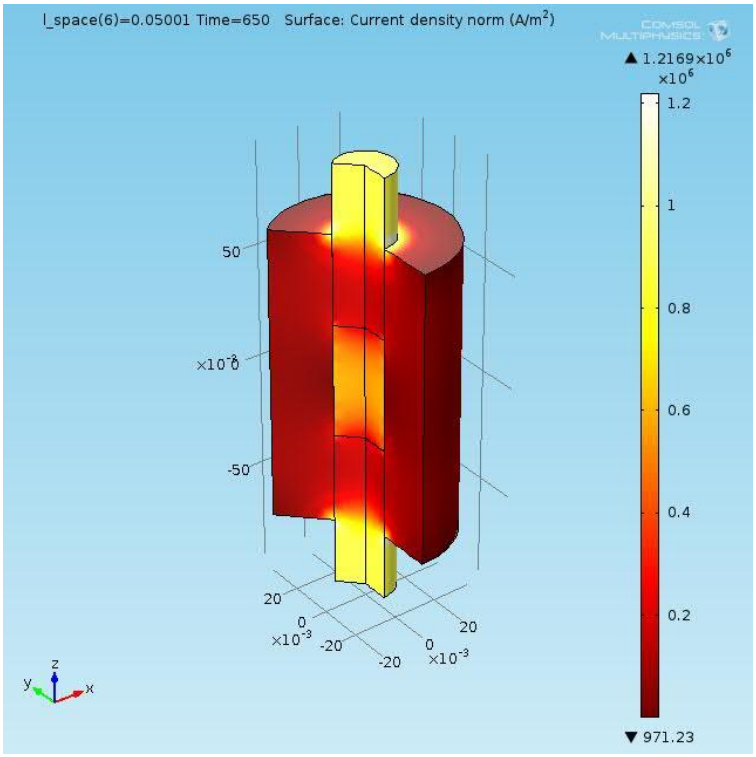

Figure 33: Surface Current density contour plot for sample height=50 mm, at 650s.

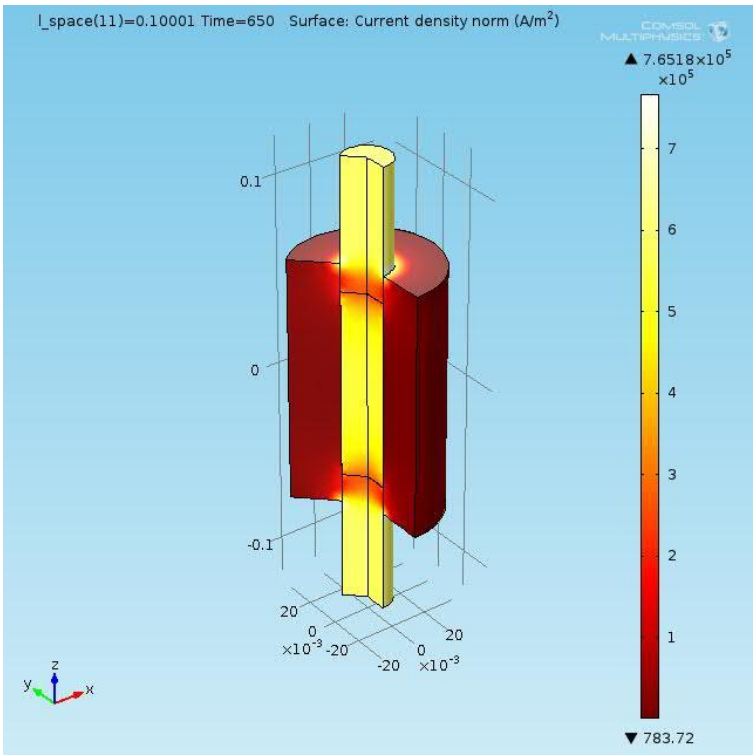

Figure 34: Surface Current density contour plot for sample height=100 mm, at 650s.

Temperature distribution

From the analysis of the temperature contours – Figure 35, & Figure 36 – we observe that the maximum temperature is achieved in those planes of the punches which are farthest from the sample. The reason for this is that the current density is highest in that region which is responsible for the Joules heat generation. Also, the maximum temperature achieved in the sample is lower in the thicker samples (see Figure 39) i.e. the maximum achieved temperature is inversely related to the aspect ratio of the sample. It is because of the fact that as the volume of the sample increases it needs more energy to reach the same temperature. In addition, from the comparison of Figure 37 & Figure 38, the temperature evolution in the punches as well as the sample follows the same profile.

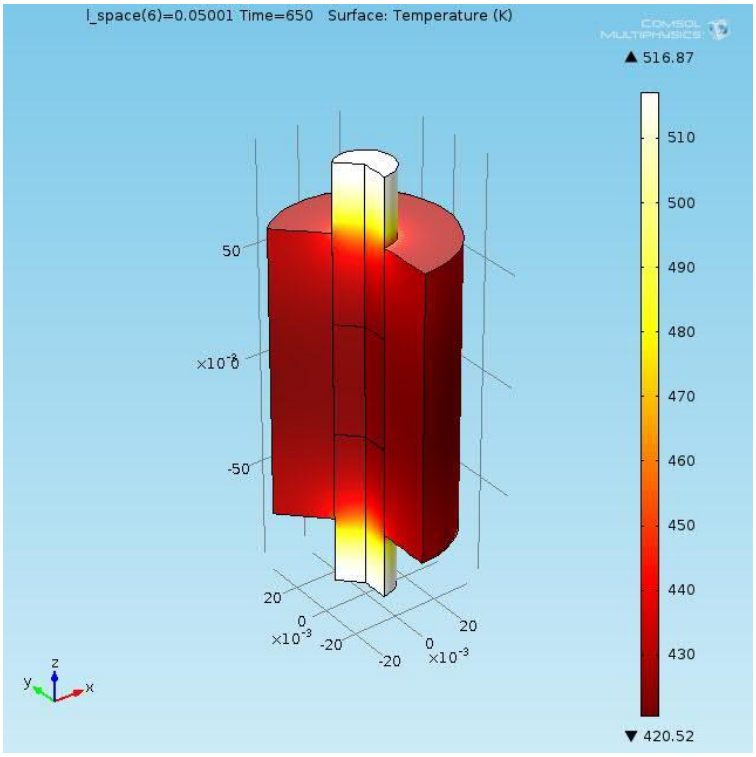

Figure 35: Surface Temperature contour plot for sample height=50mm, at t=650s

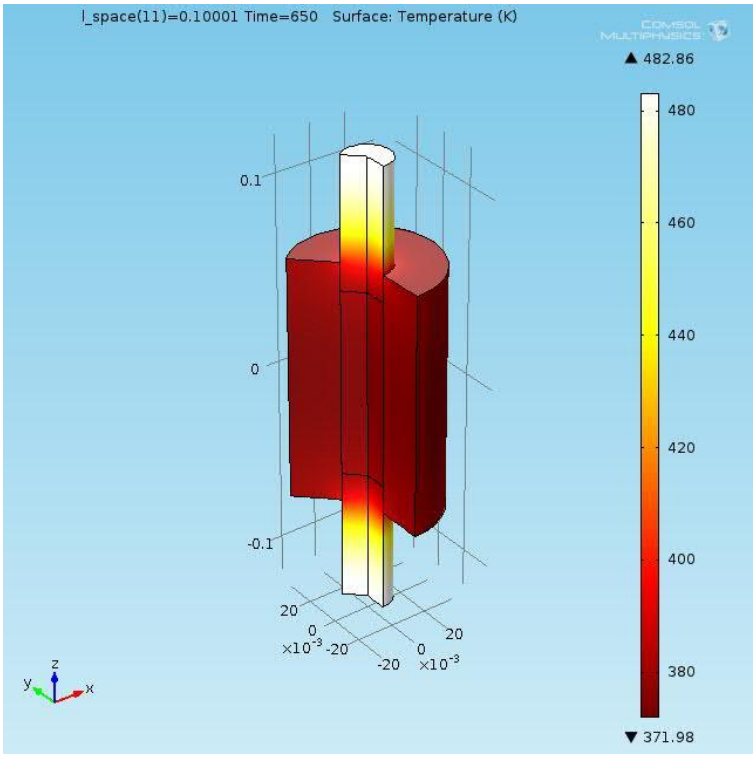

Figure 36: Surface Temperature contour plot for sample height=100mm, at t=650s

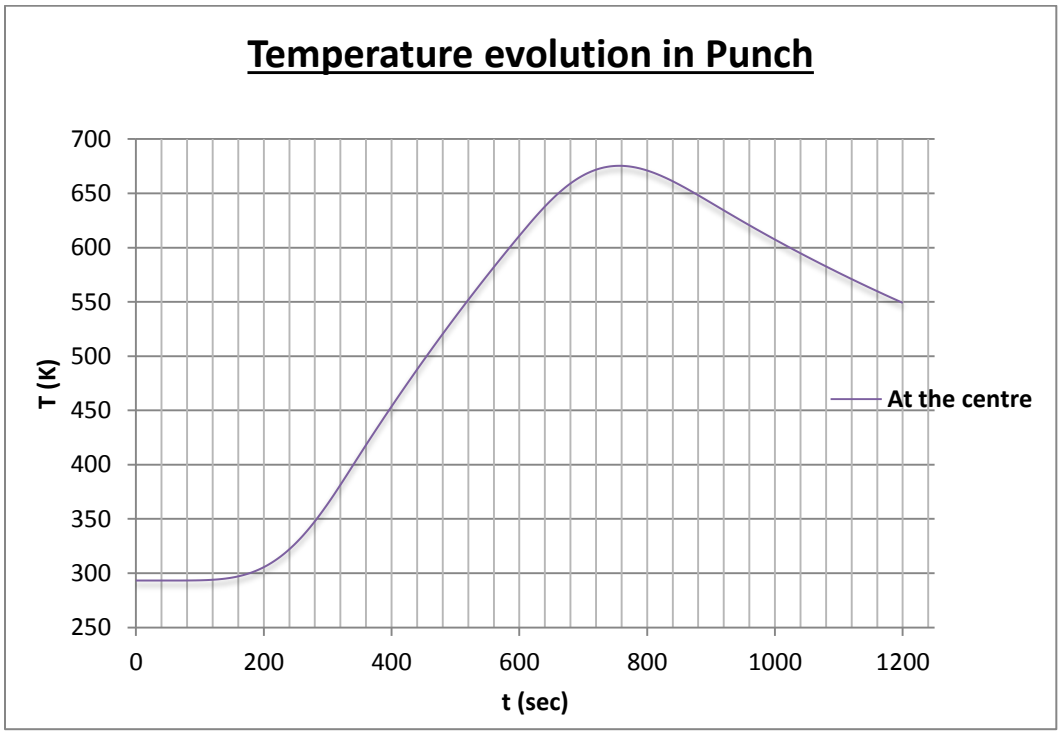

Figure 37: Graph showing the temperature evolution in punches

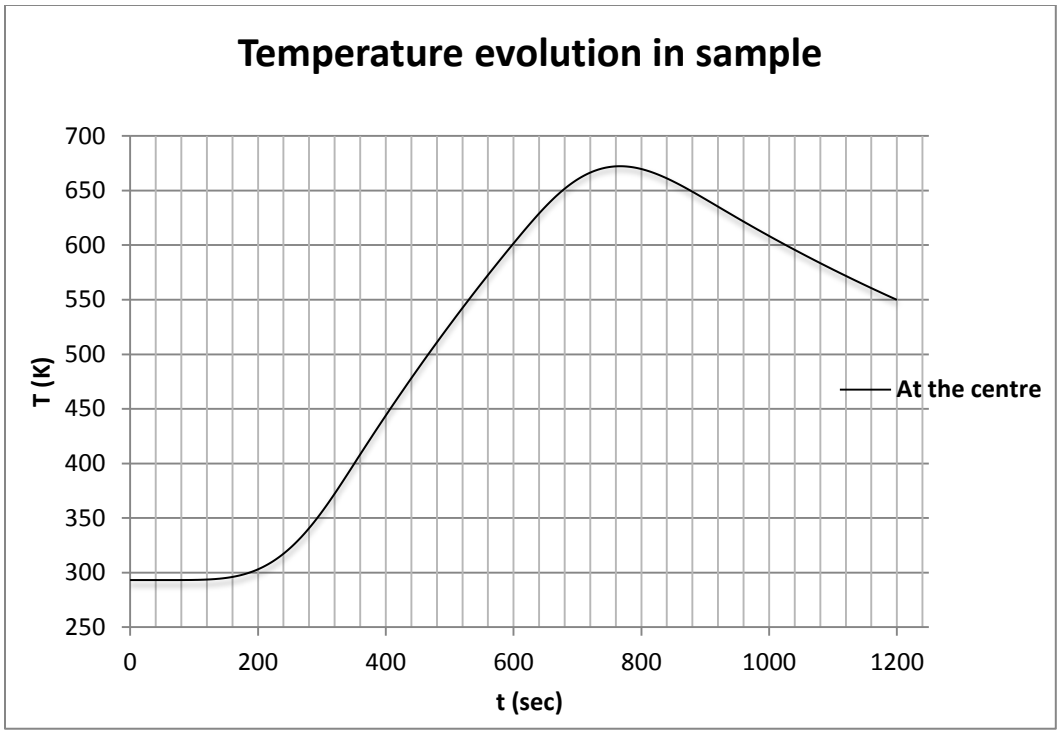

Figure 38: Graph showing the temperature evolution in the sample

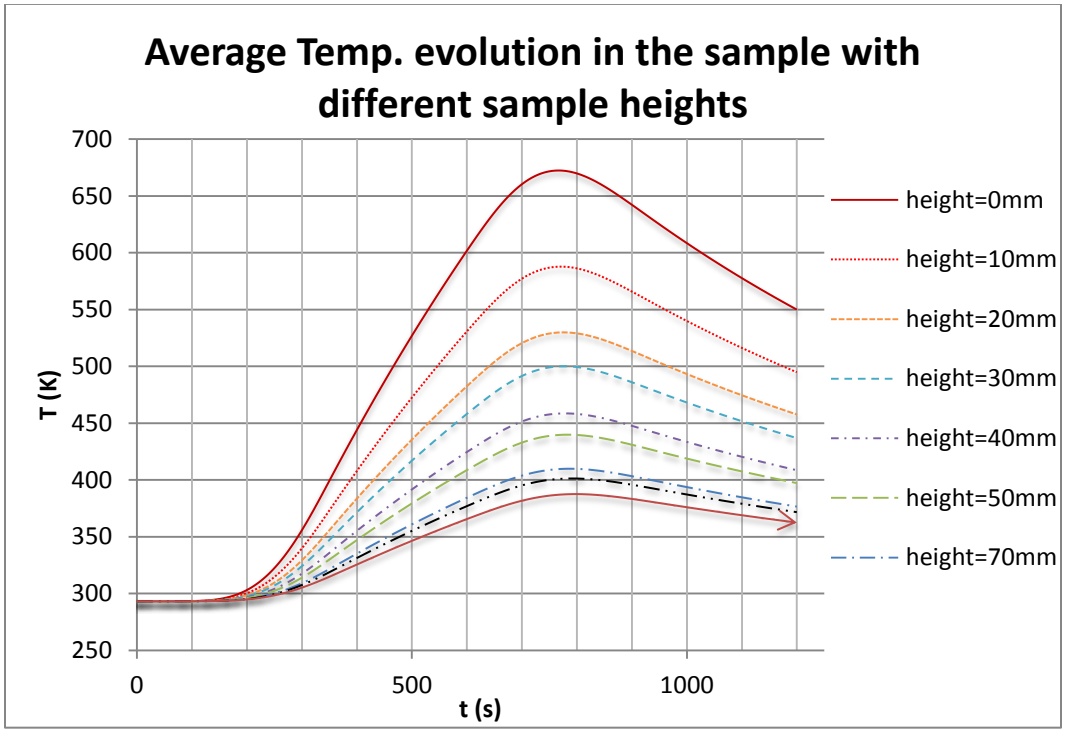

Figure 39: Graph showing average temperature evolution in sample for different sample heights.

In the following paragraphs, at first, the validation of the developed model will be discussed which will be followed by two case studies: Case-I and Case-II. Case-I deals with the electrical-thermal model for an electrically conductive material (Aluminum) and Case-II deals with the electrical-thermal model for an electrically insulator material (Alumina).

To analyze the results in a simplified manner, the sample's cross-section has been divided into several columns and rows as shown in Figure 40. The column "1" shows the axis of symmetry while column "5" is at the extreme radial position in the sample and row "*A*" represents the top surface while row "*I*" is the bottom surface of the sample. Moreover, row "*E*" is the central "$r\theta$" plane.

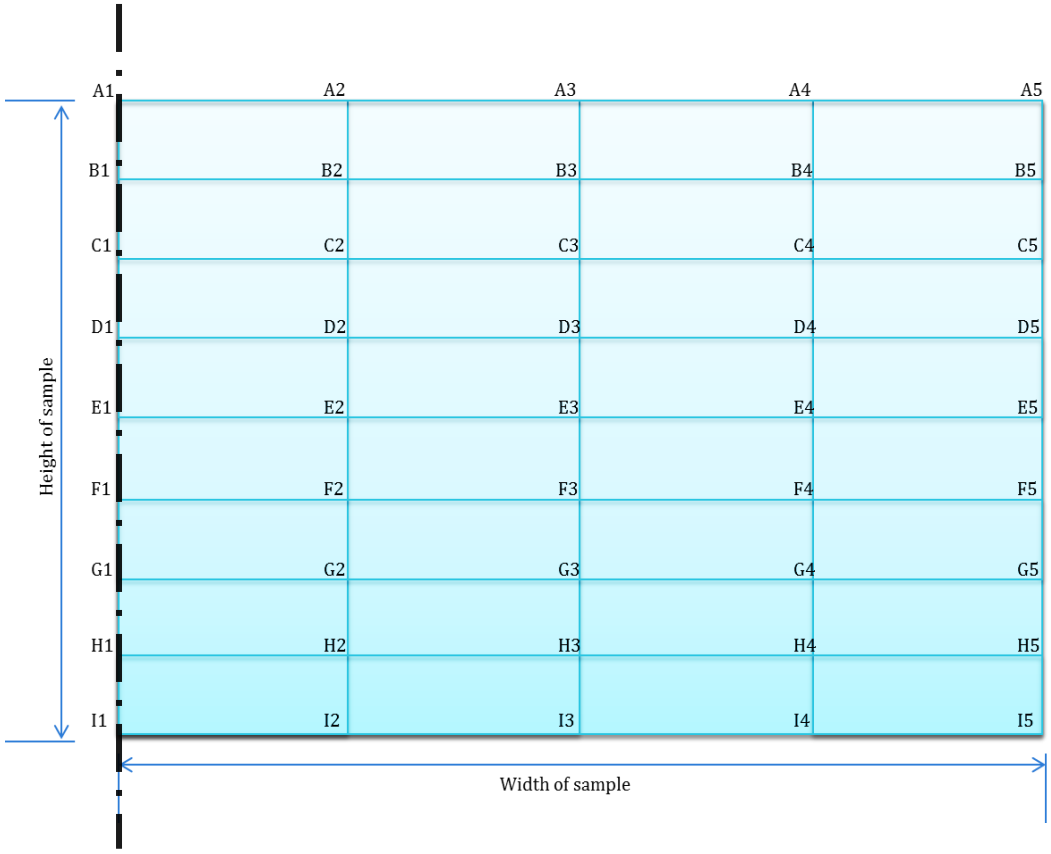

Figure 40: Divisions in the sample.

4.3.2 Validation of the developed model

In order to validate the model (only qualitatively), the results of the developed model are compared with the published literature in the following paragraphs. The developed model is for aluminum sample.

Current density distribution

From Figure 45, it is noticed that the current density is increasing along positive radial direction. Similar trend has also been reported by G. Antou et. al [31], F. Mechighel et. al [32] and G. Mole'nat et. al [33] (see Figure 41).

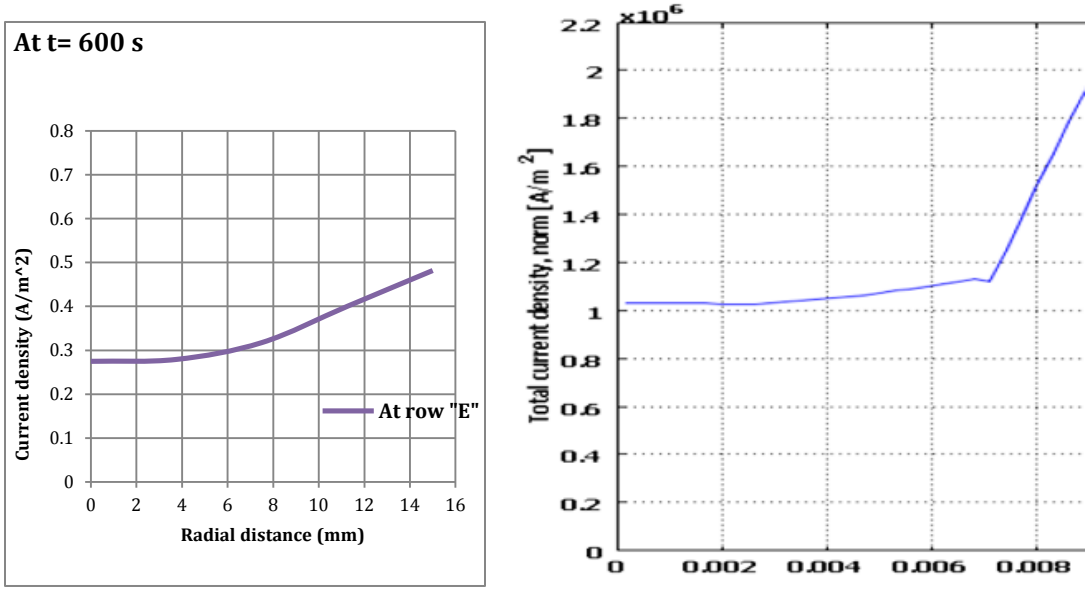

Figure 41: Current density distribution along the radius: Left) this study, & Right) F. Mechighel et. al. [32]

Temperature distribution

From Figure 49, it is noticed that generally the temperature in any plane, is found maximum at the central axis of the sample and has decreasing (although very little) trend

along the radius of the sample. Similar trend has been reported by F. Mechighel et. al in [32], S. Munoz et. al [34], and Y. Song et. al [35] (see Figure 42).

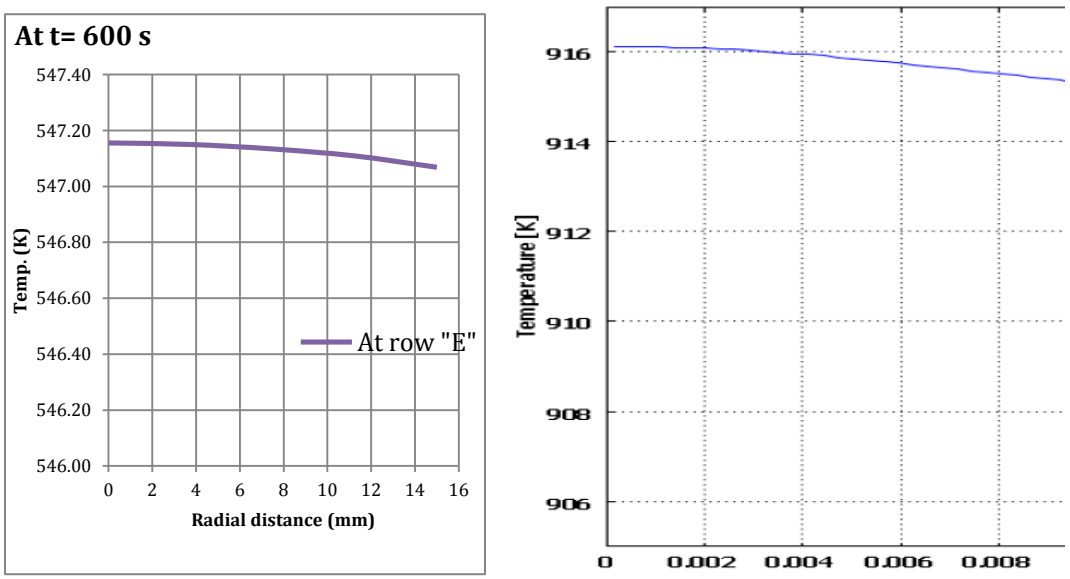

Figure 42: Temperature distribution along the radius: Left) this study, & Right) F. Mechighel et. al [32].

From Figure 50, in heating cycle, the temperature in the sample along "z" axis (positive as well as negative direction) has increasing trend and is symmetric about the central "rθ" plane. Similar trend has been shown by F. Mechighel [32] G. Antou et. al [31] and Y. Song et. al [35].

From Figure 51, the temperature evolution with respect to time in any region of the sample adopts almost the same profile: the temperature initially increases, reaches a peak value and then starts reducing due to switching-off of the applied current and the cooling process. Similar trend has been reported by E. Olevsky et. al [36], B. McWilliams et. al [37], and G. Antou et. al [31].

4.3.3 CASE-I

Sample heights: 0-100 mm with 10 mm steps

Sample diameter: 30 mm

Sample Material: Aluminum (electrically conductor)

Current density distribution

From Figure 45, it is observed that the current density shows increasing trend along positive radial direction in the sample thereby resulting in the maximum current density at the maximum radial position. Also, the difference between the values of current densities in different planes is higher near to the central axis while it is nominal at the extreme radial positions. In addition, from Figure 46, it is also noticed that the homogeneity in current density is more (values are very close in planes near the center of the sample) in the central regions (along axial direction). Moreover, the current density shows symmetrical decreasing trend in "*z*" axis along positive as well as negative direction. The current density is found zero in the sample at the end of the process which results in no heat generation source in the system (see Figure 44). Furthermore, from Figure 47, it is noticed that the current densities evolved in the sample at any position have the same pattern as that of the applied current, as expected– the only difference is in its values.

From Figure 45 & Figure 46, it is noticed that, as the sample thickness increases, the current density gradient (in radial as well as axial direction) starts to reduce i.e. the spatial inhomogeneity in the current density is lesser in the larger sized samples than that of the

small sized samples. It is because of the fact that the difference between minimum and maximum current densities in the sample is lesser and the size of the sample is increased.

From Figure 47, the maximum current density achieved in the central *"rθ"* plane is found increasing with the increase in the size of the sample up to the thickness of 50 mm and after this it is almost uniform with the increase in size of the sample. The reason is that the current which is flowing in the die starts to concentrate in the sample because of its lower electrical resistance and this convergence of current from the die into the sample is almost complete in the sample having its height of 50 mm. After this height, no more current converges into the sample and hence it flows uniformly. One important observation is that that the current density difference between row "*A*" (sample's top surface) and row "*E*" (sample's central *"rθ"* plane) is substantial while the difference between row "*C*" (plane at the center of "*A*" and "*E*") and row "*E*" is very nominal which means that the current density homogeneity is higher in the central region of the sample. In other words, most of the inhomogeneity in current density is found near the distal regions of the sample. (Because of the same reason explained in this paragraph above).

The maximum current density is found in the "*rθ*" plane passing through the origin – located at the center of the sample – while the minimum is in the distal planes (along "*z*" axis) of the sample. Although, the location of maximum current density in the sample varies with size, its value is same in all the sizes of the samples.

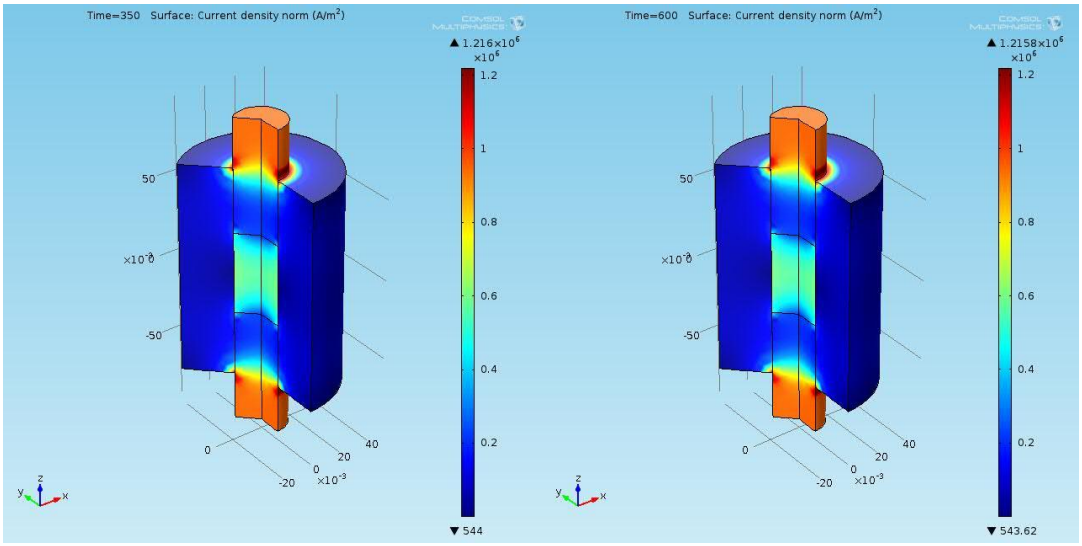

Figure 43: Current density plots at: (left) t=350s, & (right) t=600s

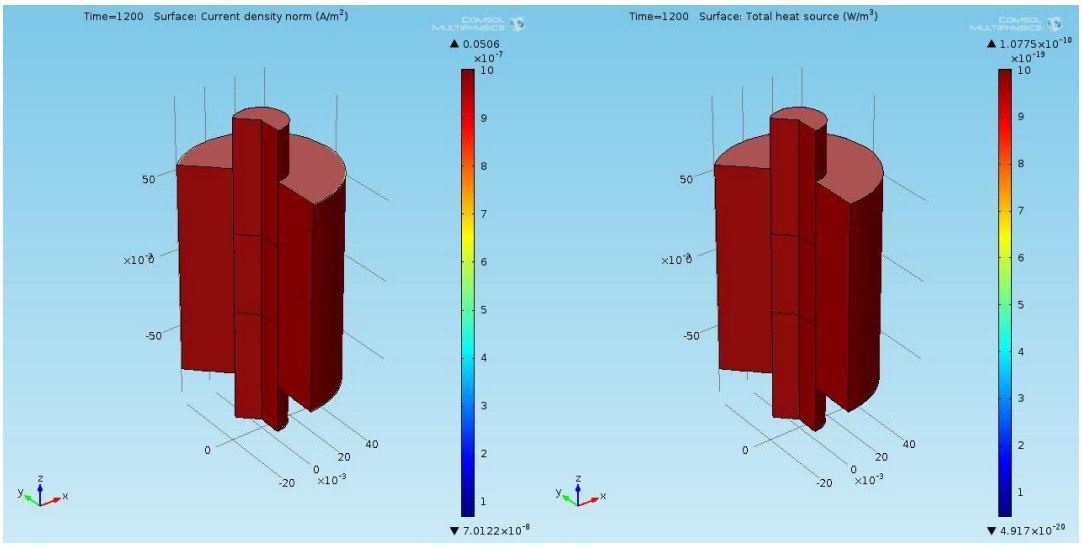

Figure 44: (Left) Current density in the system, & (right) corresponding total heat source in the system at t=1200s

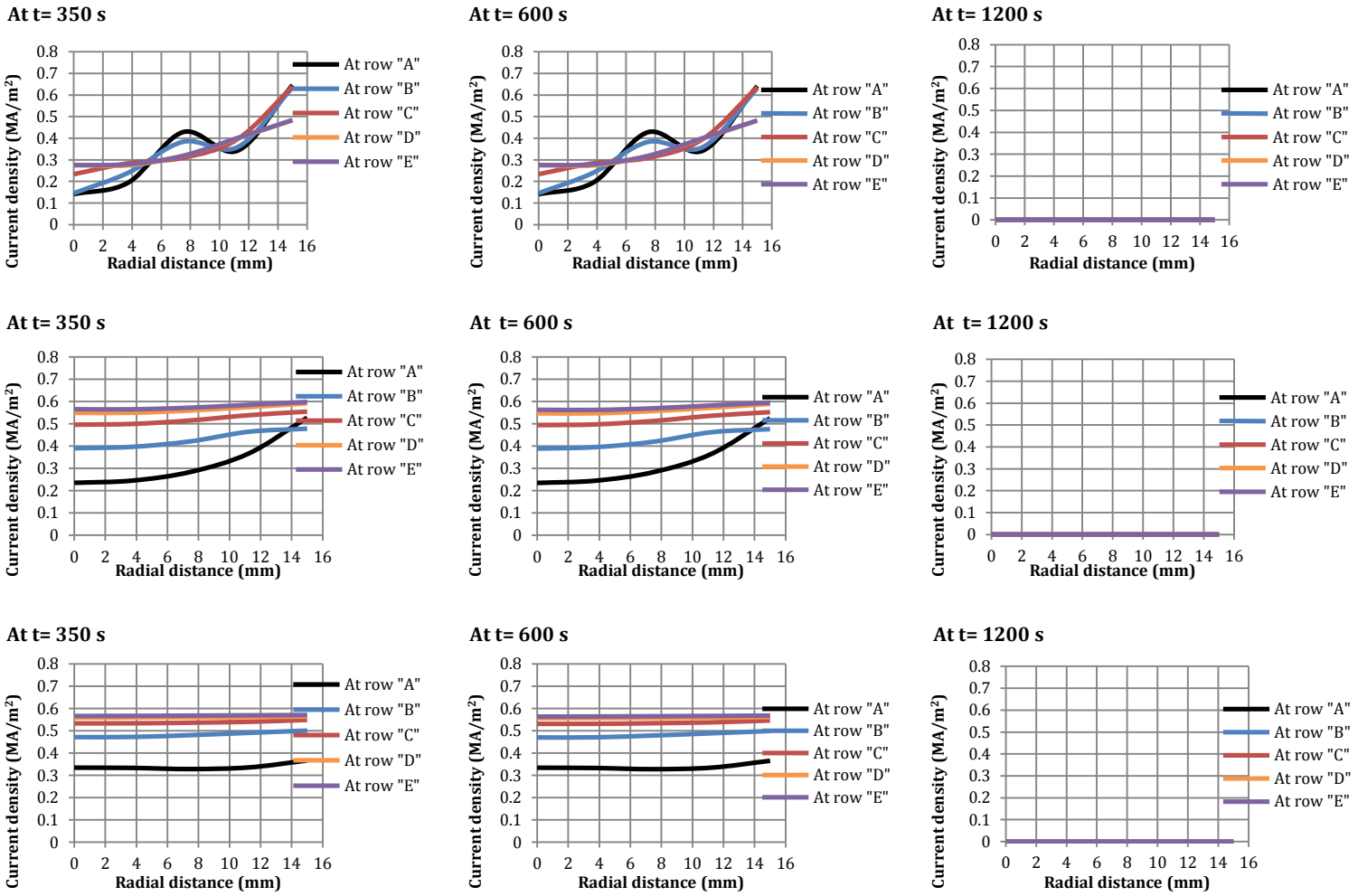

Figure 45: Current density distribution along radius at different axial positions for different sample thicknesses: row1) height=10mm, row 2) height=50mm, & row 3) height=100mm

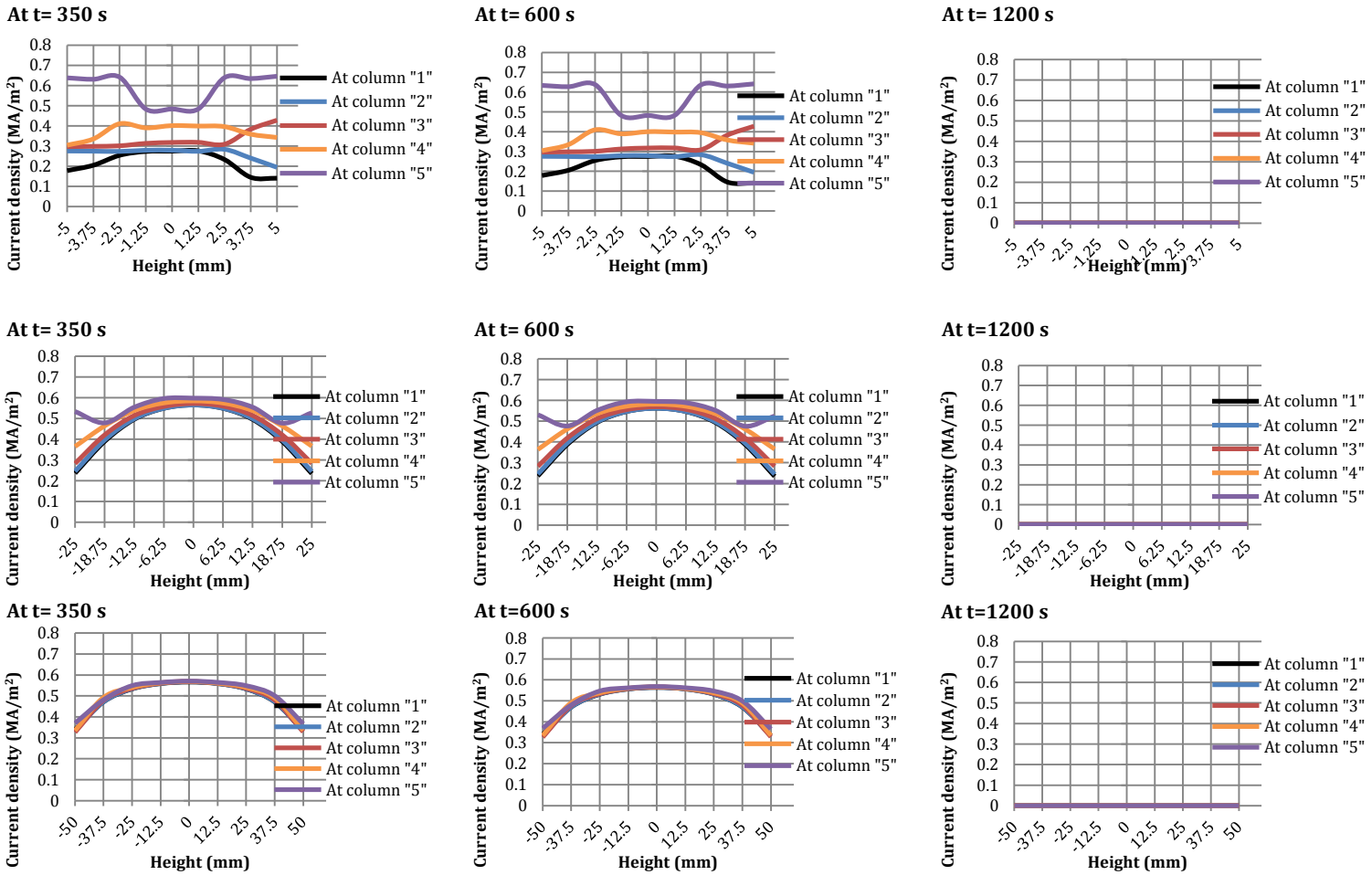

Figure 46: Current density distribution along height at different radial positions for different sample thicknesses: row1) height=10mm, row 2) height=50mm, & row 3) height=100mm

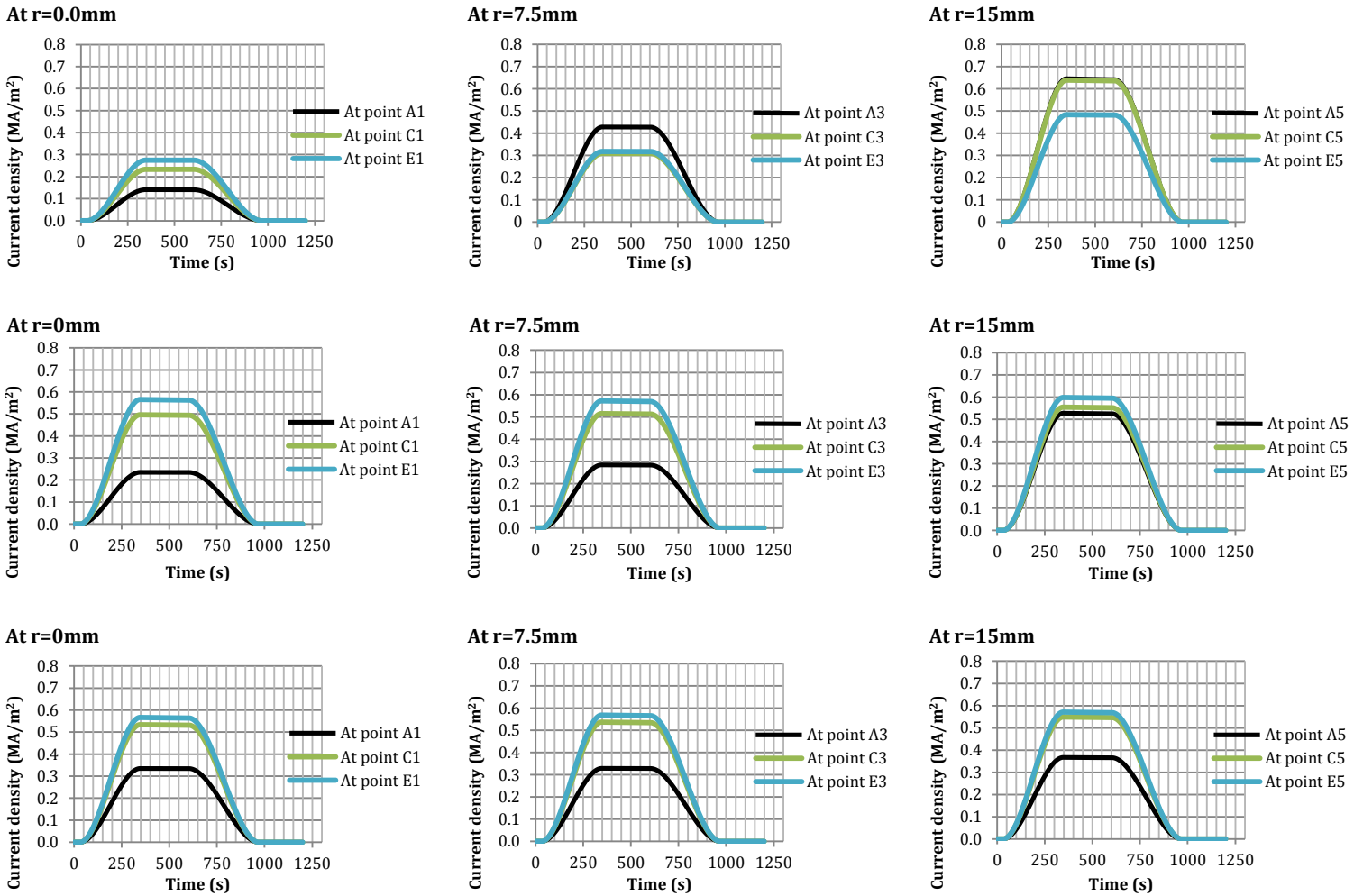

Figure 47: Current density evolution at different locations for different sample thicknesses: row1) height=10mm, row 2) height=50mm, & row 3) height=100mm

Temperature distribution

From Figure 49, it is observed that the temperature in the horizontal planes has decreasing trend along the radius of the sample. The difference between the maximum and minimum temperature in the sample is only few Kelvins – about 0.2 K in 10mm thick sample and 8 K in 100mm sample. In cooling cycle (3^{rd} column in Figure 49), the temperature along the radial distance has the same pattern as that of the heating cycle i.e. reducing along the radius, which is because of the outer surfaces being at lower temperature (convective cooling condition applied at all the outer boundaries of the system). Moreover, this temperature inhomogeneity in cooling cycle is very nominal – less than a Kelvin. Also, from Figure 50, the highest temperature is found in the axially distal planes of the sample. The reason for this maximum temperature in the distal regions of the sample is that that in addition to the joule's heat generation in the sample there is heat conduction from the punch being at higher temperature than the sample. In addition, it is found that in cooling cycle, the temperature becomes almost uniform throughout the sample. This conclusion directs us to the conclusion that *with the increase in the holding time of sintering, there will be more homogeneity in the temperature distribution.*

From Figure 50, it is noticed that the temperature distribution is symmetric about the central *"rθ"* plane. Also, at this plane, the temperature difference along the radius gets reduced with increase in the sample thickness. Furthermore, in heating cycle, the highest overall temperature is found in the center of the top and bottom surfaces of the sample while in cooling cycle, the center of the sample is at the highest temperature and it reduces in any direction accordingly (see Figure 49 & Figure 50).

From Figure 51, it is observed that the temperature at any point in the sample increases till a maximum value and then starts to reduce because of the current supply being switched off and the cooling process. However, the maximum temperature achieved in the sample is lesser in the larger sized samples because of the increase in volume of the sample and the applied current being same.

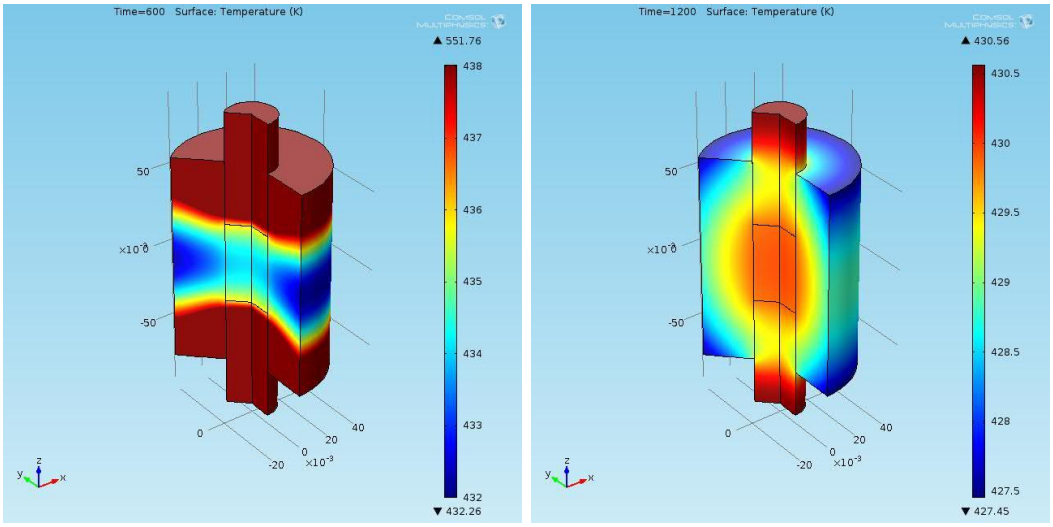

Figure 48: Temperature distribution in the system at different timings at: (left) t=600s, & (right) t=1200s.

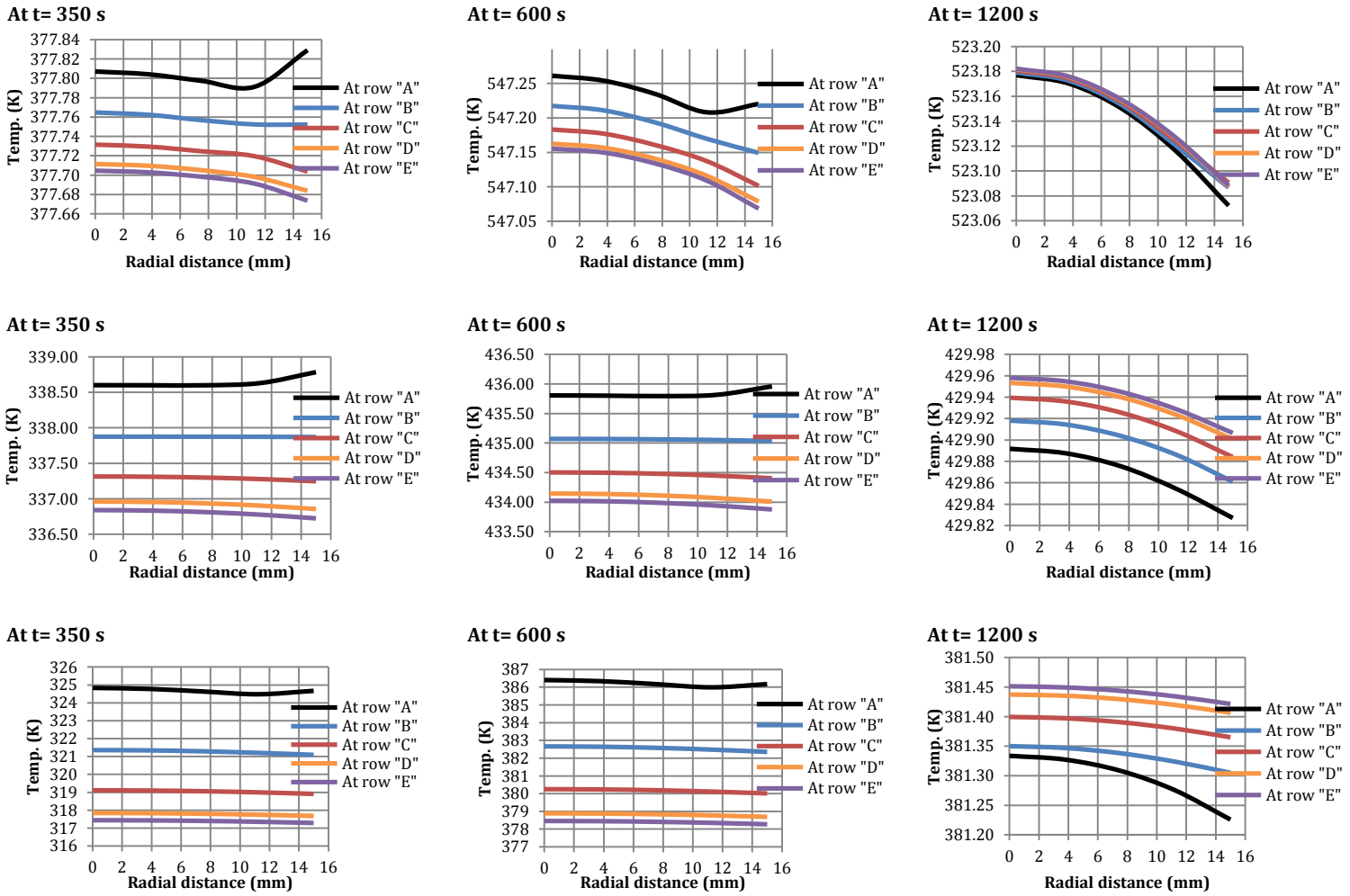

Figure 49: Temperature distribution along radius at different axial positions for different sample thicknesses: row1) height=10mm, row 2) height=50mm, & row 3) height=100mm

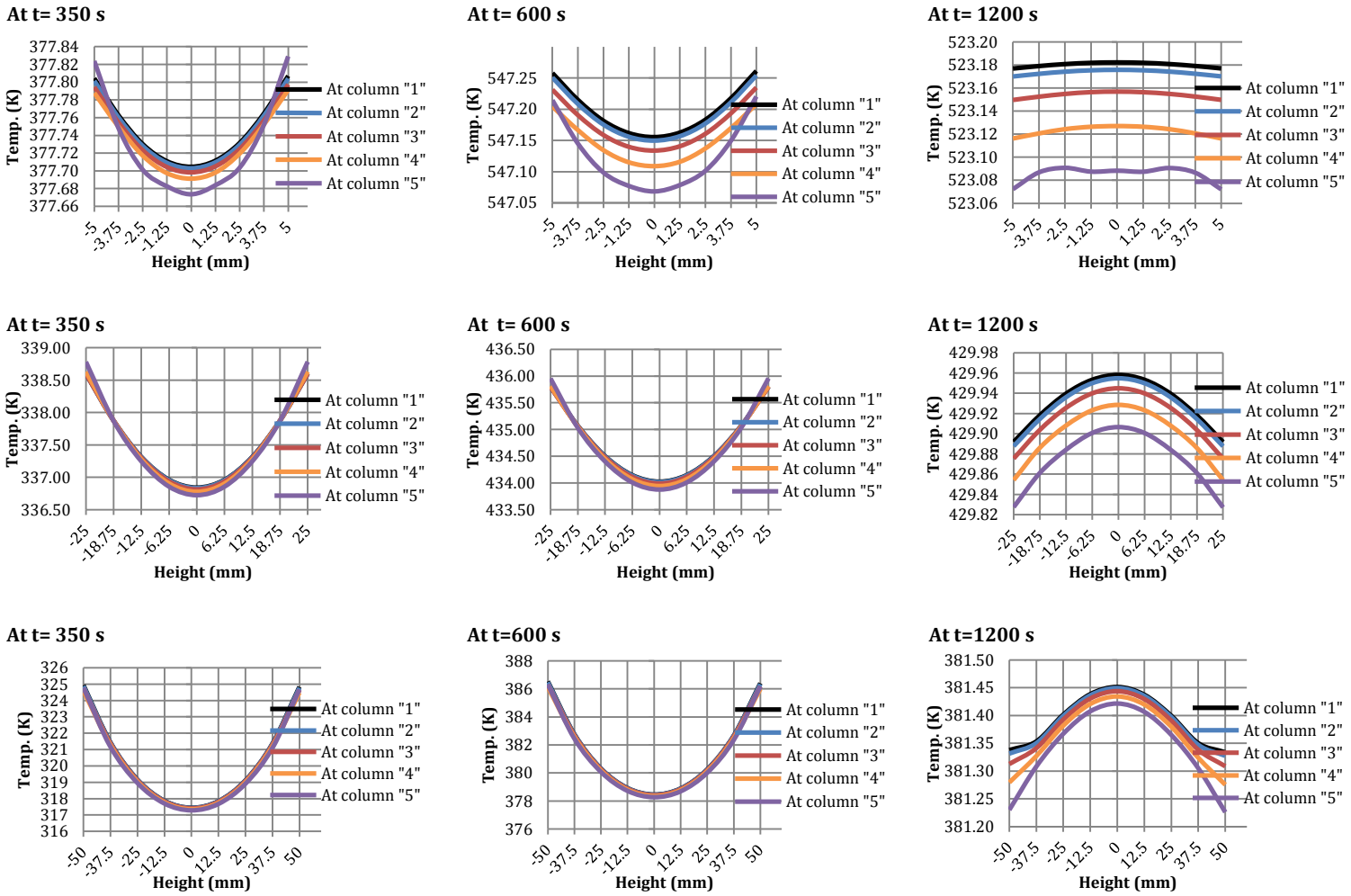

Figure 50: Temperature distribution along height at different radial positions for different sample thicknesses: row1) height=10mm, row 2) height=50mm, & row 3) height=100mm

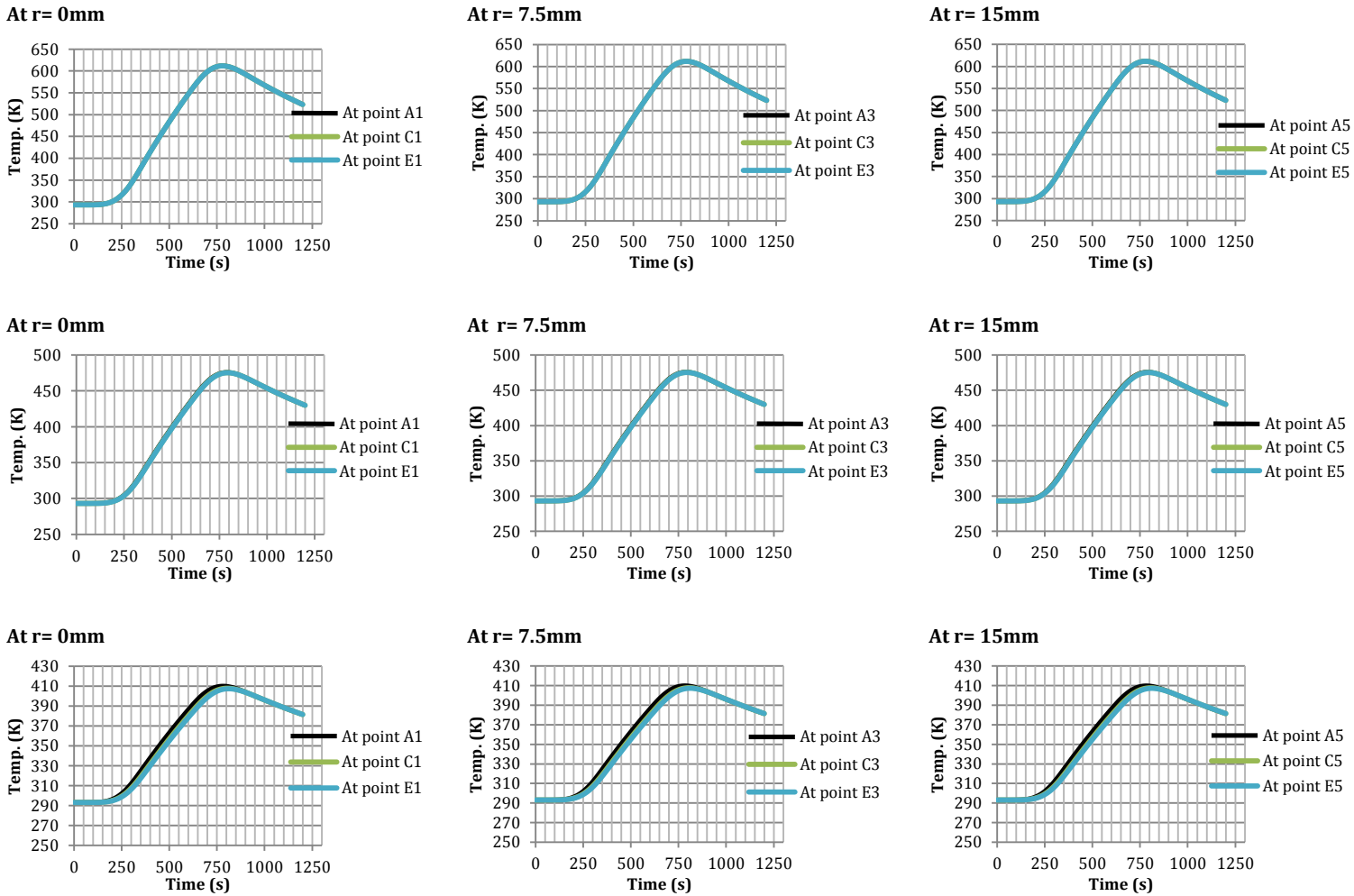

Figure 51: Temperature evolution at different locations for different sample thicknesses: row1) height=10mm, row 2) height=50mm, & row 3) height=100mm

Conclusions

- Maximum current density is found at the extreme radial positions in the central "*rθ*" plane.
- Most of the inhomogeneity in current density is found near the distal regions of the sample along "z" axis.
- The spatial inhomogeneity in the current density is lesser in the larger sized samples than that of the small sized samples.
- The temperature distribution depends upon 1) the distribution of the current in the system which in turns depends upon the electrical conductivities of the system constituents, and 2) the thermal conductivities.
- The maximum temperature achieved in the sample is lower in thicker samples because of the larger volume: the more the volume of the sample the more energy is needed to reach the same temperature.
- Increase in the holding time of sintering results in achievement of more homogeneity in the temperature distribution within the sample.

4.3.4 CASE-II

Sample heights: 1-100 mm with 10 mm steps

Sample diameter: 30 mm

Sample Material: Alumina (electrically insulator)

Current density distribution

From Figure 52, it is noticed that the current density within the sample is almost zero in all the regions at all the times. It is because of the very low (~ 0) electrical conductivity of the alumina.

Temperature distribution

From Figure 53, it is observed in the heating cycle, that the temperature in the sample is increasing in positive radial direction. This trend is because of the fact that there is almost no joules heat generation in the sample in this case and therefore, the only source of temperature rise is the heat conduction from the die and the punches. This difference is only few Kelvins in the lower sized samples while it is substantial – around 15-20 Kelvins – in large sized samples. But this change is more visible in the regions near to the central *"rθ"* plane because of the mentioned region being farther from the highest temperature regions (i.e. punches) in the system. Also, the highest temperature is found in the distal ends of the sample and it reduces towards the center of the sample.

From Figure 54, it is noticed that the temperature distribution is symmetric about the central "*rθ*" plane. In addition, at this plane, the temperature difference is much higher than that at the distal planes. Moreover, the least temperature in the sample is found in the central axis (column 1). In cooling cycle, the center of the sample is at the highest

temperature and it reduces in any direction accordingly (axially as well as radially) because of the heat flowing out of the system now.

From Figure 55, it is observed that the temperature at any point in the sample increases till a maximum value and then starts to reduce as the current supply is switched off. Also, it is quite visible that the maximum temperature achieved in the sample is lower in the larger sized samples as compared to the smaller ones. The reason is the increase in material to be sintered at constant applied conditions.

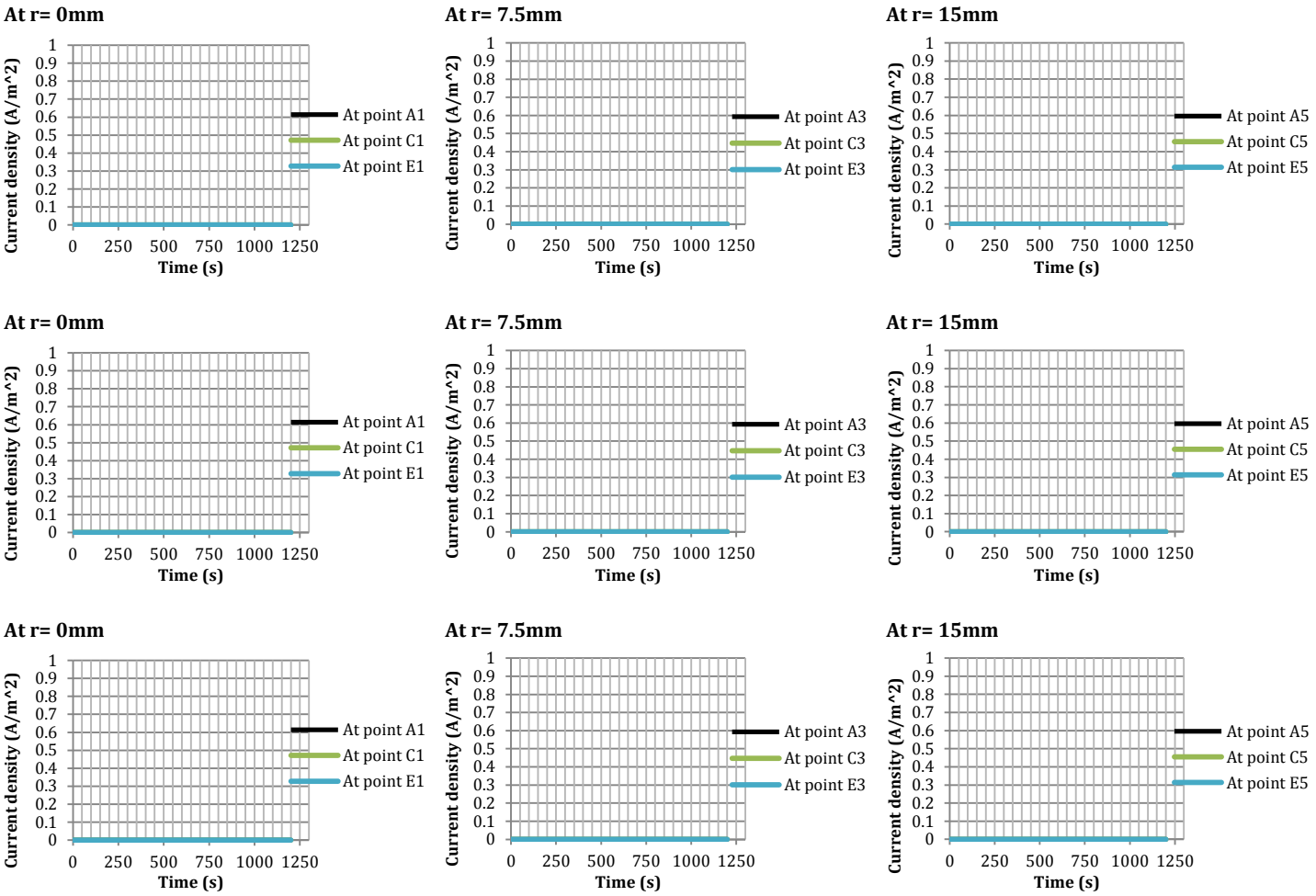

Figure 52: Current density evolution at different locations for different sample thicknesses: row1) height=10mm, row 2) height=50mm, & row 3) height=100mm

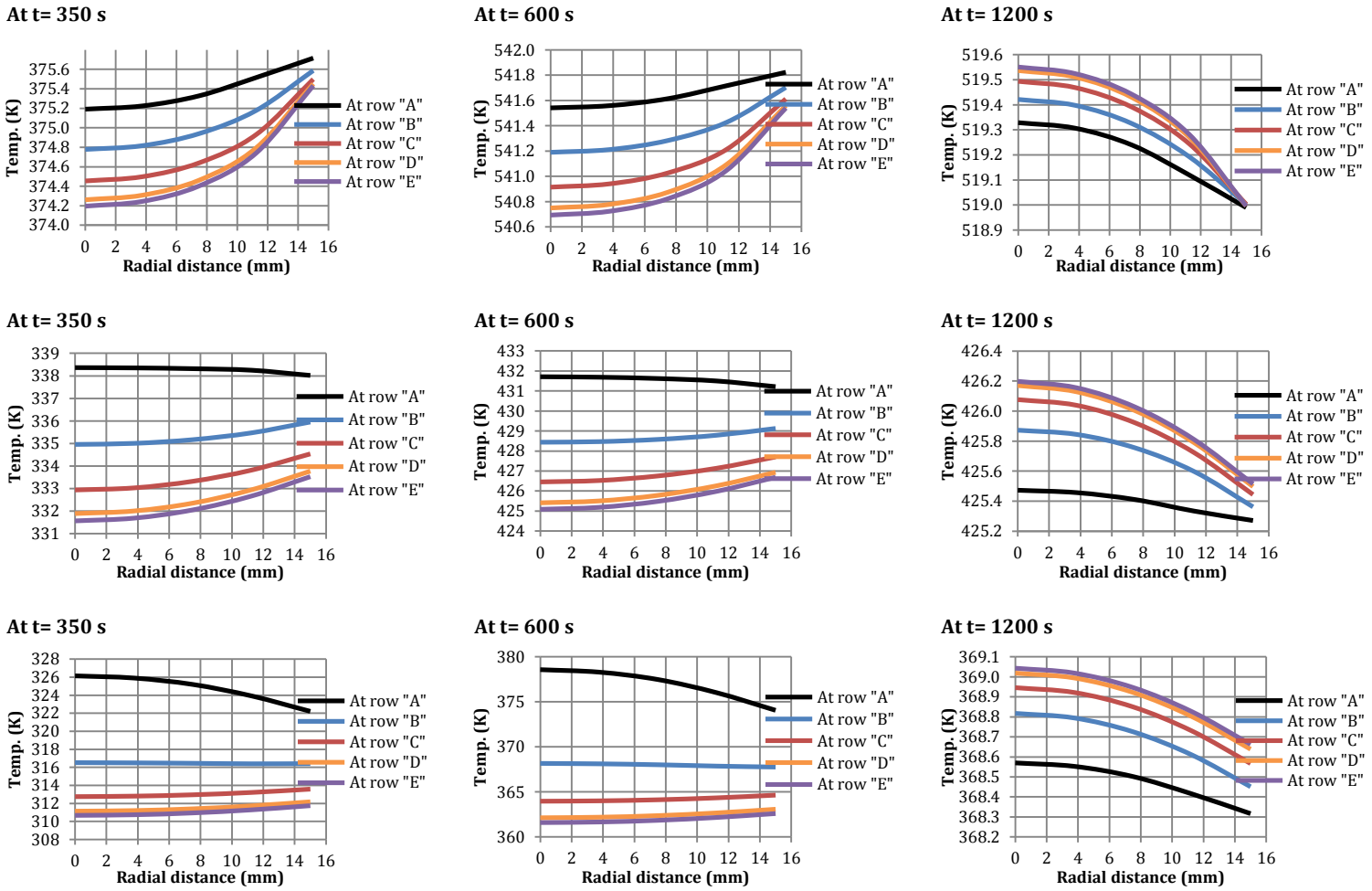

Figure 53: Temperature distribution along radius at different axial positions for different sample thicknesses: row1) height=10mm, row 2) height=50mm, & row 3) height=100mm

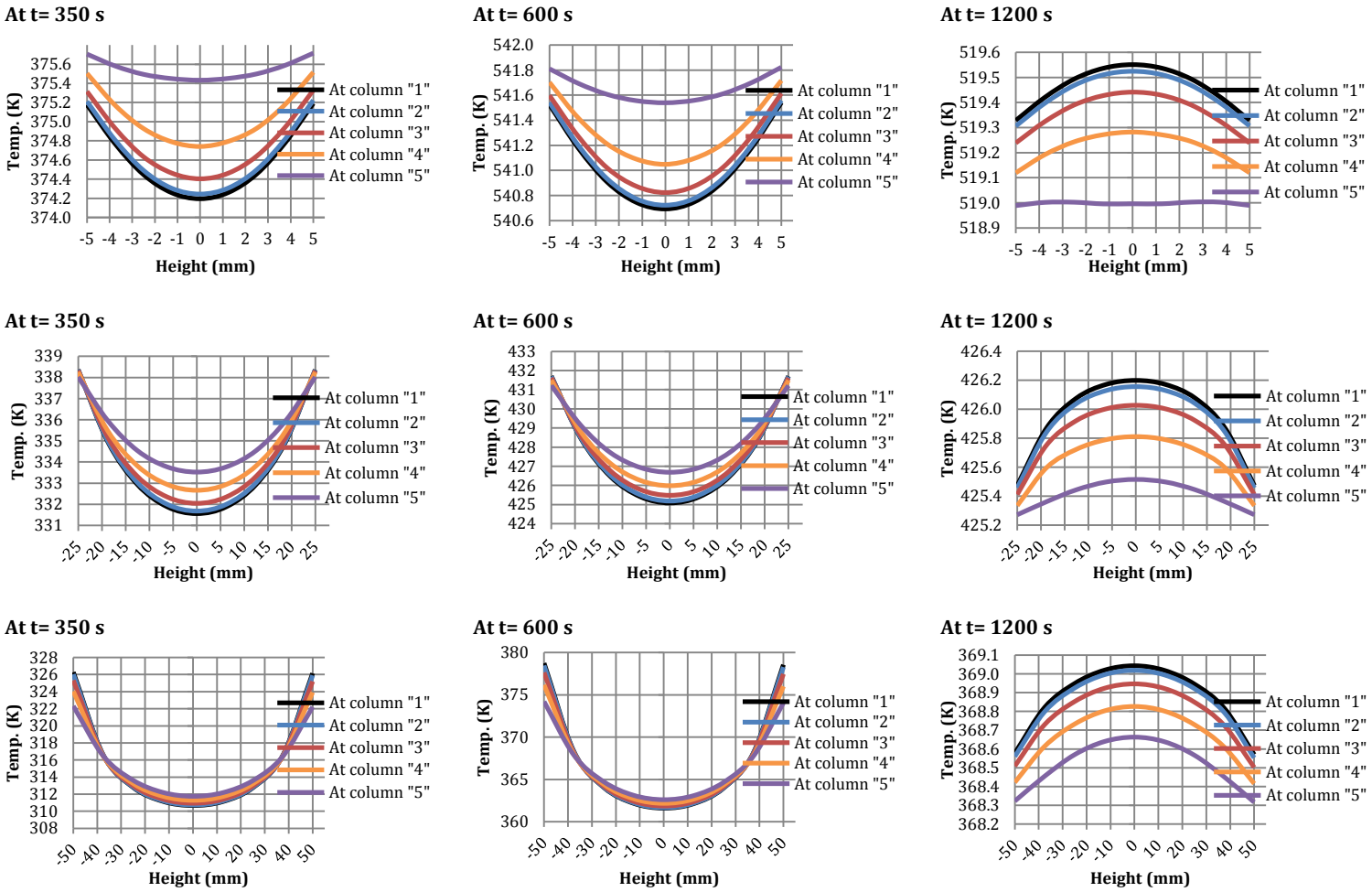

Figure 54: Temperature distribution along height at different radial positions for different sample thicknesses: row1) height=10mm, row 2) height=50mm, & row 3) height=100mm

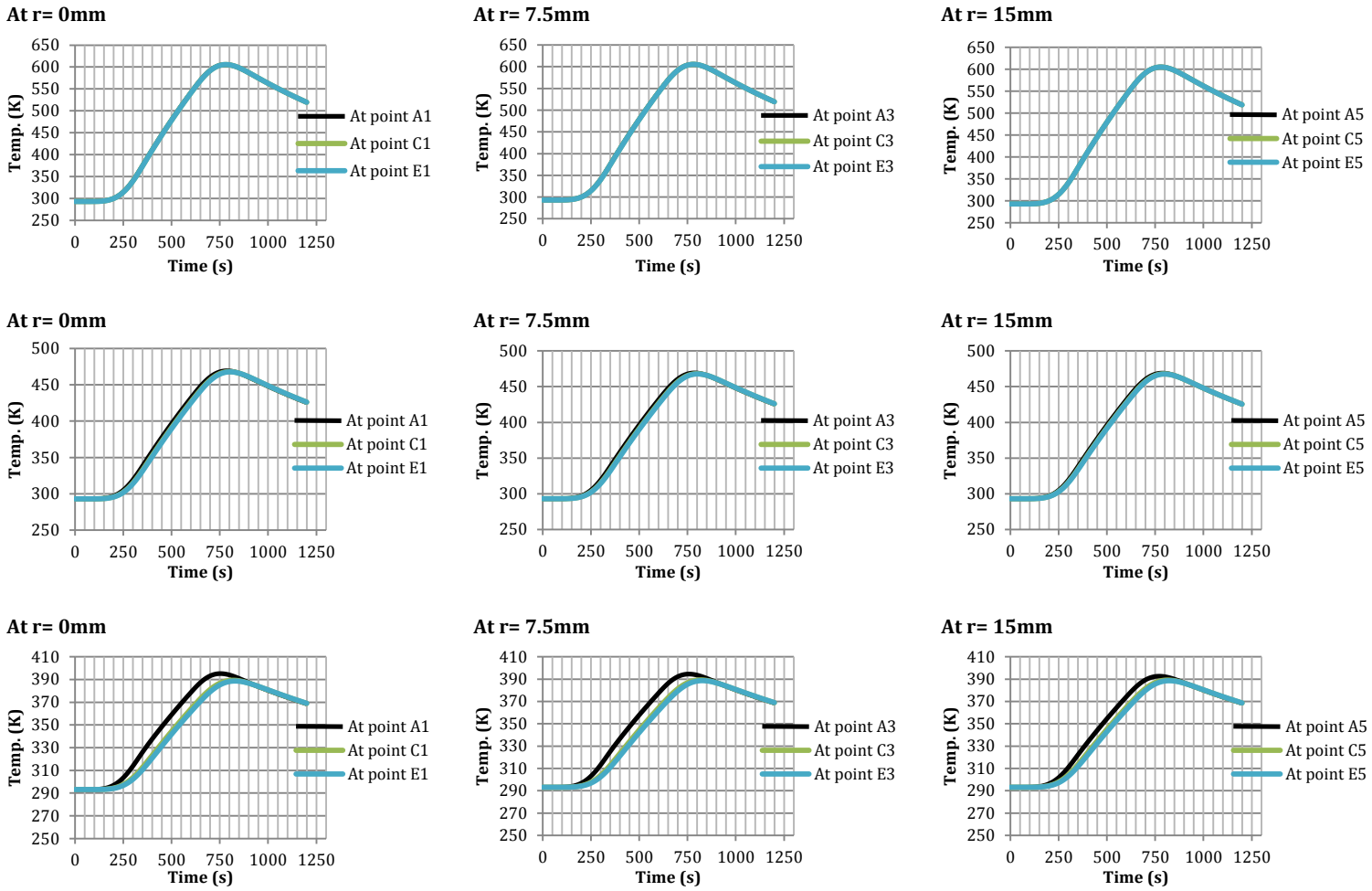

Figure 55: Temperature evolution at different locations for different sample thicknesses: row1) height=10mm, row 2) height=50mm, & row 3) height=100mm

Conclusions

- There is no current flow in the sample because of the almost zero electrical conductivity.
- The only source of temperature rise in the sample is the heat conduction from the die and punches.
- The maximum temperature achieved in the sample is lower in thicker samples because of the larger volume: the more the volume of the sample the more energy is needed to reach the same temperature.
- In comparison to the case-I, the maximum temperature achieved in the sample is lower because of the elimination of the joule's heat generation in the sample.

CHAPTER 5

STRUCTURAL MODEL

5.1 INTRODUCTION

The purpose of the structural model is to calculate all the types of stresses developed in the die-punch- sample system. The basic phenomenon behind this is the applied uniaxial pressure and the stresses generated due to the temperature variations (along with some contribution from the friction between the domains which are in contact with each other). So, the stresses developed have very strong relationship with that of the applied pressure and the temperature. Therefore, the accuracy of the model is very significant in accurate structural behavior prediction of the system.

As far as the structural modeling of the Spark Plasma Sintering process is concerned, only very few attempts have been made. In our model, we used COMSOL Multiphysics to simulate the SPS process. In the following paragraphs the developed model will be explained in adequate detail.

5.2 THE MODEL

5.2.1 Mathematical model

In the SPS process, in addition to the applied structural loads, there is a strong coupling between the structural and the thermal fields because of the temperature dependence of the physical properties of the materials. In the following lines, the mathematical equations which govern this process are discussed.

The constitutive relationship for sintering of a non-linear viscous porous material is given by [38]:

$$\sigma_{ij} = \frac{\sigma(W)}{W}\left[\varphi\dot{\varepsilon}_{ij} + \left(\psi - \frac{1}{3}\varphi\right)\dot{e}\delta_{ij}\right] + P_L\delta_{ij} \tag{14}$$

Where σ_{ij} is the externally applied stress,

$\sigma(W)$ is the effective stress,

W is the equivalent strain rate,

φ is the normalized shear viscosity modulus,

ε_{ij} is the strain rate components,

ψ is the normalized bulk viscosity modulus,

$\dot{e}$ is the shrinkage rate,

δ_{ij} is the kronekar's delta, and

P_L is the effective sintering stress

Also, we have,

$$\varphi = (1-\theta)^2$$

$$\psi = \frac{2(1-\theta)^3}{3\theta}$$

$$P_L = \frac{3\alpha}{r_o}(1-\theta)^2$$

Where, α is the surface energy, and

r_o is the average particle radius

Now, for the power law creep (PLC) case, we have:

$$\sigma(W) = AW^m$$

and

$$W = \frac{1}{\sqrt{1-\theta}}\sqrt{\varphi\dot{\gamma}^2 + \psi\dot{e}^2}$$

Where $\dot{\gamma}$ is the shape change rate and can be expressed as:

$$\dot{\gamma} = \sqrt{2\left(\dot{\varepsilon}_{xy}{}^2 + \dot{\varepsilon}_{xz}{}^2 + \dot{\varepsilon}_{yz}{}^2\right) + \frac{2}{3}\left(\dot{\varepsilon}_x{}^2 + \dot{\varepsilon}_y{}^2 + \dot{\varepsilon}_z{}^2\right) - \frac{2}{3}(\dot{\varepsilon}_x\dot{\varepsilon}_y + \dot{\varepsilon}_x\dot{\varepsilon}_z + \dot{\varepsilon}_y\dot{\varepsilon}_z)}$$

The shrinkage rate can also be expressed in the following form

$$\dot{e} = \dot{\varepsilon}_x + \dot{\varepsilon}_y + \dot{\varepsilon}_z$$

Combining all the above equations in (14), the constitutive equation becomes:

$$\sigma_{ij} = \frac{A\left(\frac{1}{\sqrt{1-\theta}}\sqrt{\varphi\left(\sqrt{2\left(\dot{\varepsilon}_{xy}{}^2+\dot{\varepsilon}_{xz}{}^2+\dot{\varepsilon}_{yz}{}^2\right)+\frac{2}{3}\left(\dot{\varepsilon}_x{}^2+\dot{\varepsilon}_y{}^2+\dot{\varepsilon}_z{}^2\right)-\frac{2}{3}(\dot{\varepsilon}_x\dot{\varepsilon}_y+\dot{\varepsilon}_x\dot{\varepsilon}_z+\dot{\varepsilon}_y\dot{\varepsilon}_z)}\right)^2+\psi(\dot{\varepsilon}_x+\dot{\varepsilon}_y+\dot{\varepsilon}_z)^2}\right)^m}{W}\Big[(1-\theta)^2\dot{\varepsilon}_{ij} + \left(\frac{2(1-\theta)^3}{3\theta} - \frac{1}{3}(1-\theta)^2\right)\dot{e}\delta_{ij}\Big] + \frac{3\alpha}{r_o}(1-\theta)^2\delta_{ij} \quad (15)$$

5.2.2 Model in COMSOL Multiphysics

The model developed in this section is the same as that of the one discussed in chapter 4 except the addition of the structural mechanics node.

Applied Conditions

In addition to the boundary conditions discussed in the electrical-thermal model, there are several structural boundary conditions that are applied in the developed model. These boundary conditions are discussed in the following paragraphs.

Applied load:

The structural load applied in the system is of two types: one is the uniaxial pressure applied (boundary load) at boundary # 11 and second is the thermal load. The applied pressure is a function of time which increases initially up to a maximum value, then stays constant for some time and after that it is removed (see Figure 31). In addition, in the system, boundary # 2 is fixed and continuity of the field is maintained in all the domains. Moreover, at all the contact surfaces, friction is defined. In addition, the material is assumed to behave elastically.

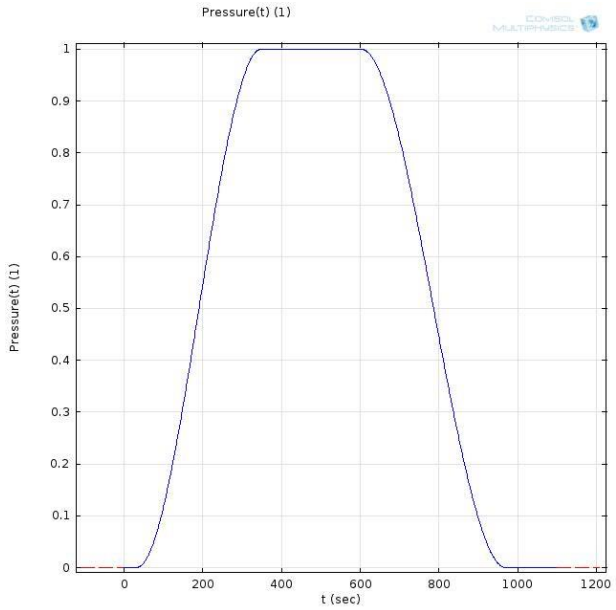

Figure 56: The Applied pressure

5.3 RESULTS AND DISCUSSIONS

In this study, the model comprised of four domains – a die, a sample and two punches. They were assembled using contact pairs at all the matching boundaries to define the contact mechanisms at these boundaries. In the following paragraphs, at first, the validation of the developed model will be discussed which will be followed by two case studies: Case-I and Case-II. Case-I deals with the electrical-thermal-mechanical model for an electrically conductive material (Aluminum) and Case-II deals with the electrical-thermal-mechanical model for an electrically insulator material (Alumina).

5.3.1 Validation of the developed model

In order to validate the model (only qualitatively), the results of the developed model are compared with the published literature in the following paragraphs. The developed model is for the aluminum sample.

Axial stress distribution

From Figure 57, it is noticed that the axial stress is compressive in nature and increasing along the radius of the sample. Similar trend has been reported by F. Mechigel et. al [32].

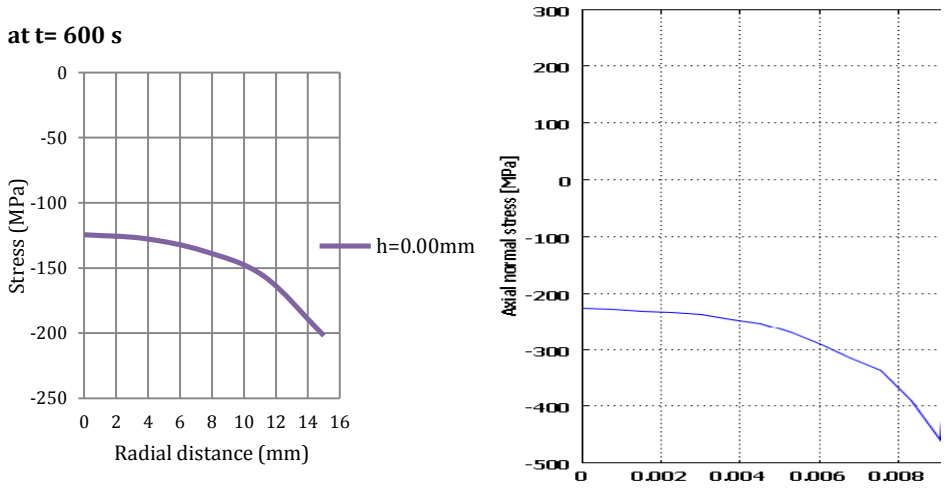

Figure 57: Axial stress distribution along the radius in the sample: Left) this study, & Right) F. Mechighel et. al [32]

Radial stress distribution

From Figure 58, it is noticed that the radial stress is compressive in nature and increasing along the radius of the sample. Similar trend has also been reported by F. Mechigel et. al [32].

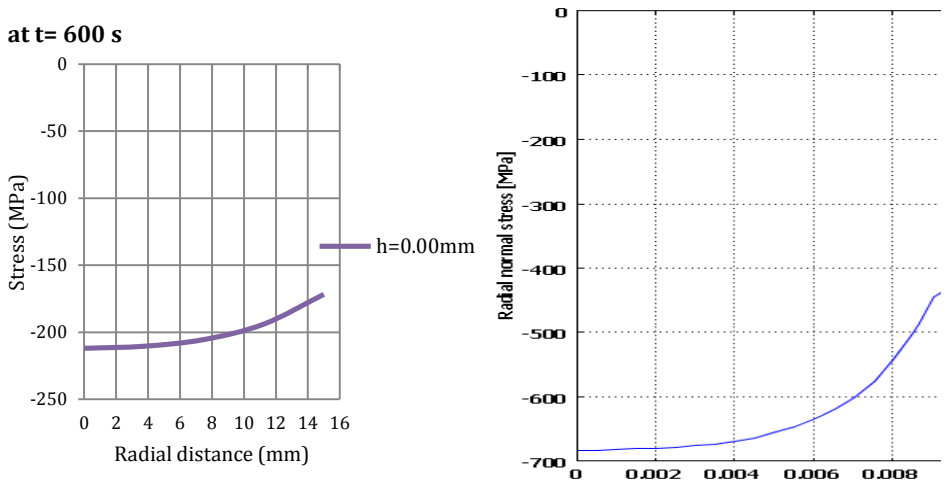

Figure 58: Radial stress distribution along the radius in the sample: Left) this study, & Right) F. Mechighel et. al [32]

5.3.2 Case-I

Sample heights: 0, 50 & 100 mm

Sample diameter: 30 mm

Sample Material: Aluminum (electrically conductor)

Current density distribution

From Figure 59, in 10mm sample, it is observed that the current density is having a decreasing trend in either direction along z-axis. In addition, with increase in the thickness of the sample, the difference along axial direction increases with the maximum difference in the top and bottom regions of the samples (because of the same reasons explained in section 4.3.3). Also, the maximum and minimum values of the current densities are independent of the sample sizes and are found at the center and edges of the samples respectively. The reason for this is that the maximum current density is dependent upon the applied current which is constant. As far as the time dependency is concerned, the current density is uniform at 350s and 600s but zero at the end of the process (as the applied current is switched off). From Figure 60, it is noticed that the current density shows increasing trend near the edge of the sample in radial direction in 10mm sample in all the horizontal planes. In rest of the region, it is uniform. But in larger samples the current density is uniform throughout the radius with the only exception in the boundaries of the sample adjacent to the punches. In addition, from Figure 61, it is observed that in all the regions of the sample, the current density in the sample adopts the same profile as that of the applied current.

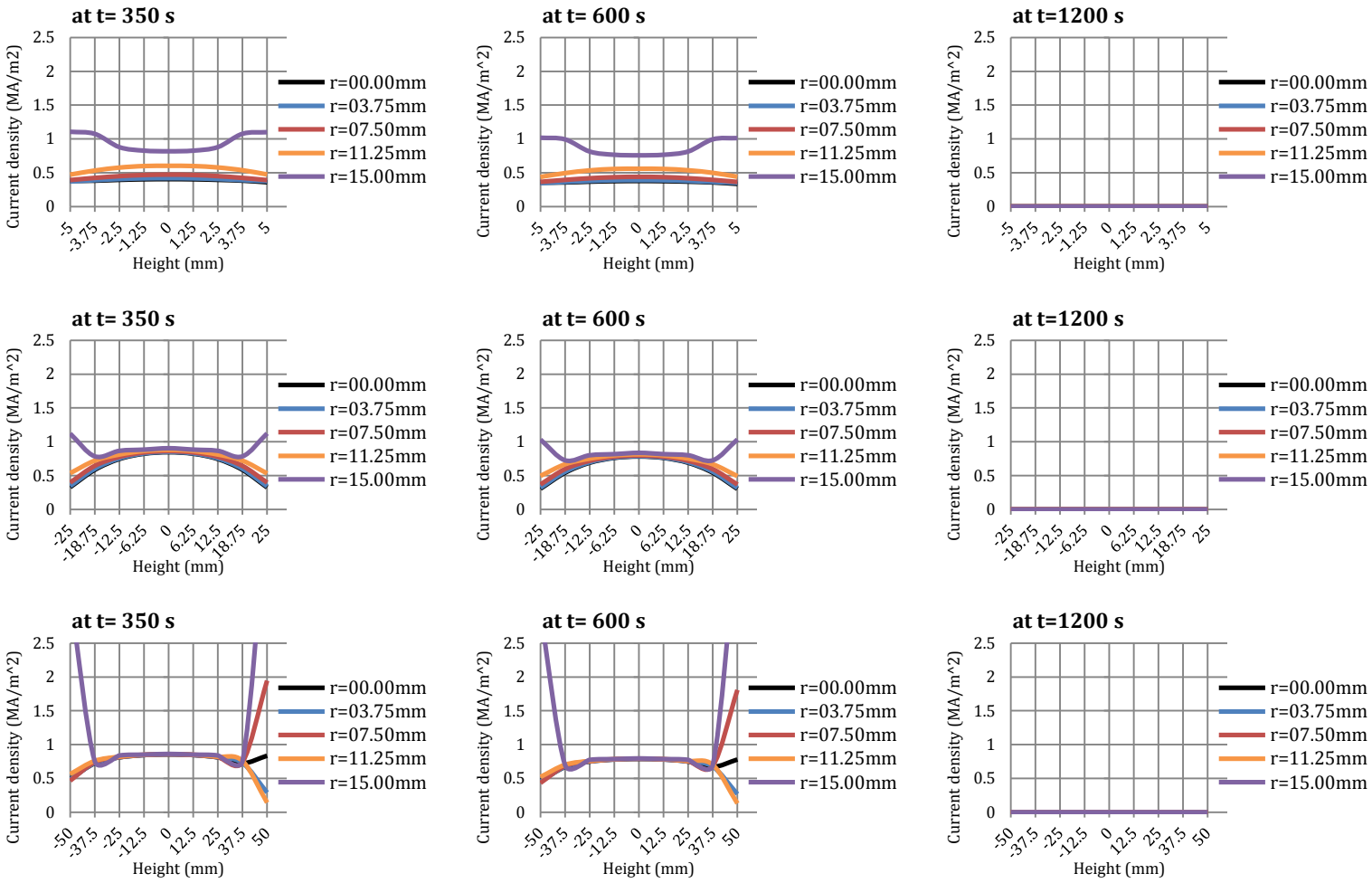

Figure 59: Current density along height at different radial positions for different sample thicknesses: row1) height=10mm, row 2) height=50mm, & row 3) height=100mm

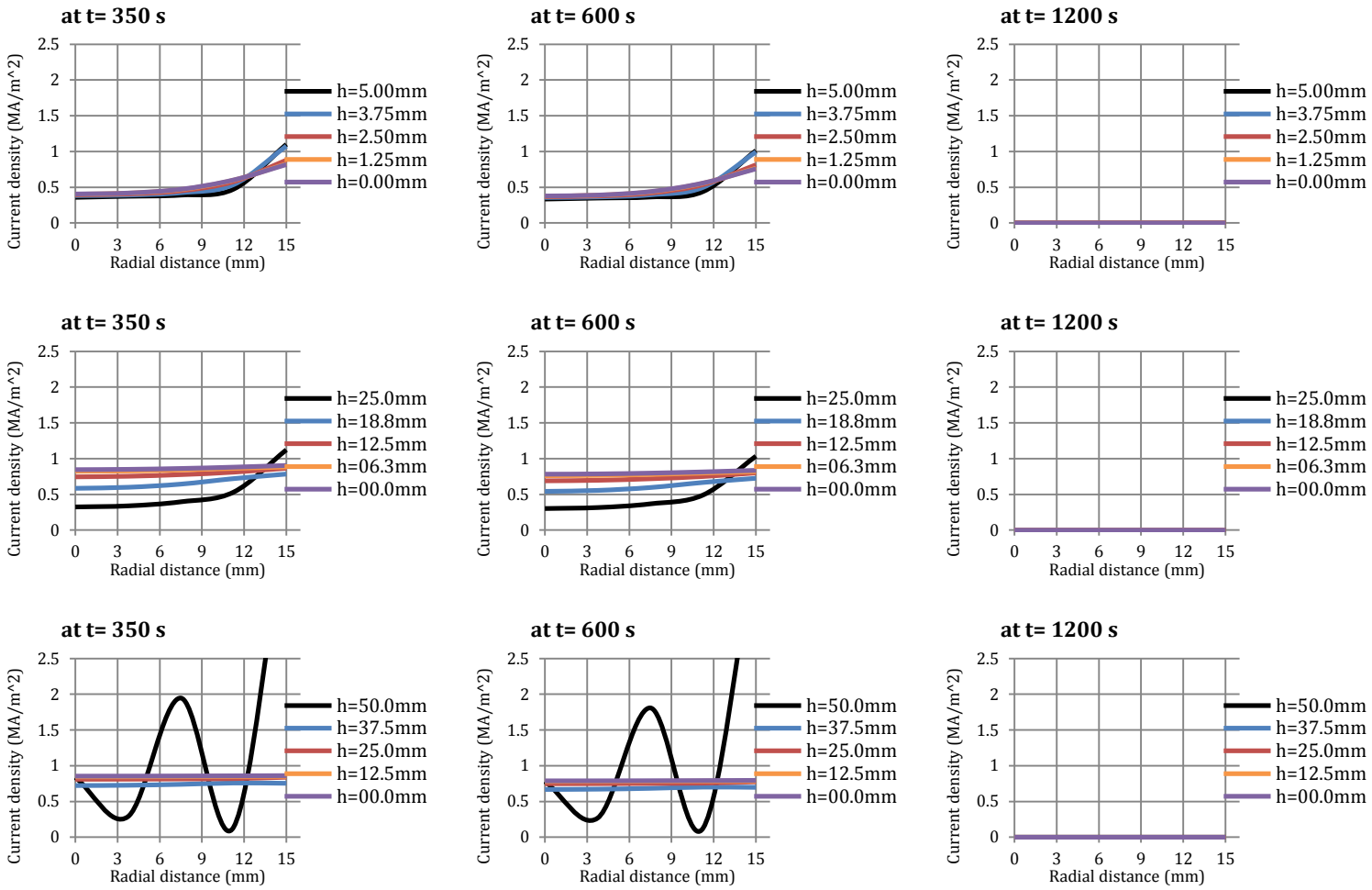

Figure 60: Current density along radius at different axial positions for different sample thicknesses: row1) height=10mm, row 2) height=50mm, & row 3) height=100mm

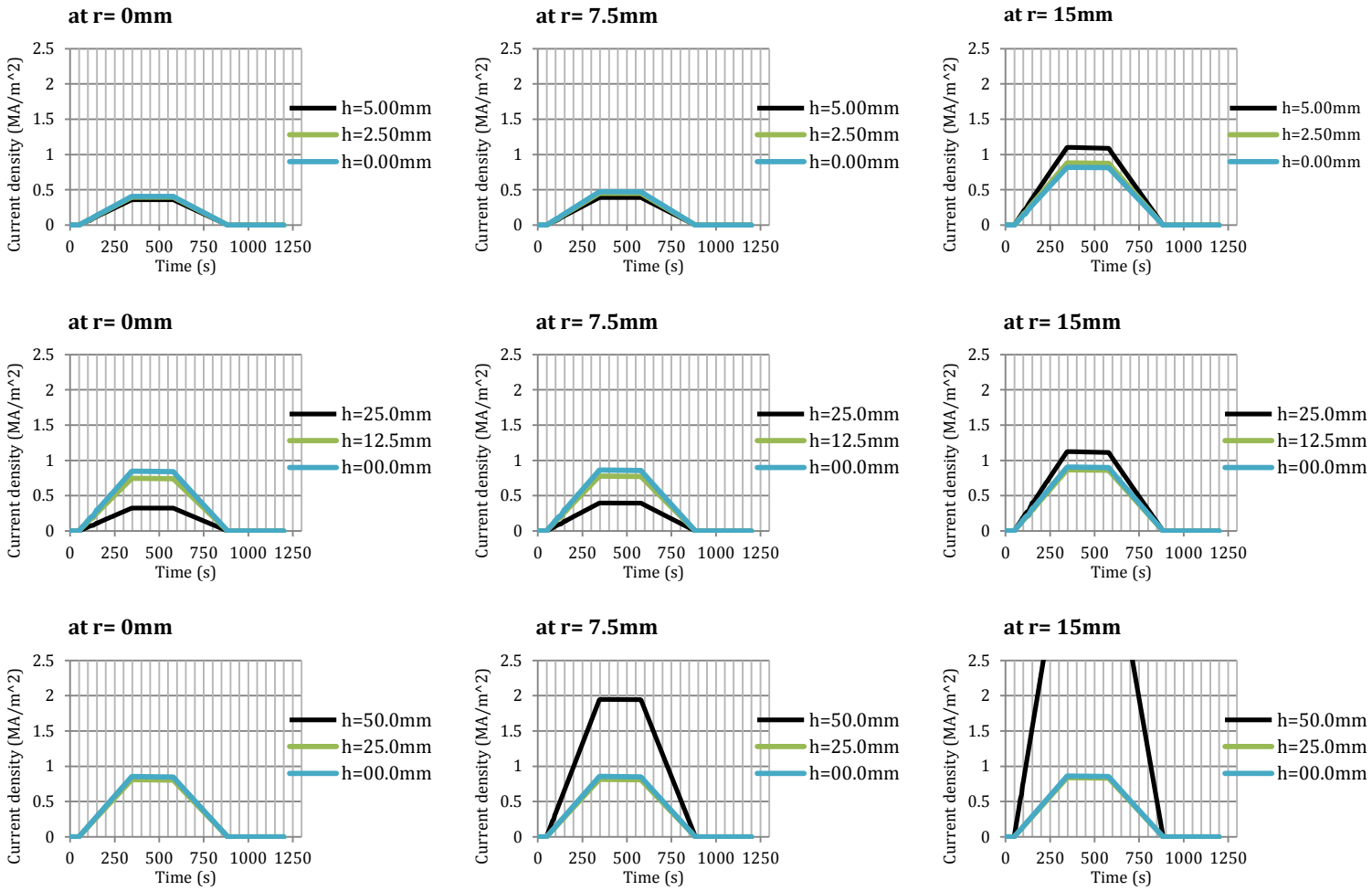

Figure 61: Current density evolution at different axial positions for different sample thicknesses: row1) height=10mm, row 2) height=50mm, & row 3) height=100mm

Temperature distribution

From Figure 62, it is observed that that there exists some temperature difference in the sample along the height. But this difference is very nominal – less than 1K – in the smaller sized (10mm) samples whereas it is of appreciable value – about 12K – in 100mm samples. Moreover, the trend along axial direction is increasing in all the planes in heating cycles while decreasing in the cooling cycles (t=1200s). In addition, the temperature becomes almost uniform at the end of the process which leads us to the conclusion that increase in holding time results in lesser inhomogeneity in the sample. It is also noticed that the temperature is lesser in the radially outward planes in the sample (see Figure 63) but this difference almost vanishes in the larger sized samples. From this discussion, it comes out that the highest temperature is found at the center of the top and bottom surfaces of the samples. It is because of the reason that, in the whole system, the highest temperature region is in the punches and hence there exists heat conduction from punches into the sample. In addition, it is also noted that the temperature first increases, reaches a maximum value and then, after switching off of the applied current, starts reducing (see Figure 64). One of the important observations is that as the sample size increases, the maximum temperature achieved in the sample is reduced. The reason behind this is that, the amount of energy needed in larger sized samples is higher as compared to the required energy in the smaller samples.

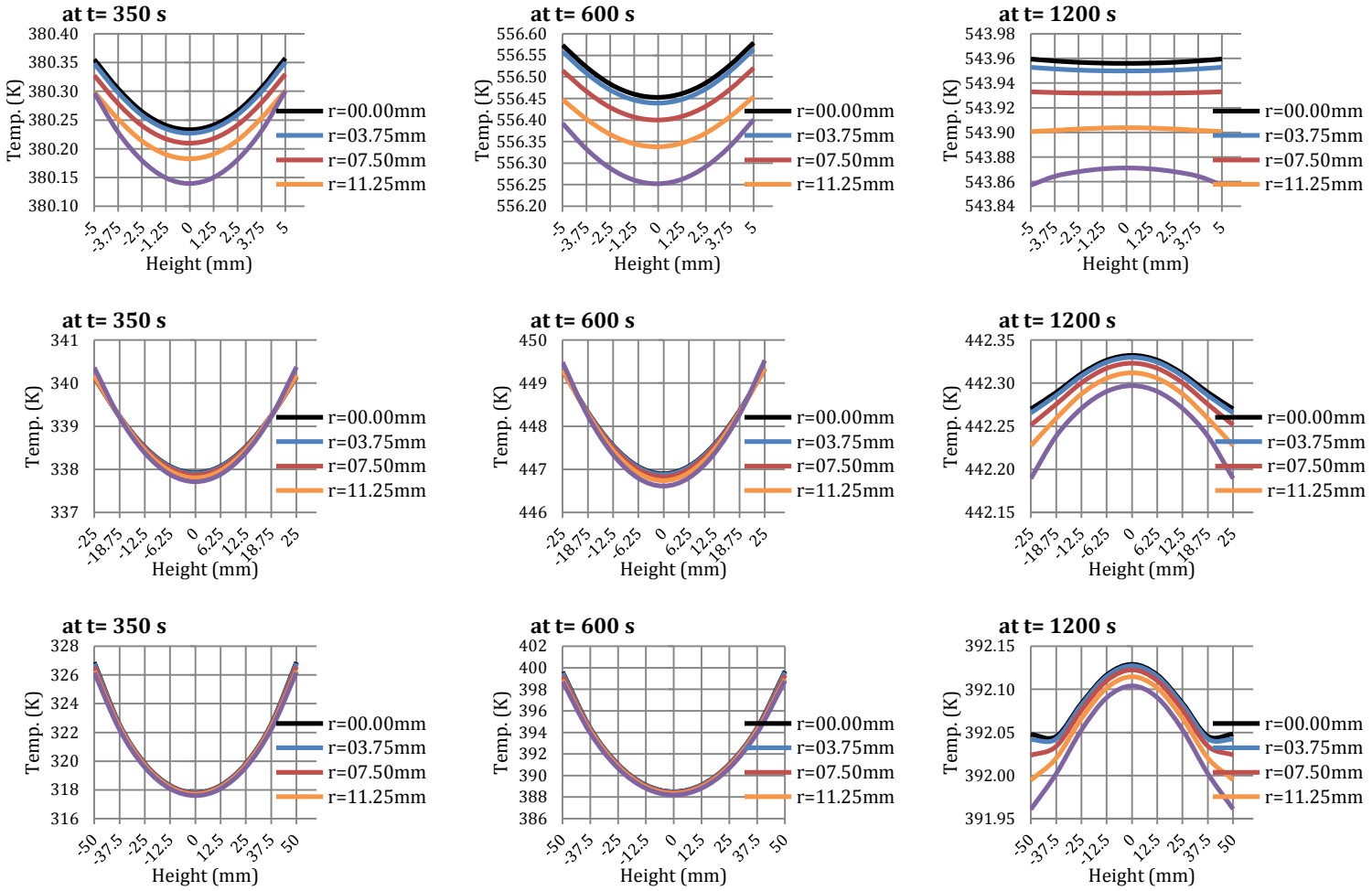

Figure 62: Height-wise temperature distribution at different radial positions for different sample thicknesses: row1) height=10mm, row 2) height=50mm, & row 3) height=100mm

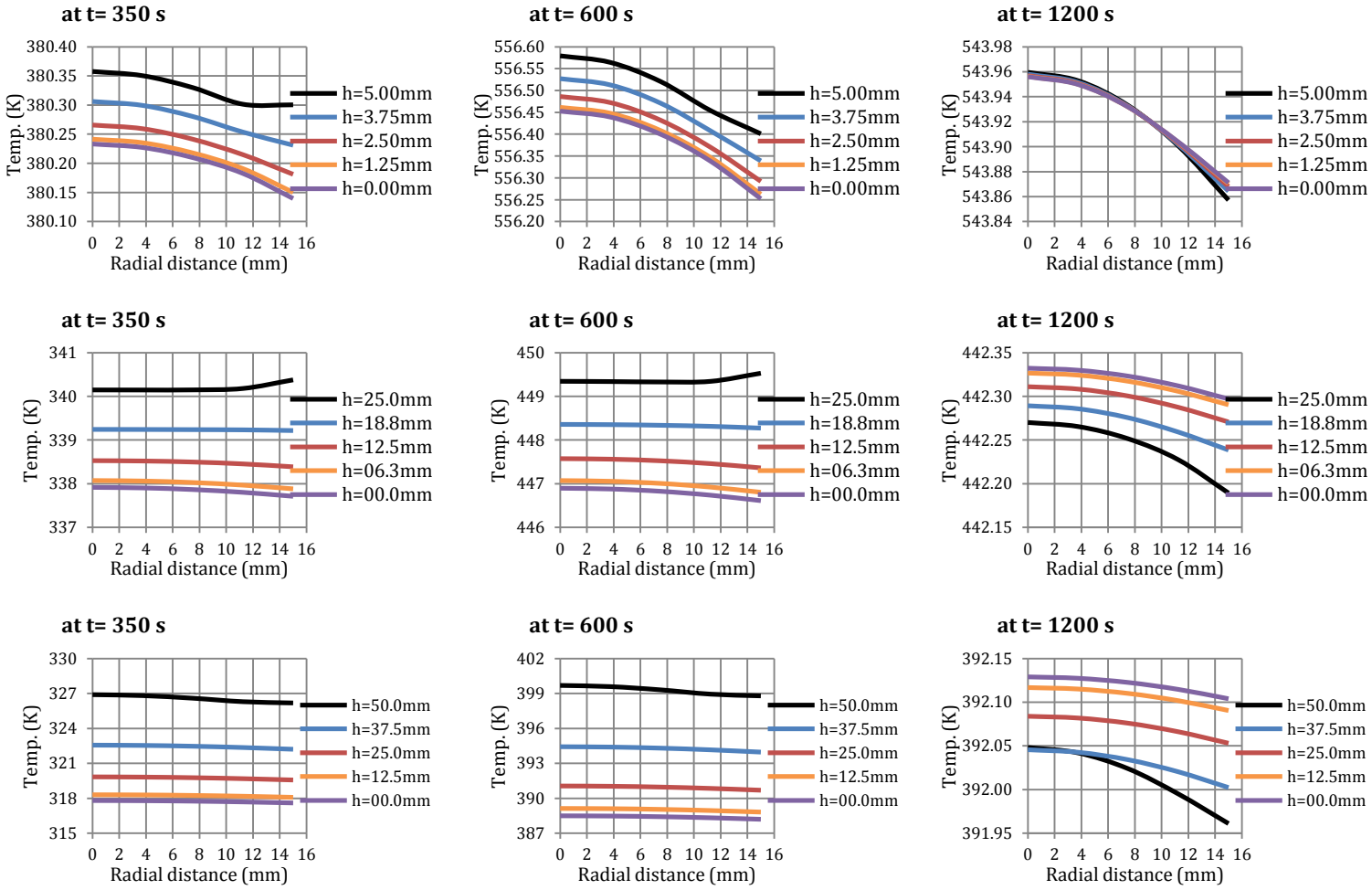

Figure 63: Radius-wise temperature distribution at different radial positions for different sample thicknesses: row1) height=10mm, row 2) height=50mm, & row 3) height=100mm

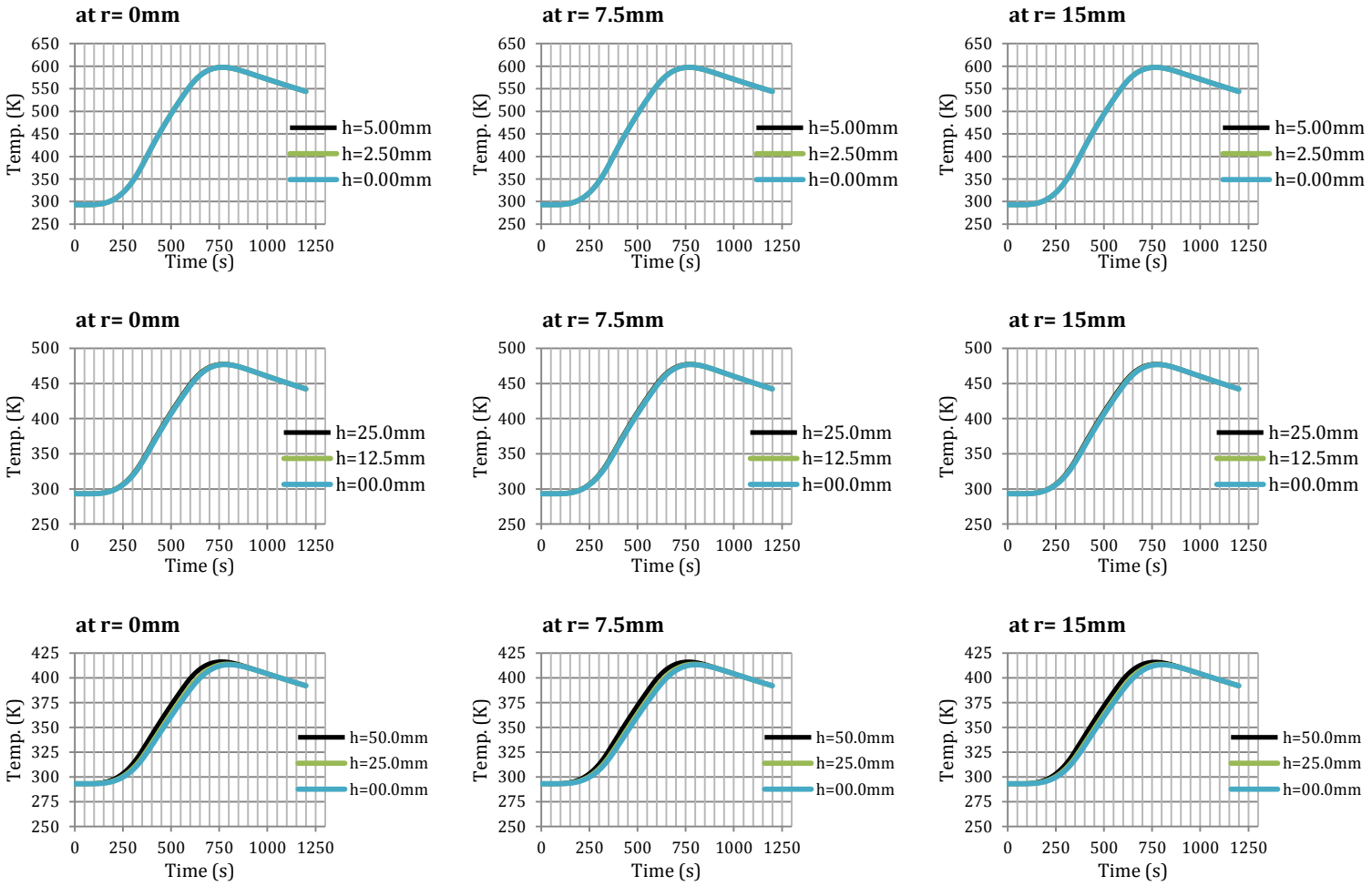

Figure 64: Temperature evolution at different axial positions for different sample thicknesses: row1) height=10mm, row 2) height=50mm, & row 3) height=100mm

Von-Mises stress distribution

From Figure 65, it is observed that von-Mises stress developed in the samples varies along the axial direction with the maximum variation at the top and bottom surfaces of the sample. In other words, von-Mises stress is relatively uniform in the central region (axially) of the sample. The maximum von-Mises stress is found in the layer at the sample-die boundary and its value is decreasing with the increase in the size of the sample – ~180MPa in 10mm sample and ~100MPa in 100mm sample. Again, it is because of the same reason that as the sample volume increases, more energy is needed to achieve the same deformation. Moreover, as these values are higher than the yield stress of aluminum, plastic strains will be present in the sample and hence the elastic behavior assumption is not enough and it is needed to include the plastic behavior of the material in the model. Furthermore, the von-Mises stress is found to be symmetric about the center of the sample in axial direction in smaller samples but in larger samples the stress developed in the top surface (pressure application surface) is more than that of the bottom surface. In addition, from Figure 66, it is noticed that there exists variation in von-Mises stress along the radius and the maximum value is found in the top surface of the sample. Moreover, as the size of the sample increases, the stresses in the sample become more and more uniform with an exception in the sample's top surface where it shows more variation. From this discussion, it is inferred that, in the whole sample, the maximum von-Mises stress is developed at the maximum radial as well as axial positions i.e. the edges of the sample and hence they are the critical regions as far as plasticity is concerned. Also, from Figure 67, it is observed that the von-Mises stress increases with time till certain maximum value and then starts to decline slightly in all the regions of the sample.

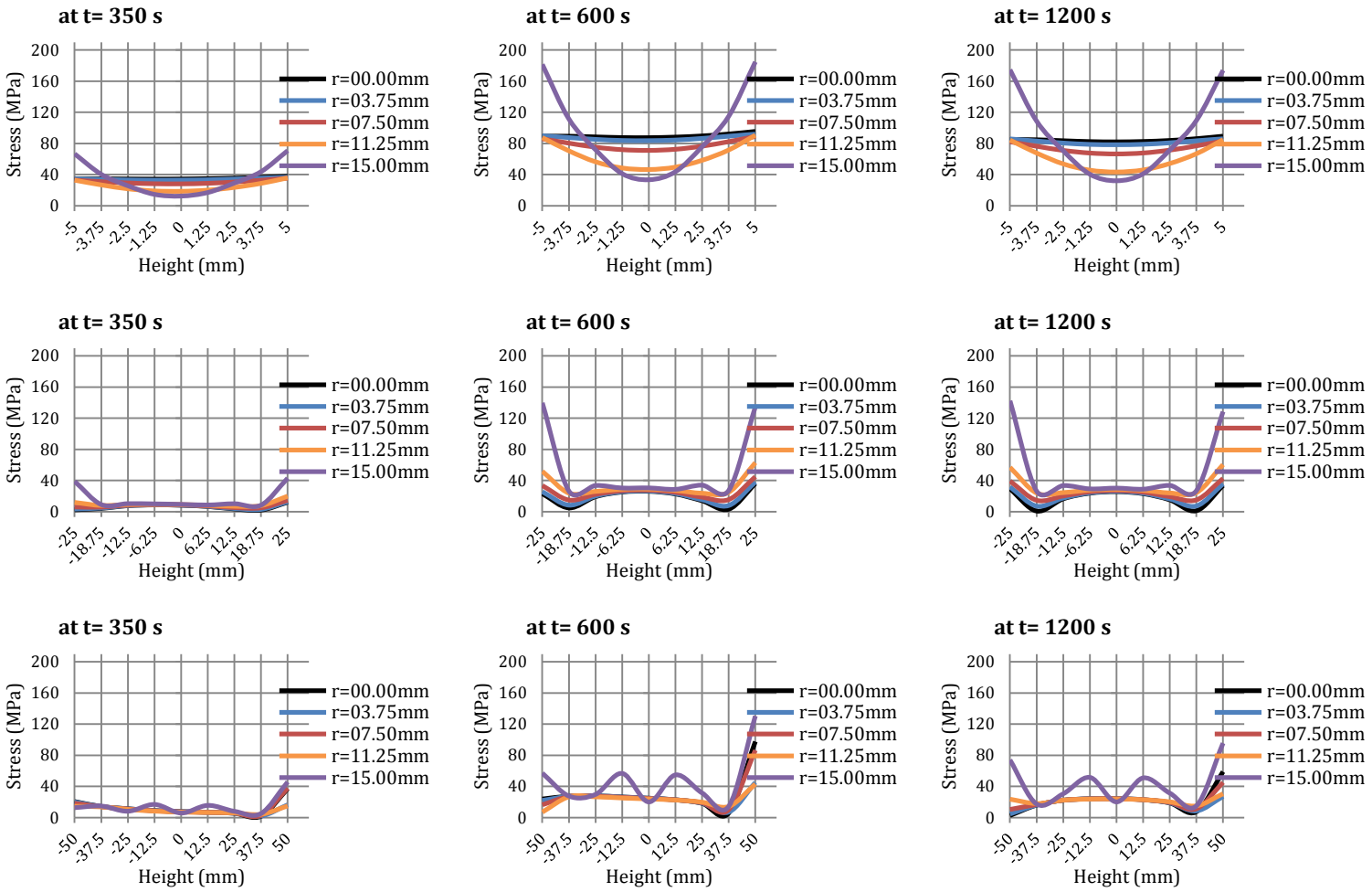

Figure 65: Height-wise von-Mises stress distribution at different radial positions for different sample thicknesses: row1) height=10mm, row 2) height=50mm, & row 3) height=100mm

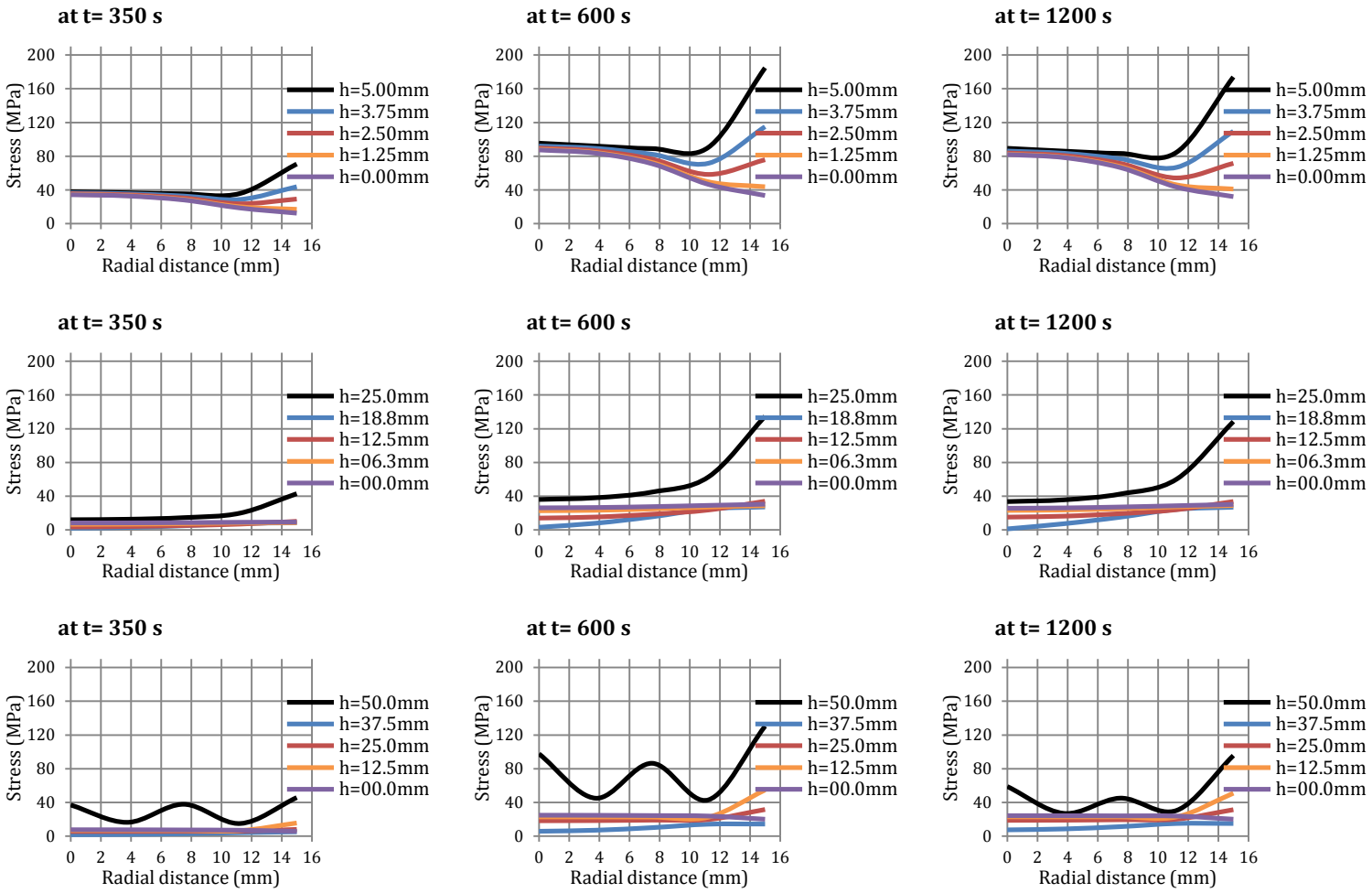

Figure 66: Radius-wise von-Mises stress distribution at different axial positions for different sample thicknesses: row1) height=10mm, row 2) height=50mm, & row 3) height=100mm

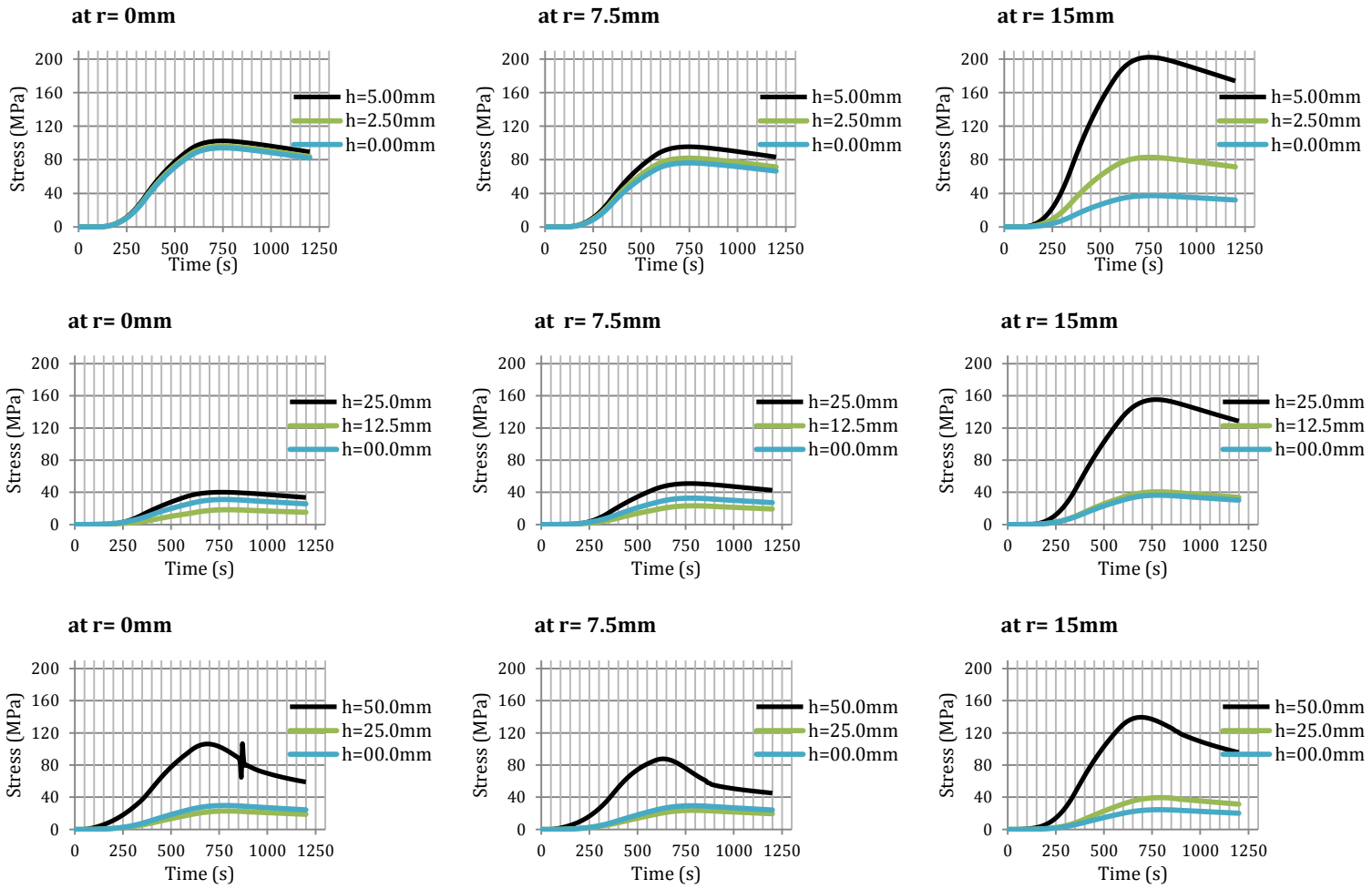

Figure 67: Von-Mises stress evolution at different axial positions for different sample thicknesses: row1) height=10mm, row 2) height=50mm, & row 3) height=100mm

Axial stress distribution

From Figure 68, it is noticed that the axial stresses developed in the sample are compressive in nature (because of the applied pressure). In the axial direction, these stresses are generally uniform and symmetric about the central "rθ" plane (z=0). But this behavior is slightly deviated in the larger samples – the stresses are either more or less at the top surface of the sample as compared to the other regions. Moreover, the stresses in the smaller samples are larger than the stresses developed in the larger samples. The maximum axial stress developed is ~ -200MPa in the 10mm sample. In radial directions, from Figure 69, the stresses are increasing along the radius in the smaller samples while it is almost uniform in the larger samples. In larger samples, the only exception is in the top surface of the sample where the stresses vary along the radius. Moreover, the stresses developed in different horizontal planes are almost same in the central regions of the sample while they have differences near the sample-die boundary. From these discussions, it is deduced that, in the central regions of the samples, the stresses are almost homogenous while the inhomogeneity is mostly found at all the edges/boundaries of the samples. Furthermore, the axial stresses also evolve in the same manner as that of the von-Mises stresses i.e. increase to a maximum value and then reduce slightly. In addition, some stresses remain in the sample at the end of the process.

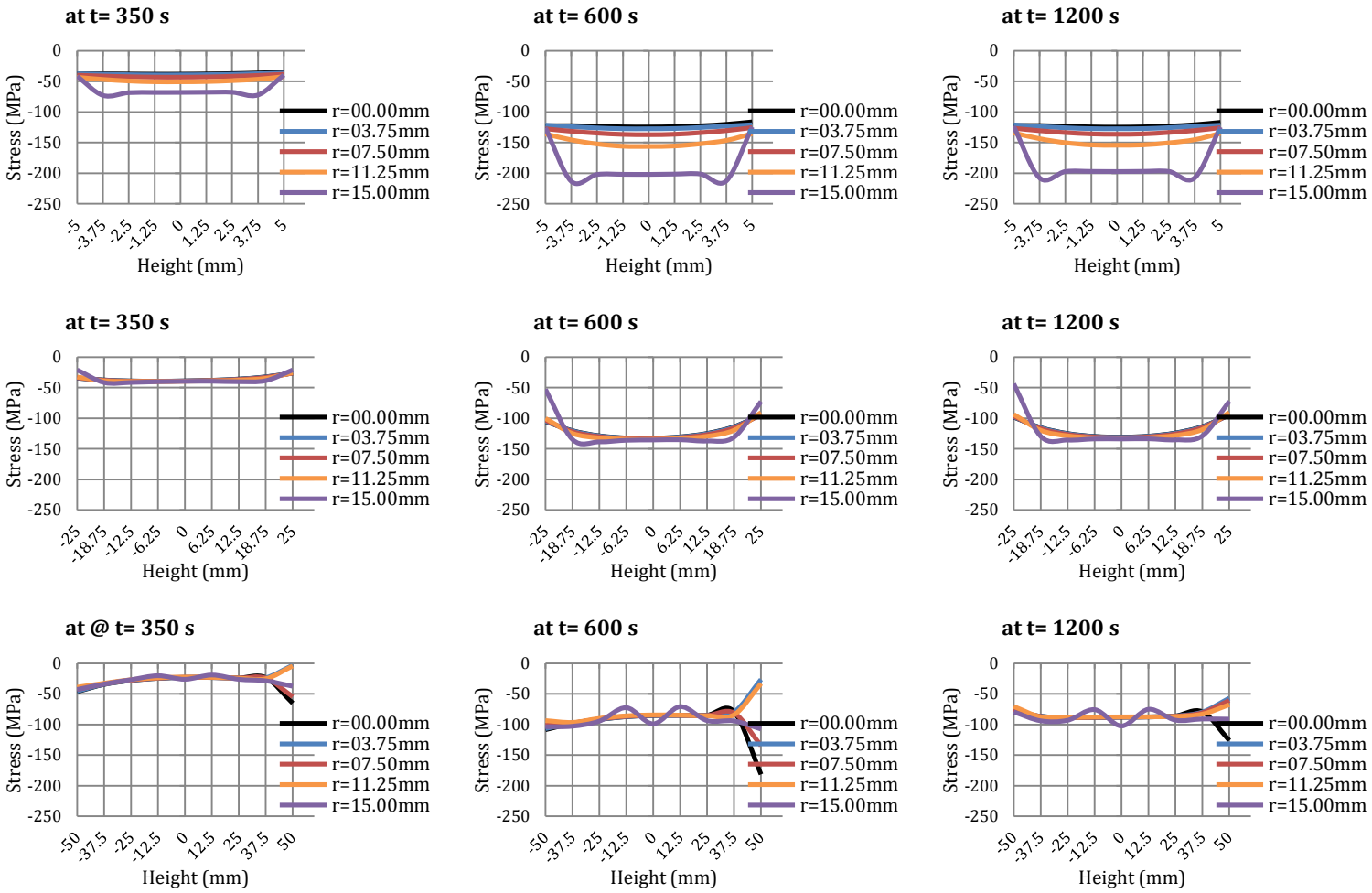

Figure 68: Height-wise axial stress distribution at different radial positions for different sample thicknesses: row1) height=10mm, row 2) height=50mm, & row 3) height=100mm

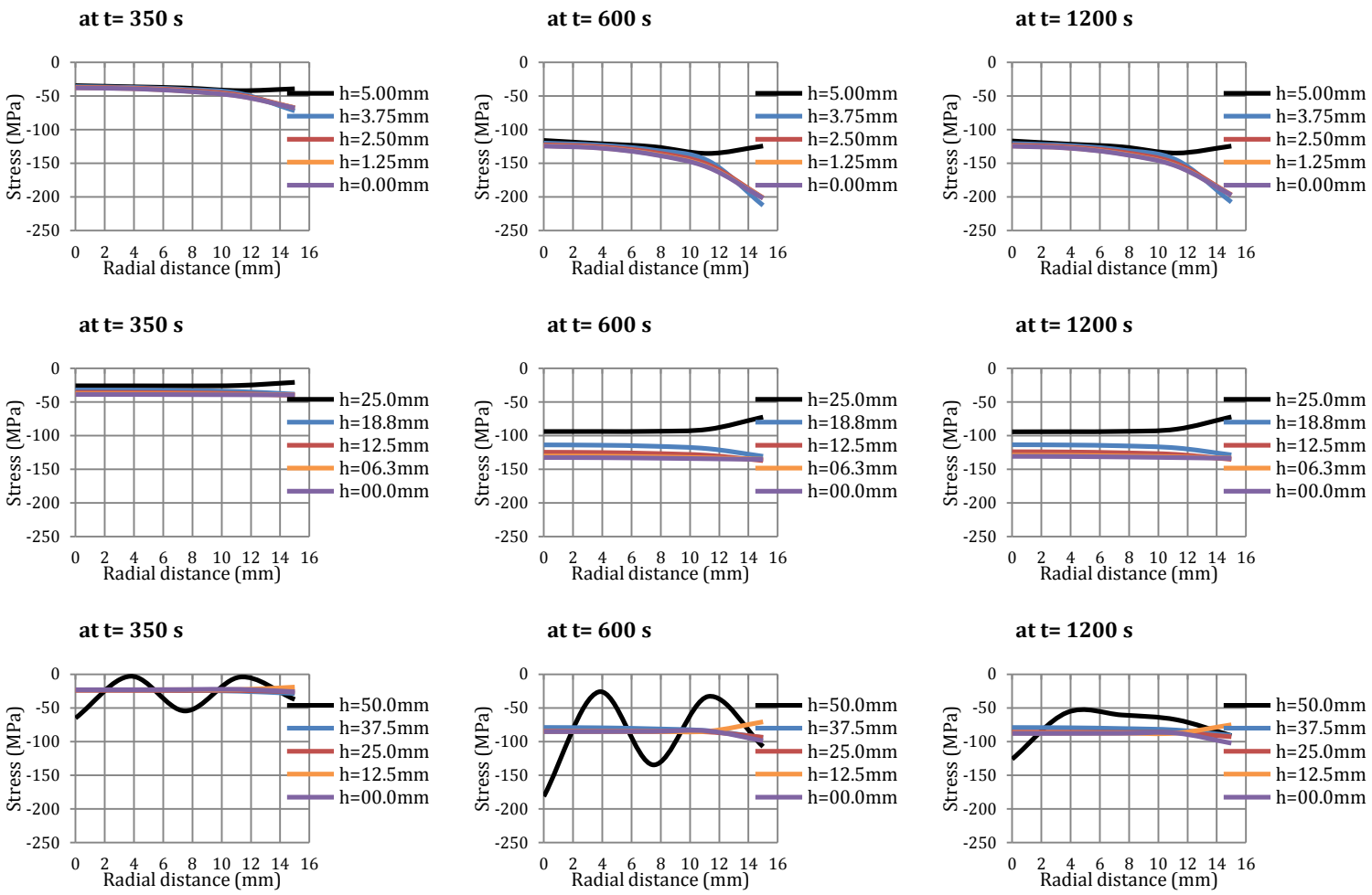

Figure 69: Radius-wise axial stress distribution at different axial positions for different sample thicknesses: row1) height=10mm, row 2) height=50mm, & row 3) height=100mm

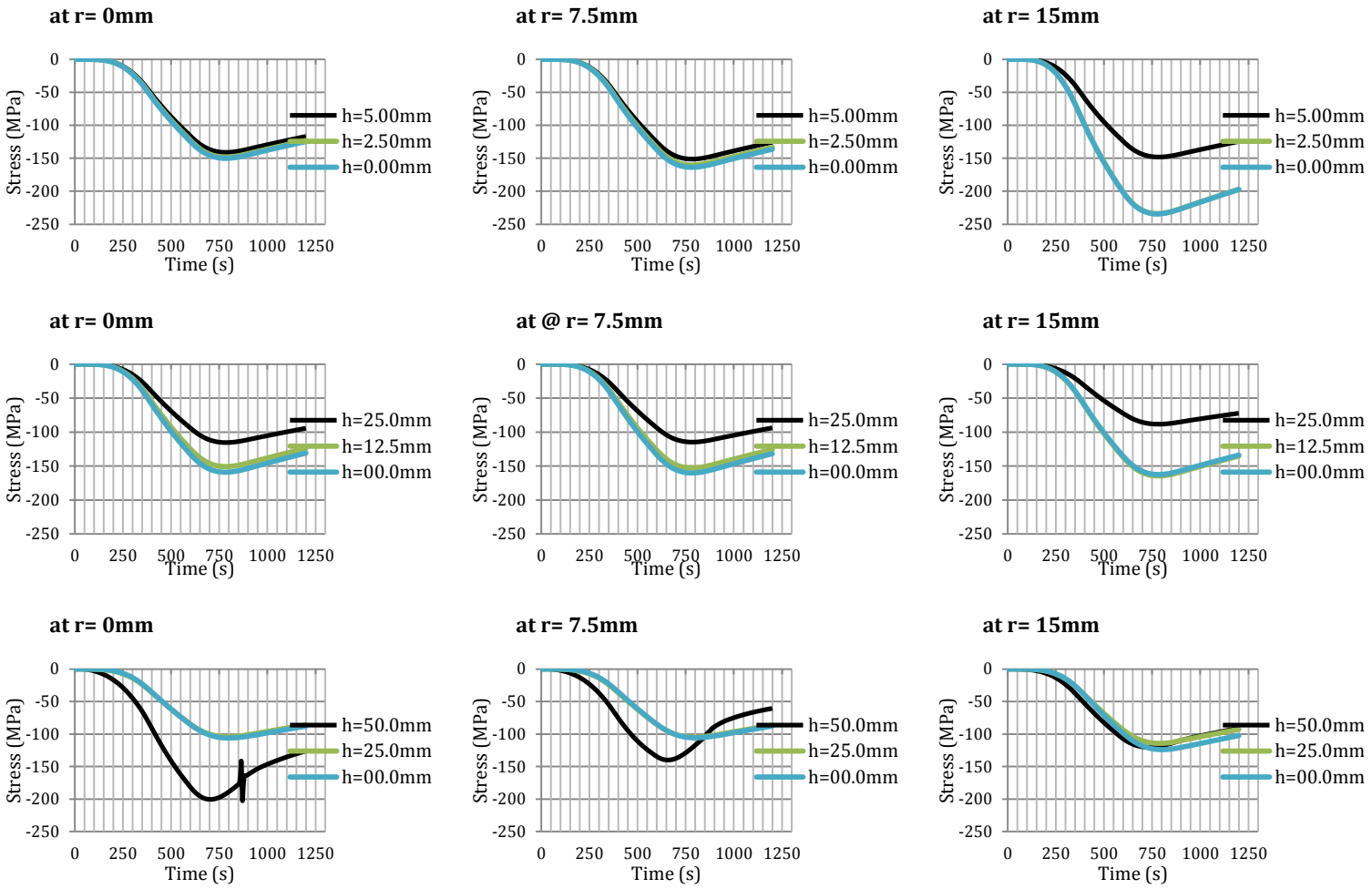

Figure 70: Axial stress evolution at different axial positions for different sample thicknesses: row1) height=10mm, row 2) height=50mm, & row 3) height=100mm

Radial stress distribution

From Figure 71, it is found that, like axial stresses, the radial stress also has compressive nature. It is because of two reasons: 1) the application of compressive load (pressure) and 2) the restriction in thermal expansion. The maximum radial stress is found in the 10mm sample and has the value of ~ -210MPa. Moreover, the radial stresses developed in the sample decreases with the increase in the size of the sample. Axially, the radial stresses' distribution is uniform in the smaller samples but has an increasing trend along z-axis (in either direction) in large sized samples. In addition, the stresses in all the "*rz*" planes are almost same in the central region but have differences near the top and bottom surfaces of the samples. This behavior is more obvious in larger samples. In radial direction, the radial stresses are uniform in the central region but near the sample-die boundary, they have a decreasing trend in the 10mm sample, almost uniform in 50mm sample and increasing trend in 100mm sample. The maximum stress is found in the top and bottom surfaces of the sample. In these top and bottom surfaces, in 100mm sample, the radial stress is not uniform and varies along the radius. From the above discussion, it can be inferred that the radial stress is mostly uniform in the central regions of the samples while it varies in the regions near to the edges. Furthermore, like the evolution of axial stresses, radial stresses also increase up to a certain maximum value and then reduce slightly leaving behind some residual stresses (see Figure 73). The quantity of these residual stresses is directly proportional to the maximum stress level achieved during the cycle.

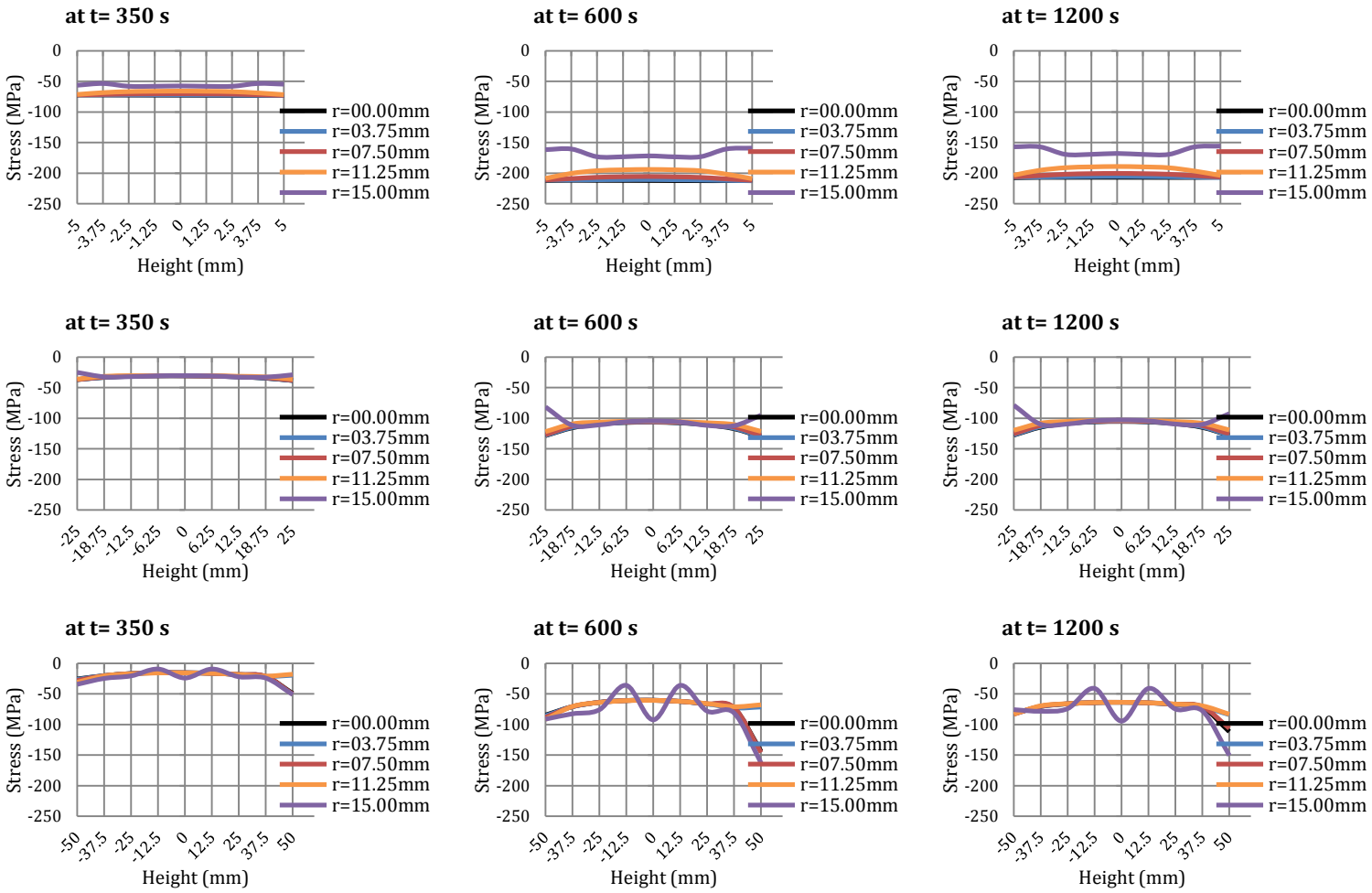

Figure 71: Height-wise radial stress distribution at different radial positions for different sample thicknesses: row1) height=10mm, row 2) height=50mm, & row 3) height=100mm

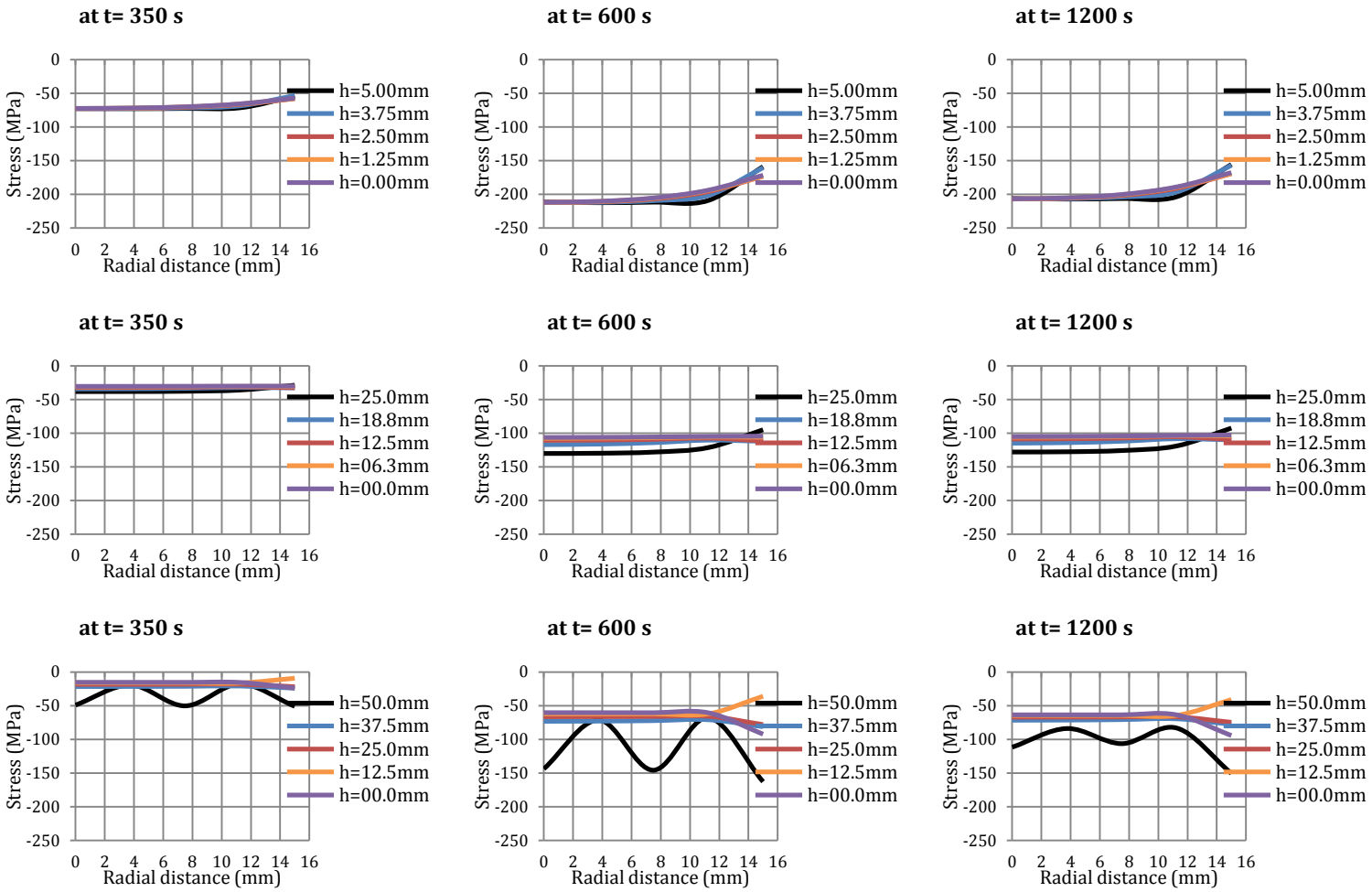

Figure 72: Radius-wise radial stress distribution at different axial positions for different sample thicknesses: row1) height=10mm, row 2) height=50mm, & row 3) height=100mm

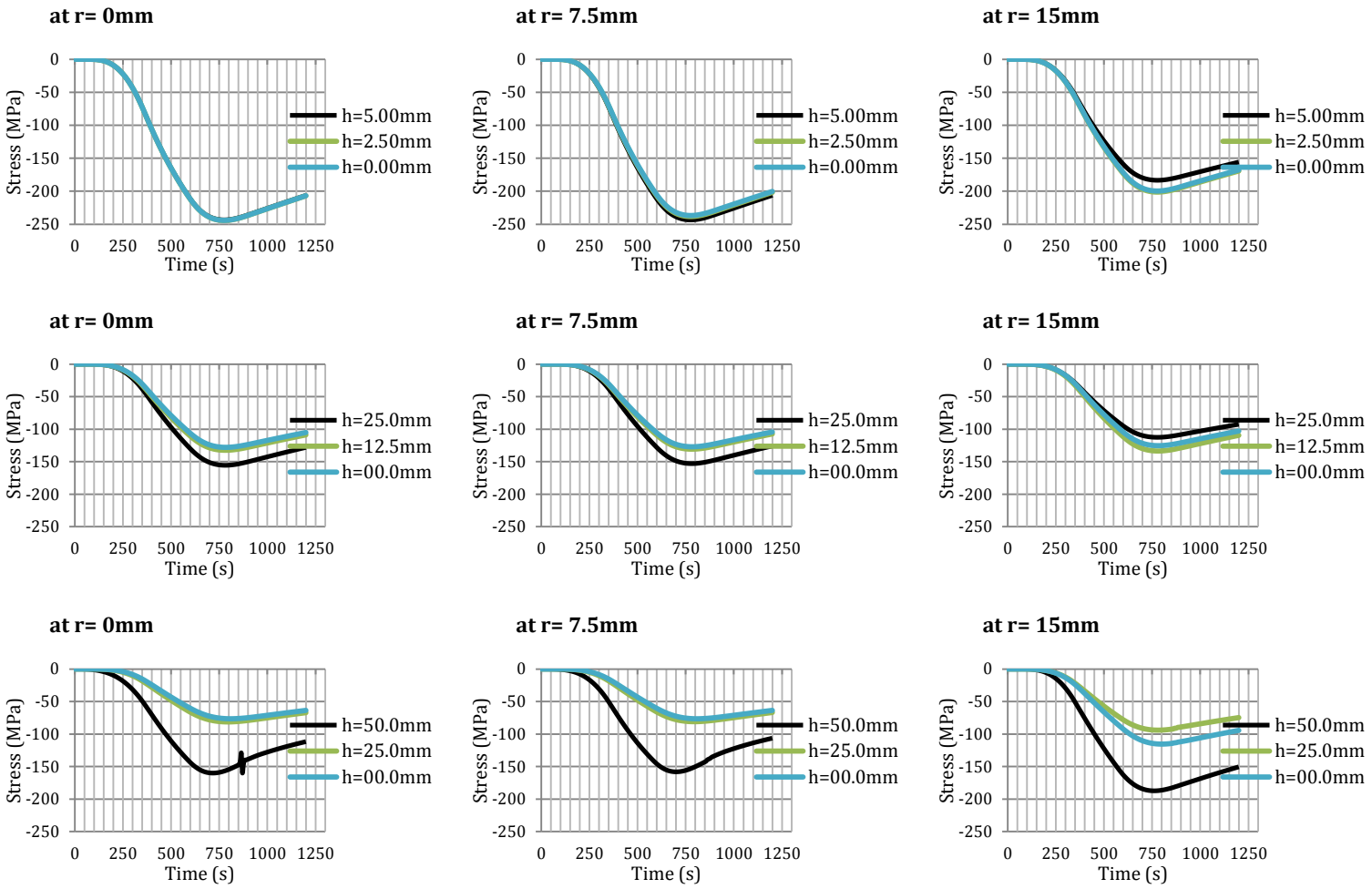

Figure 73: Radial stress evolution at different axial positions for different sample thicknesses: row1) height=10mm, row 2) height=50mm, & row 3) height=100mm

Shear stress distribution

From Figure 74, it is noticed that the shear stresses are zero in the axial directions in the axis of symmetry but in other planes they do exist with its maximum value in the plane at maximum radial position. So at the maximum radial positions, the inhomogeneity in shear stresses is maximum. Moreover, the shear stress along the height of the sample at the maximum radial position has wavering nature which is more obvious in the larger samples. The stresses developed in the samples reduce with increase in the sample thickness: the maximum shear stress is found in the 10mm sample having its value of ~100MPa. Along the radius, from Figure 75, it is observed that the shear stress is zero in the central "$r\theta$" plane while it exists in other planes with increasing trend. The maximum shear stress is found in the top and bottom surface of the sample. Moreover, maximum variations are noticed in the maximum radial positions. In addition, the shear stresses also evolve in the same manner as that of the axial and radial stresses i.e. they reach up to a maximum value and then decline slightly thereby leaving some residual stresses in the sample (see Figure 76).

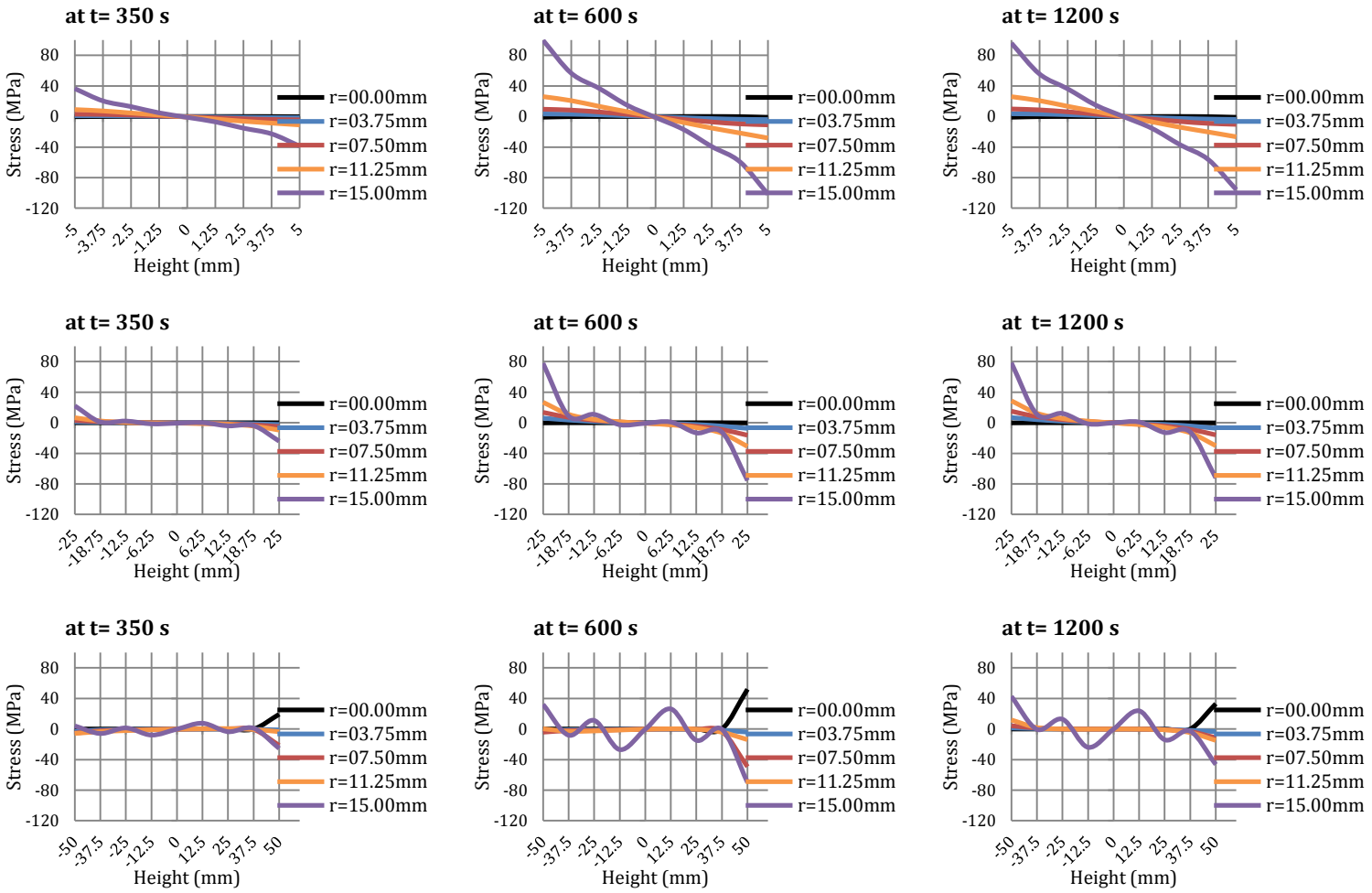

Figure 74: Height-wise shear stress distribution at different radial positions for different sample thicknesses: row1) height=10mm, row 2) height=50mm, & row 3) height=100mm

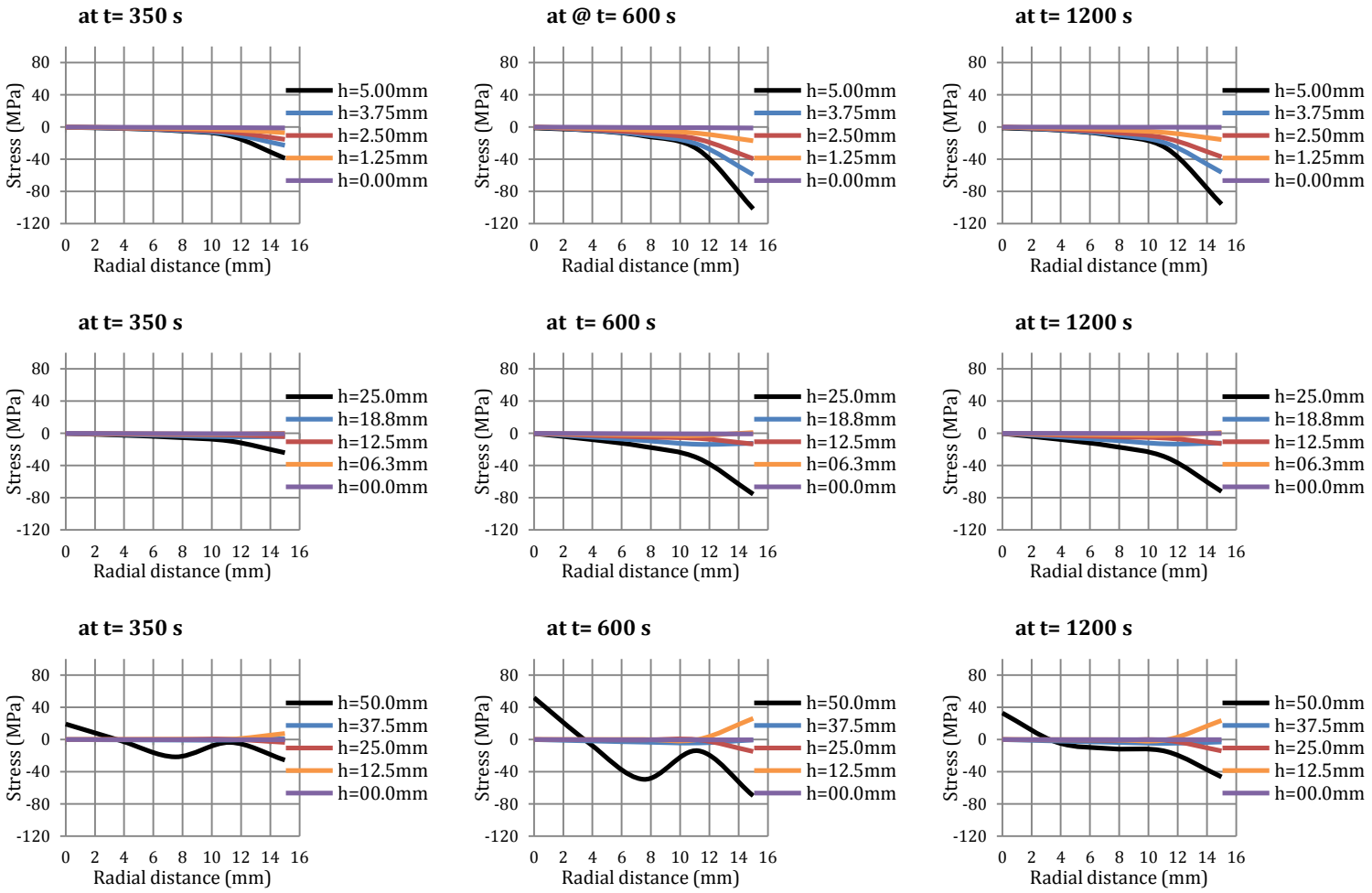

Figure 75: Radius-wise shear stress distribution at different axial positions for different sample thicknesses: row1) height=10mm, row 2) height=50mm, & row 3) height=100mm

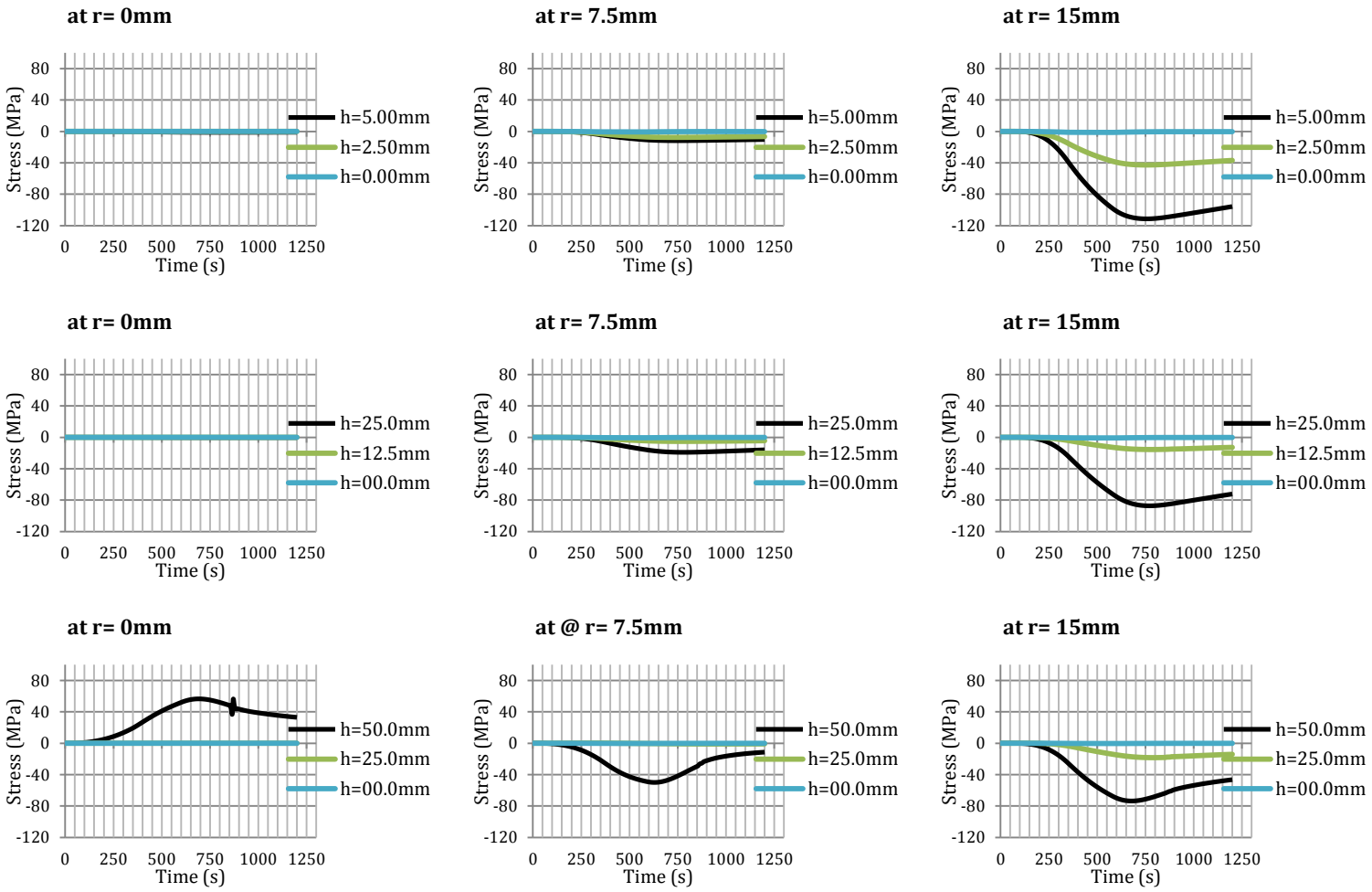

Figure 76: Shear stress evolution at different axial positions for different sample thicknesses: row1) height=10mm, row 2) height=50mm, & row 3) height=100mm

5.3.3 CASE-II

Sample heights: 10, 50, & 100 mm

Sample diameter: 30 mm

Sample Material: Alumina (electrically insulator)

Current density distribution

In this case, from Figure 77, the current density is almost zero in all the samples because of the almost zero electrical conductivity of the sample material (alumina).

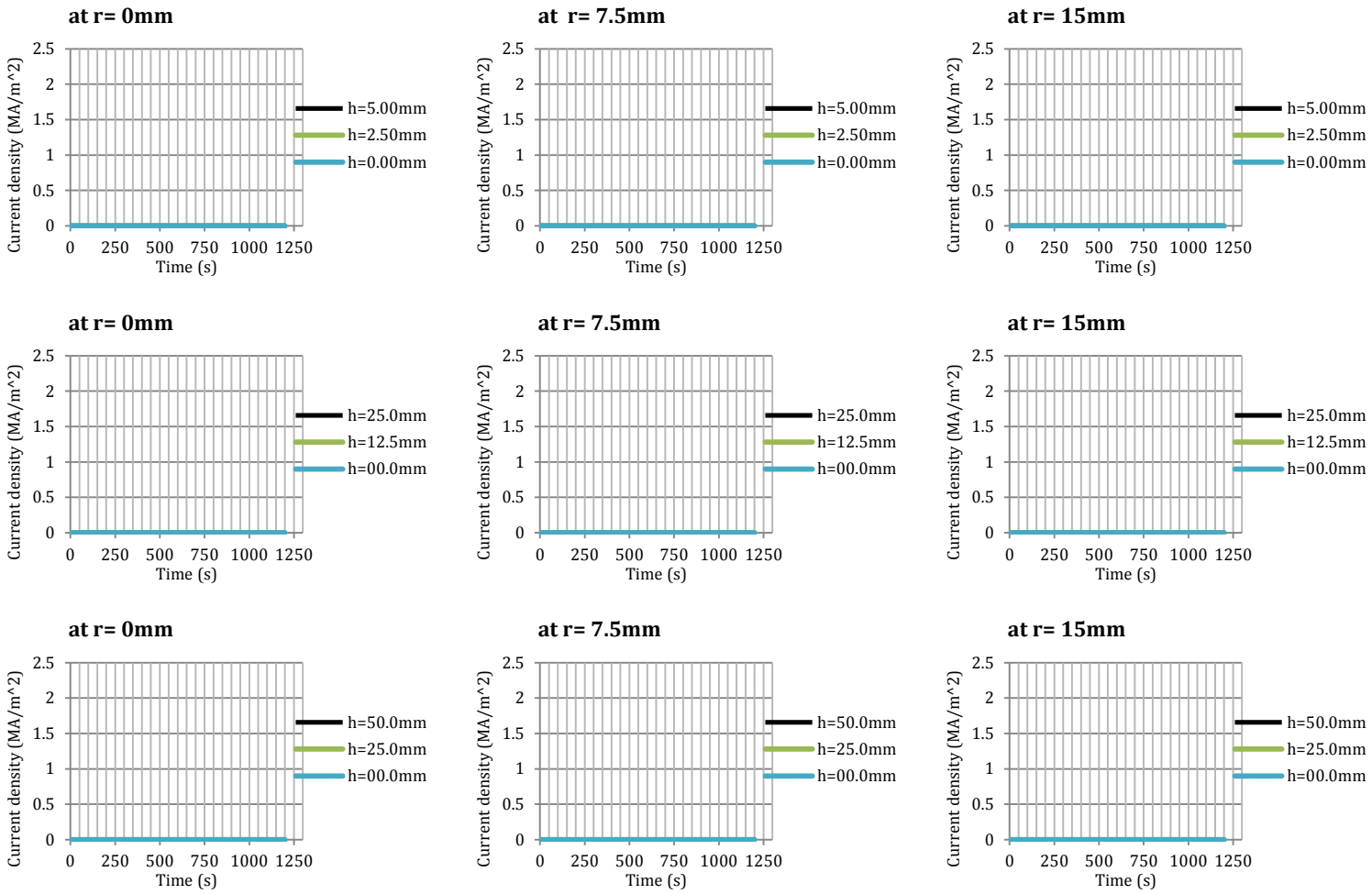

Figure 77: Current density evolution at different axial positions for different sample thicknesses: row1) height=10mm, row 2) height=50mm, & row 3) height=100mm

Temperature distribution

In this case, the temperature rise in the sample is only because of the heat conduction from the die and the punches as there is no heat source in the sample because of absence of current flow in it. This phenomenon is also supported by Figure 78, where it is observed that the temperature at the boundaries of the sample is higher than the temperature of the central region. The maximum temperature is found in the top and bottom surfaces of the sample and is symmetric about the central "*rθ*" plane. The maximum temperature difference between the top surface and the center of the sample is increasing with the increase in the size of the sample – it is ~ 3K in 10mm sample while ~ 27K in 100mm sample. In addition, it is also observed that in cooling cycle the center of the sample has the highest temperature. From Figure 79, it is noticed that the temperature is increasing in the radial direction in all the planes. But there is an exception in the larger samples in the top surface of the sample where the temperature has decreasing trend along the radius. In cooling cycle, the higher temperature is found in the central region of the sample. With respect to time, the temperature in the sample first increases up to a maximum value and then starts to reduce. At the peak value, almost all the regions of the sample reach to the same temperature and after that it is almost uniform throughout.

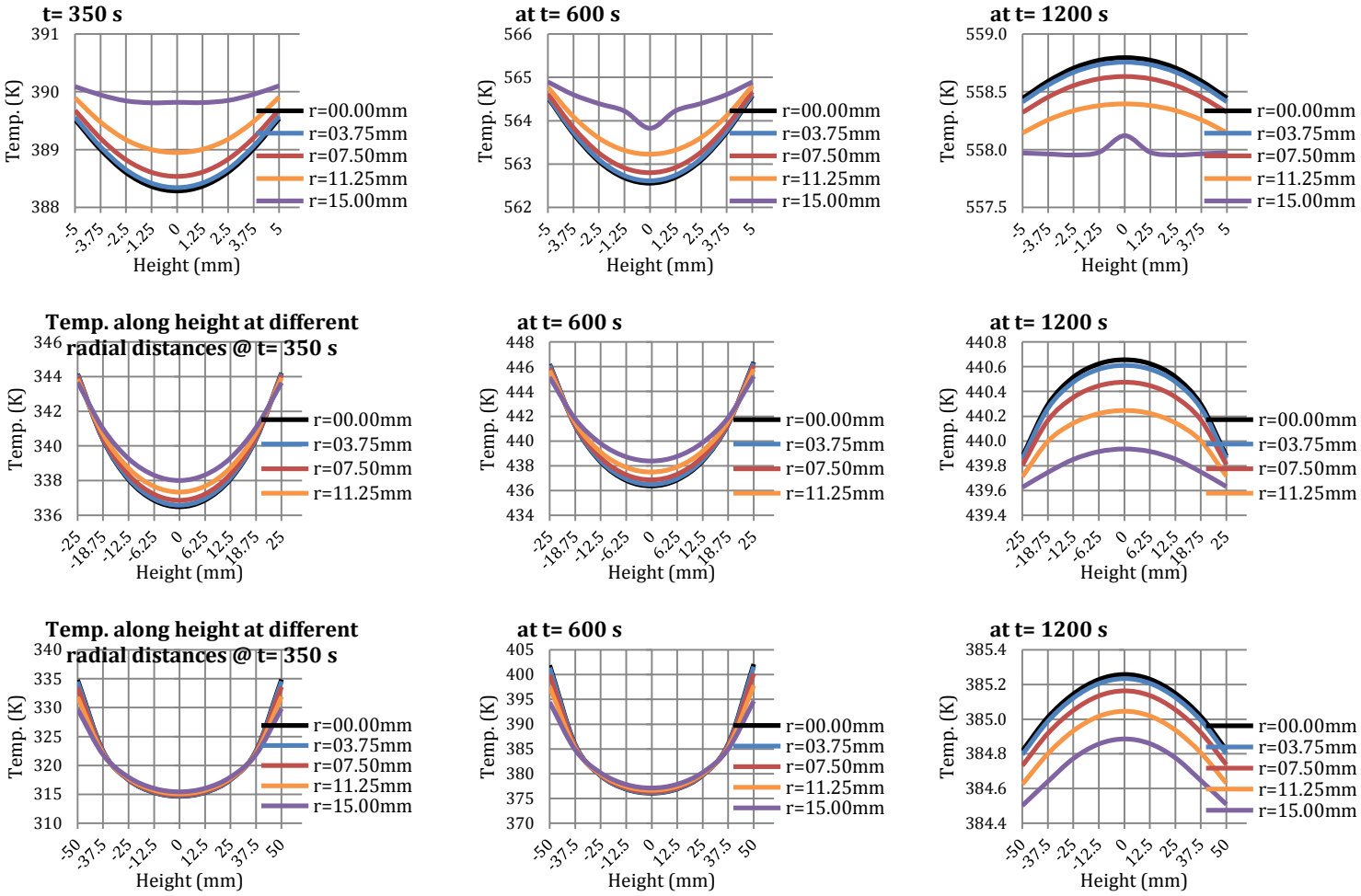

Figure 78: Height-wise temperature distribution at different radial positions for different sample thicknesses: row1) height=10mm, row 2) height=50mm, & row 3) height=100mm

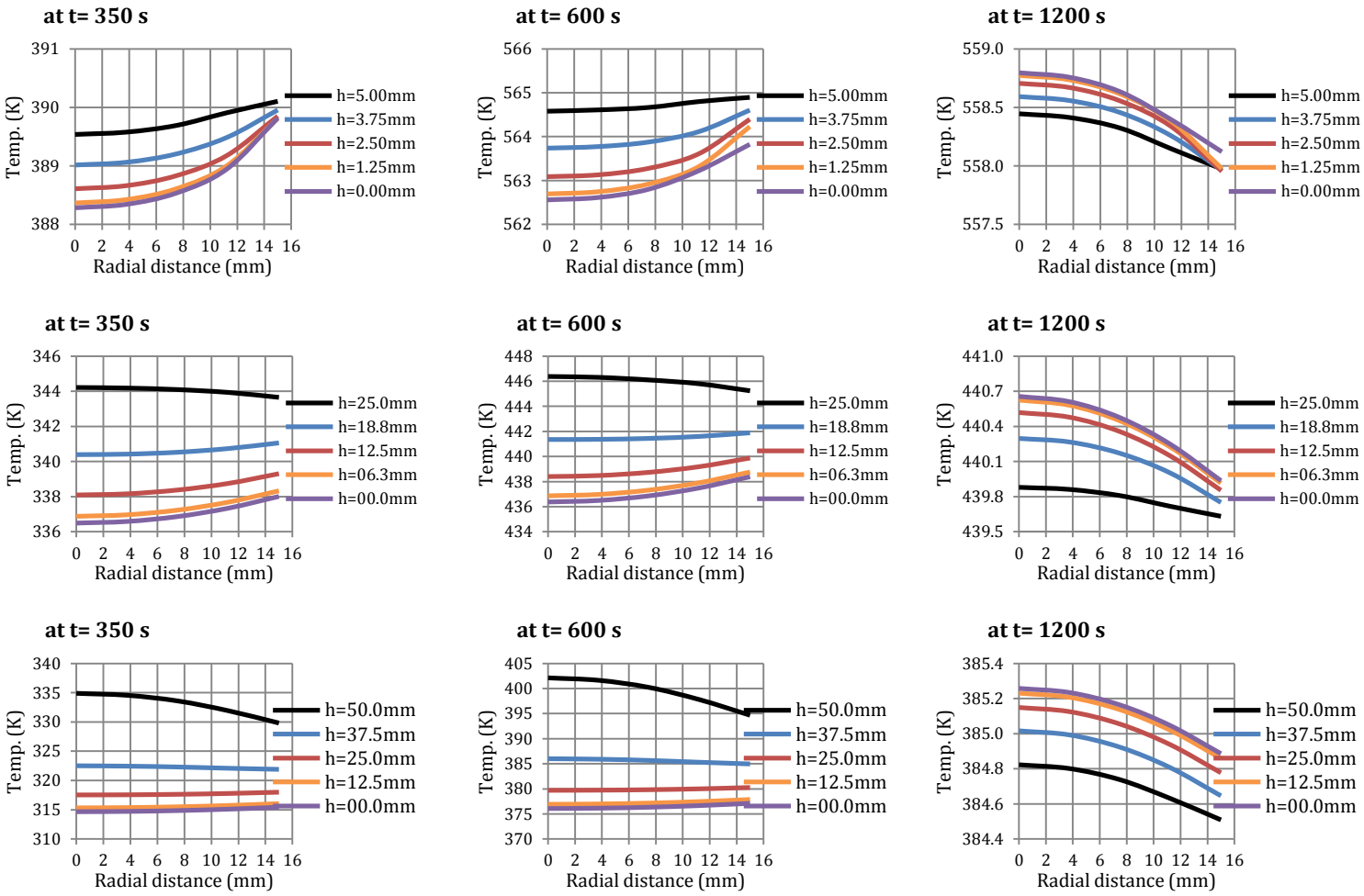

Figure 79: Radius-wise temperature distribution at different axial positions for different sample thicknesses: row1) height=10mm, row 2) height=50mm, & row 3) height=100mm

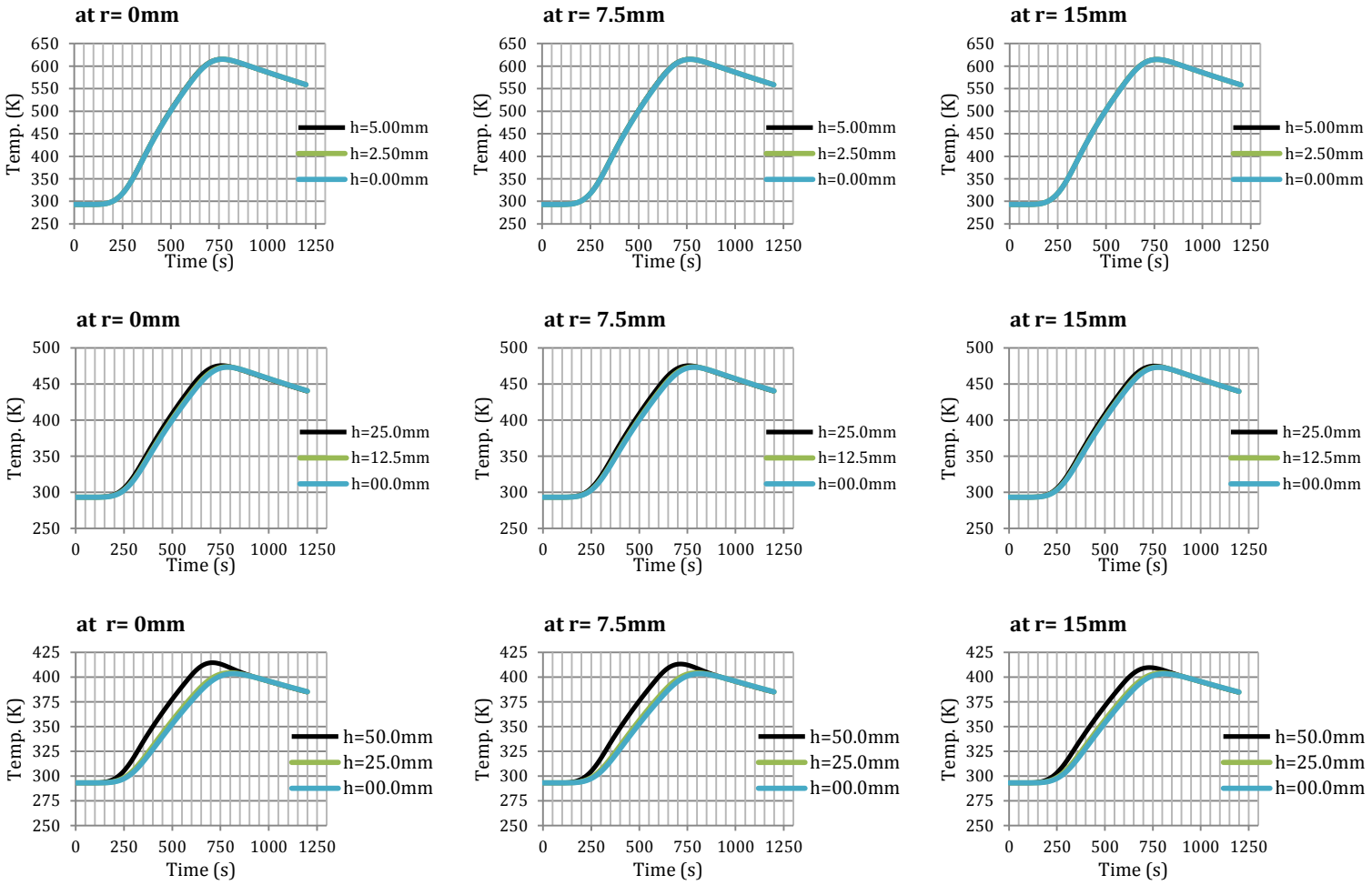

Figure 80: Temperature evolution at different axial positions for different sample thicknesses: row1) height=10mm, row 2) height=50mm, & row 3) height=100mm

Von-Mises stress distribution

From Figure 81, it is observed that von-Mises stress developed in the samples varies along the axial direction with the maximum variation at the top and bottom surfaces of the sample. In other words, von-Mises stress is relatively uniform in the central region (axially) of the sample. The maximum von-Mises stress is found in the layer at the sample-die boundary and its value is decreasing with the increase in the size of the sample – ~95GPa in 10mm sample and ~10GPa in 100mm sample. Again, it is because of the same reason that as the sample volume increases, more energy is needed to achieve the same deformation. Moreover, as these values are higher than the yield stress of alumin (15.4GPa), plastic strains will be present in the smaller samples and hence the elastic behavior assumption is not enough and it is needed to include the plastic behavior of the material in the model. Furthermore, the von-Mises stress is found to be almost symmetric about the center of the sample in axial direction. In addition, from Figure 82, it is noticed that there exists variation in von-Mises stress along the radius and the maximum value is found at r=15mm and quarter from top and bottom surface of the sample. Moreover, as the size of the sample increases, the stresses in the sample become more and more uniform. From this discussion, it is inferred that, in the whole sample, the maximum von-Mises stress is developed at the maximum radial and quarter from the top and bottom surface of the sample and hence they are the critical regions as far as plasticity is concerned. Also, from Figure 83, it is observed that the von-Mises stress increases with time till certain maximum value and then starts to decline slightly in all the regions of the sample.

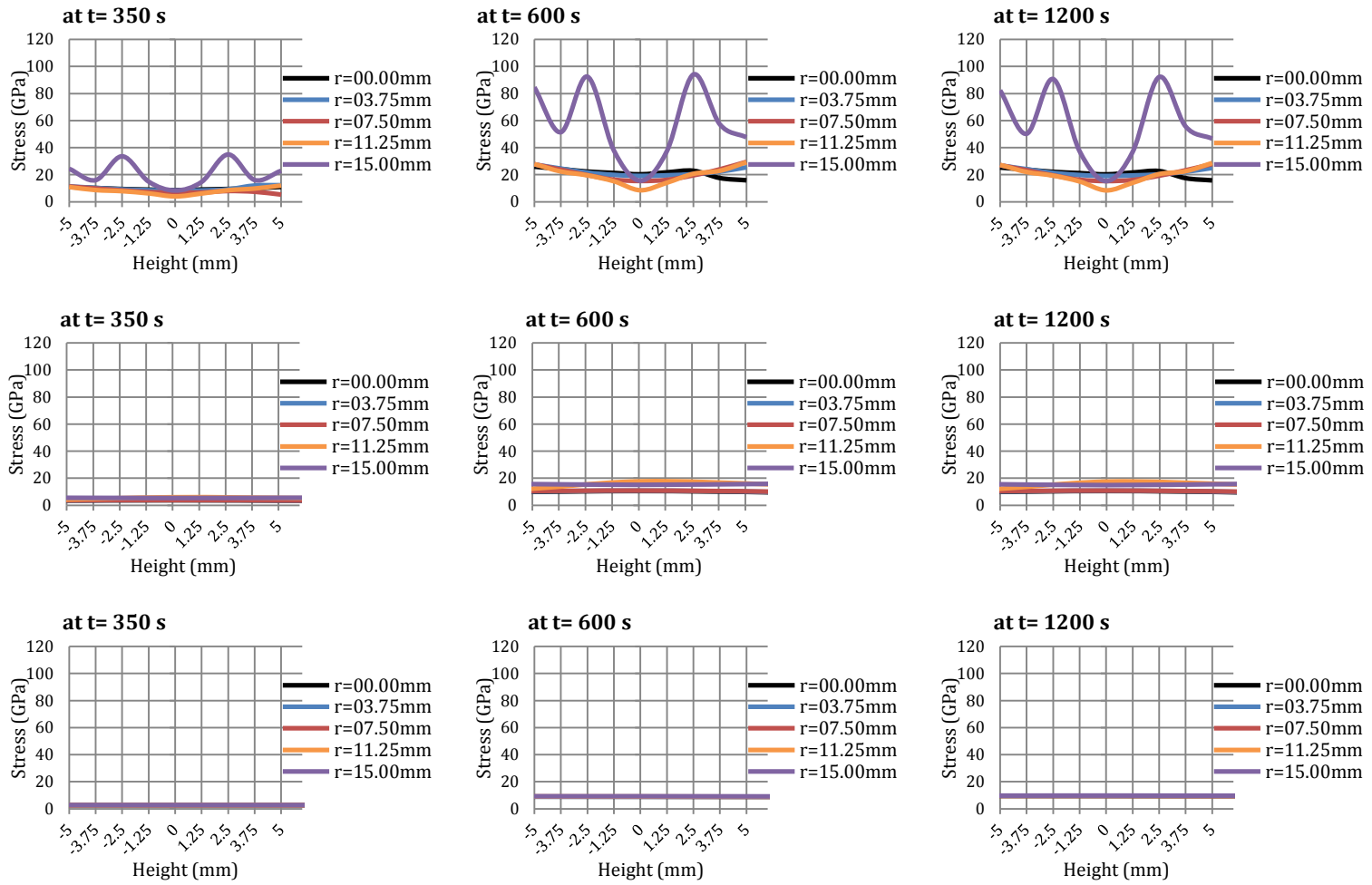

Figure 81: Height-wise von-Mises stress distribution at different radial positions for different sample thicknesses: row1) height=10mm, row 2) height=50mm, & row 3) height=100mm

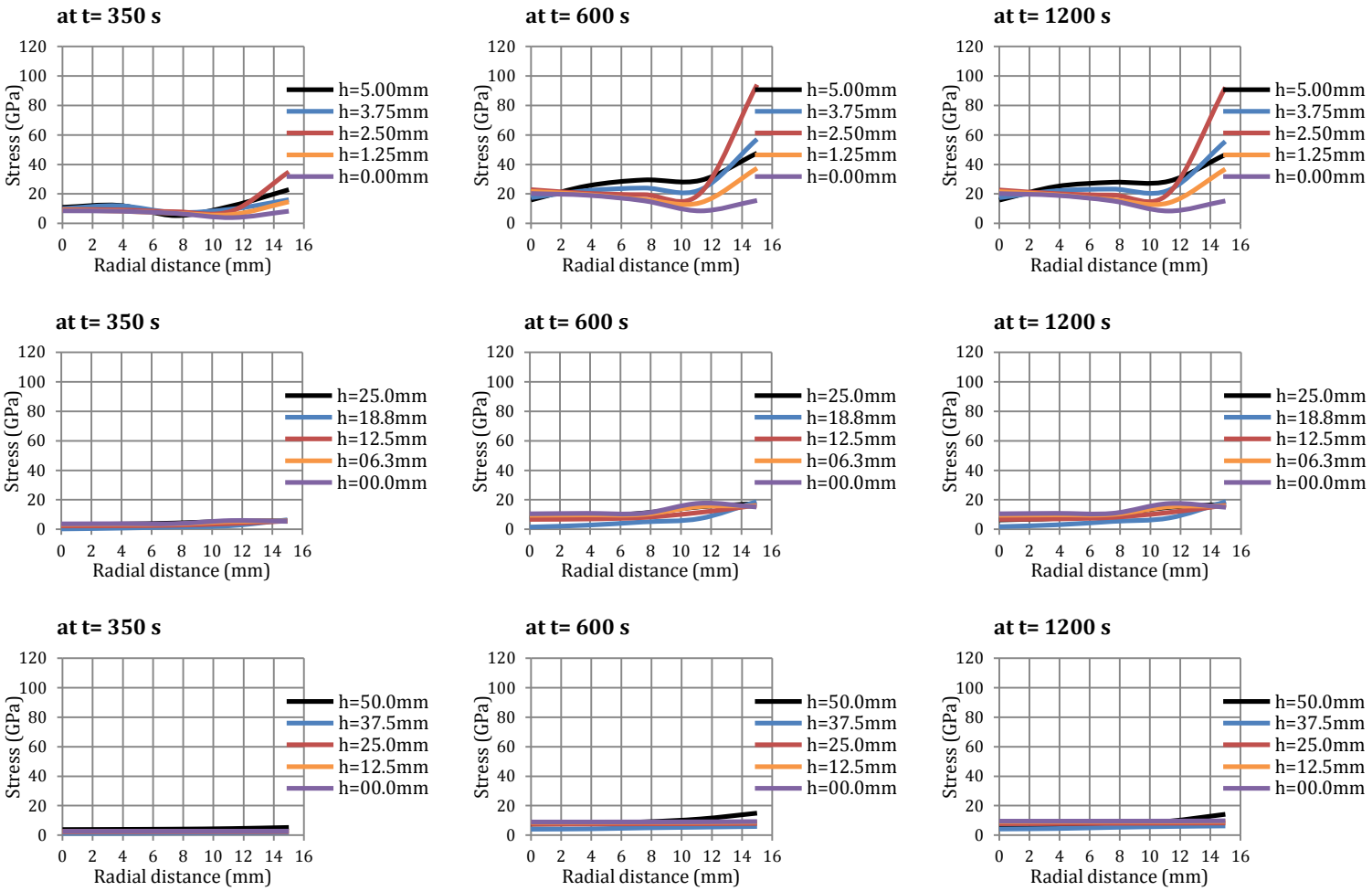

Figure 82: Radius-wise von-Mises stress distribution at different axial positions for different sample thicknesses: row1) height=10mm, row 2) height=50mm, & row 3) height=100mm

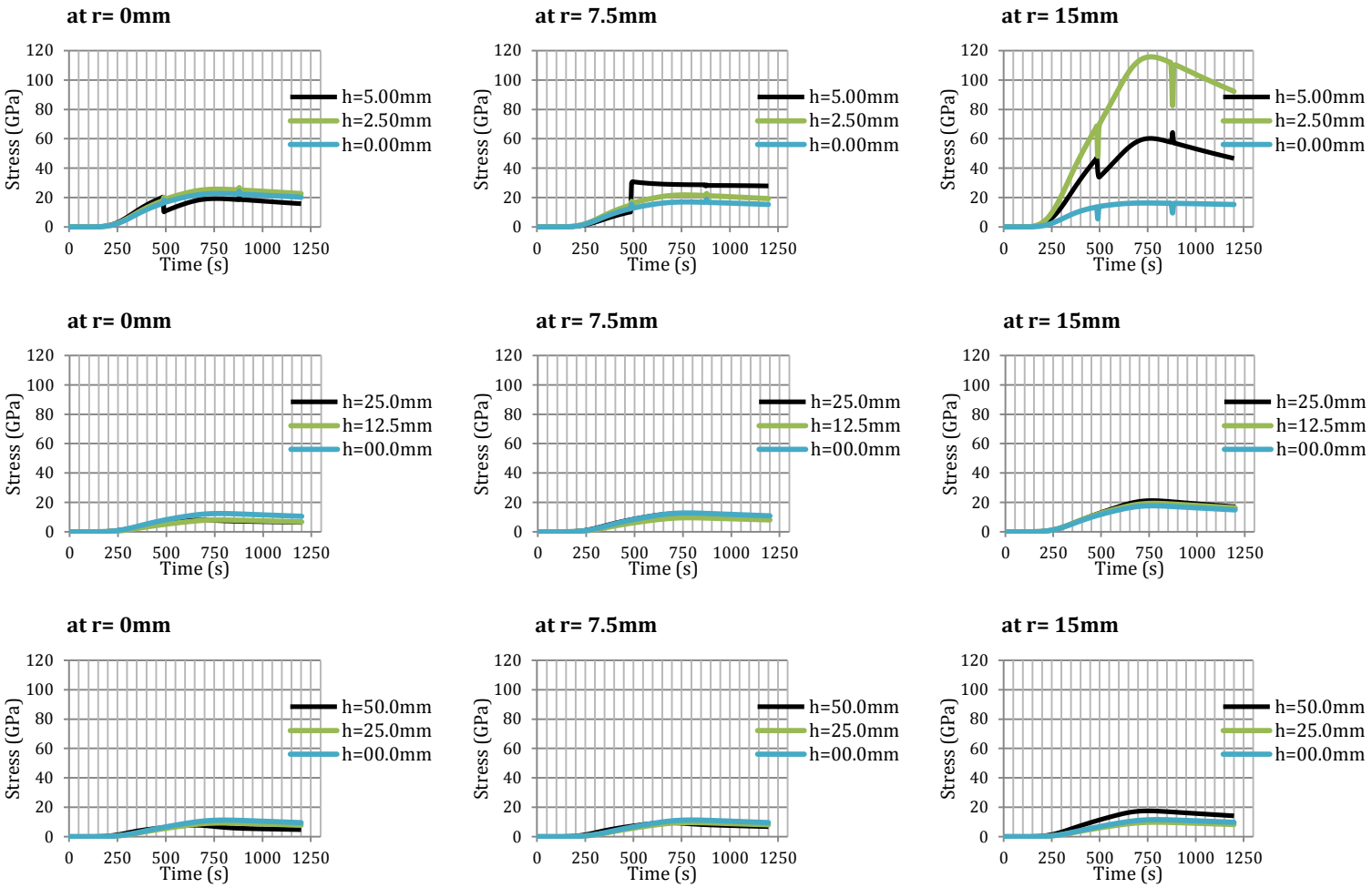

Figure 83: Von-Mises stress evolution at different axial positions for different sample thicknesses: row1) height=10mm, row 2) height=50mm, & row 3) height=100mm

Axial stress distribution

From Figure 84, it is noticed that although the axial stresses developed in the sample are generally compressive in nature (because of the applied pressure), there are some regions near the sample-die boundary where the nature of axial stress is tensile. This abnormal behavior is because of the slip and stick mechanism due to friction. In the axial direction, these stresses are non-symmetric. Moreover, the stresses in the smaller samples are larger than the stresses developed in the larger samples. The maximum axial stress developed is ~ -35GPa in the 10mm sample. In radial directions, from Figure 85, the stresses are overall increasing along the radius in the smaller samples while it is almost uniform in the larger samples. Moreover, the stresses developed in different horizontal planes are almost same in the central regions of the sample while they have differences near the sample-die boundary. From these discussions, it is deduced that, in the central regions of the samples, the stresses are almost homogenous while the inhomogeneity is mostly found at all the edges/boundaries of the samples. Furthermore, the axial stresses also evolve in the same manner as that of the von-Mises stresses i.e. increase to a maximum value and then reduce slightly. In addition, some stresses remain in the sample at the end of the process.

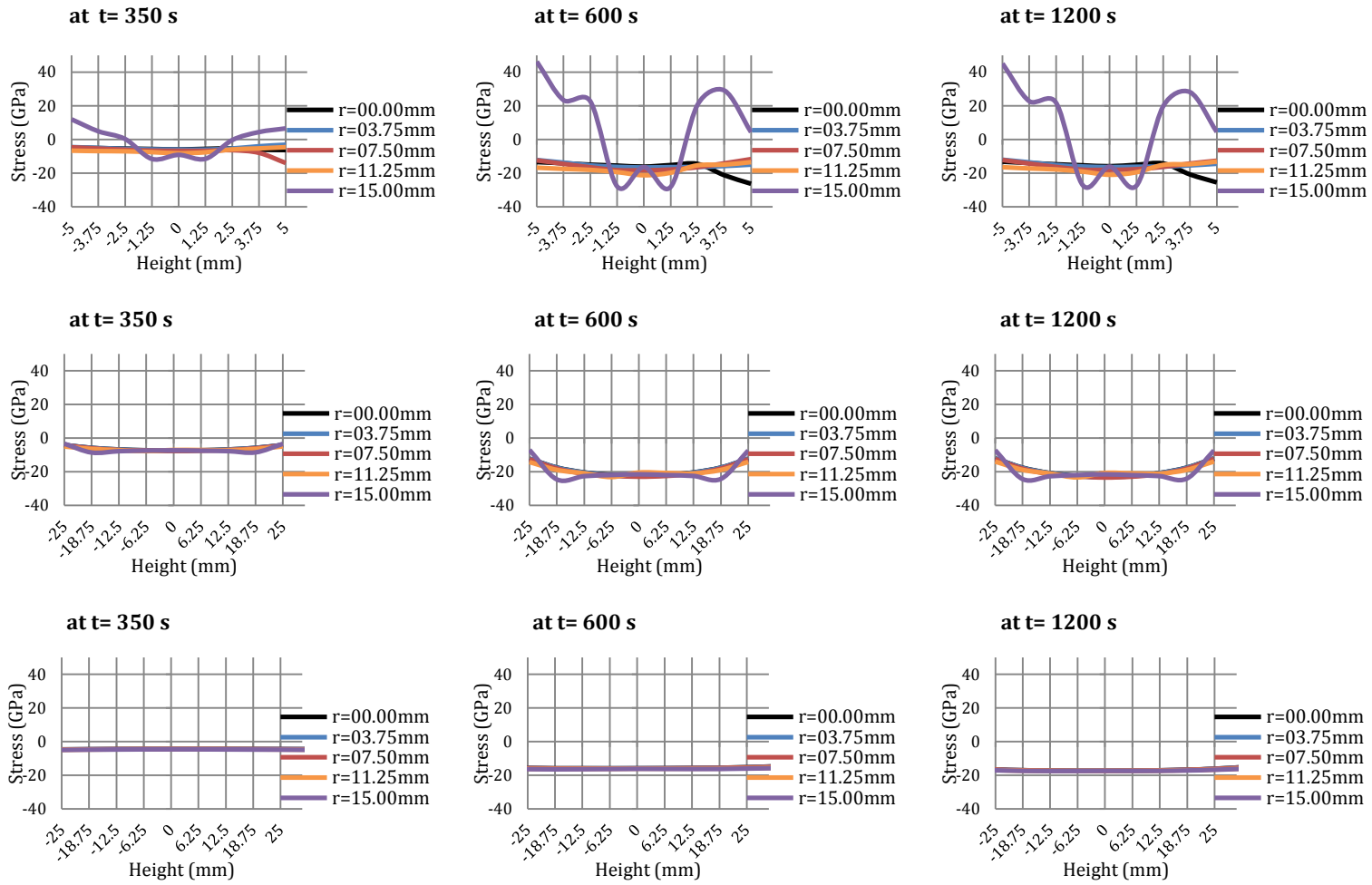

Figure 84: Height-wise axial stress distribution at different radial positions for different sample thicknesses: row1) height=10mm, row 2) height=50mm, & row 3) height=100mm

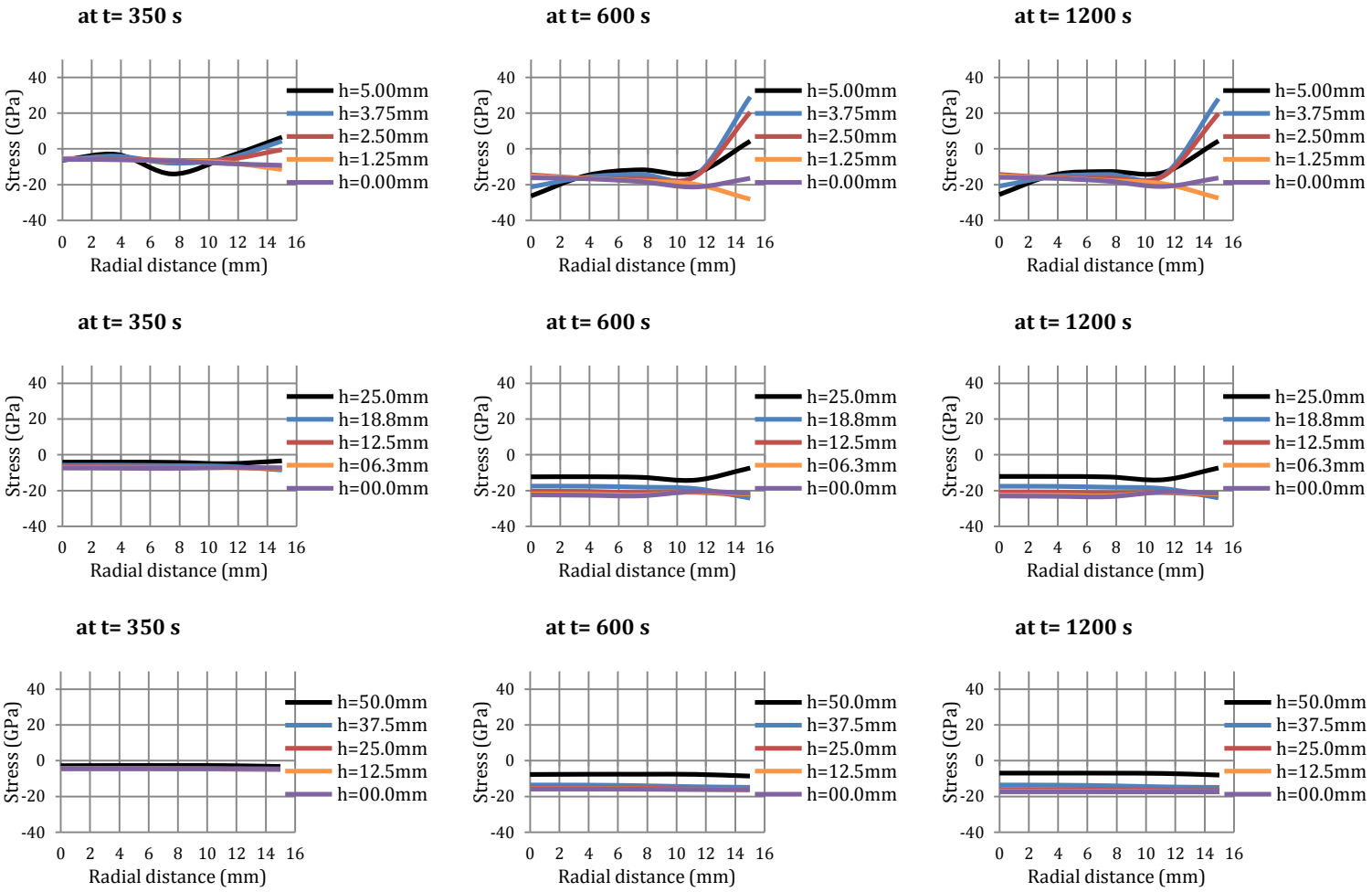

Figure 85: Radius-wise axial stress distribution at different axial positions for different sample thicknesses: row1) height=10mm, row 2) height=50mm, & row 3) height=100mm

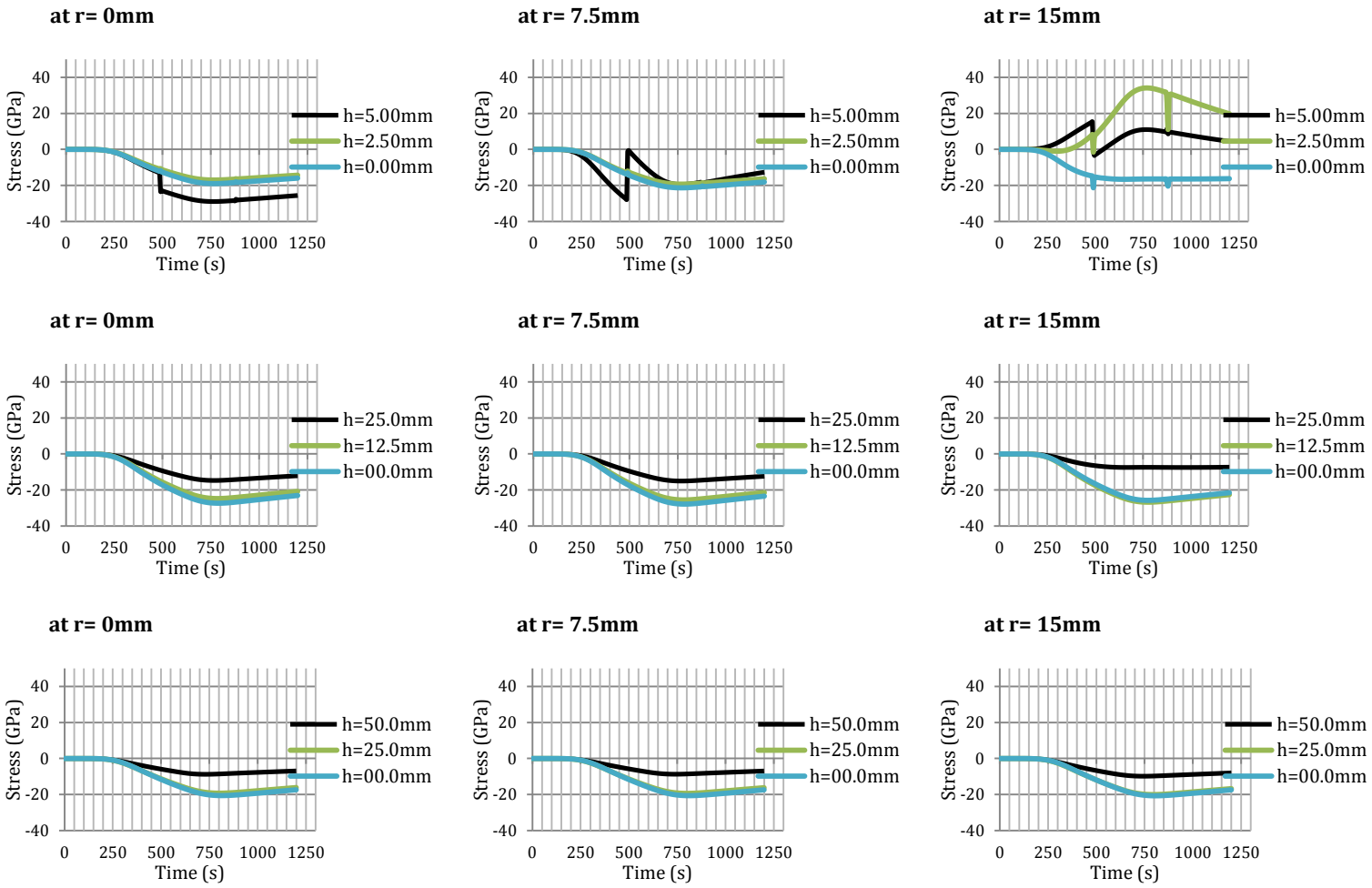

Figure 86: Axial stress evolution at different axial positions for different sample thicknesses: row1) height=10mm, row 2) height=50mm, & row 3) height=100mm

Radial stress distribution

From Figure 87, it is found that, like axial stresses, the radial stress also has compressive nature. It is because of two reasons: 1) the application of compressive load (pressure) and 2) the restriction in thermal expansion. The maximum radial stress is found in the 10mm sample and has the value of ~ -70GPa. Moreover, the radial stresses developed in the sample decreases with the increase in the size of the sample. Axially, the radial stresses' distribution is uniform in the smaller samples but has an increasing trend along z-axis (in either direction) in large sized samples. In addition, the stresses in all the "*rz*" planes are almost same in the central region but have differences near the top and bottom surfaces of the samples. This behavior is more obvious in larger samples. In radial direction (see Figure 88), the radial stresses are uniform in the central region but near the sample-die boundary, they have a decreasing trend in the 10mm sample, almost uniform in 50mm sample and increasing trend in 100mm sample. The maximum stress is found in the top and bottom surfaces of the sample. In these top and bottom surfaces, in 100mm sample, the radial stress is not uniform and varies along the radius. From the above discussion, it can be inferred that the radial stress is mostly uniform in the central regions of the samples while it varies in the regions near to the edges. Furthermore, like the evolution of axial stresses, radial stresses also increase up to a certain maximum value and then reduce slightly leaving behind some residual stresses (see Figure 89). The quantity of these residual stresses is directly proportional to the maximum stress level achieved during the cycle.

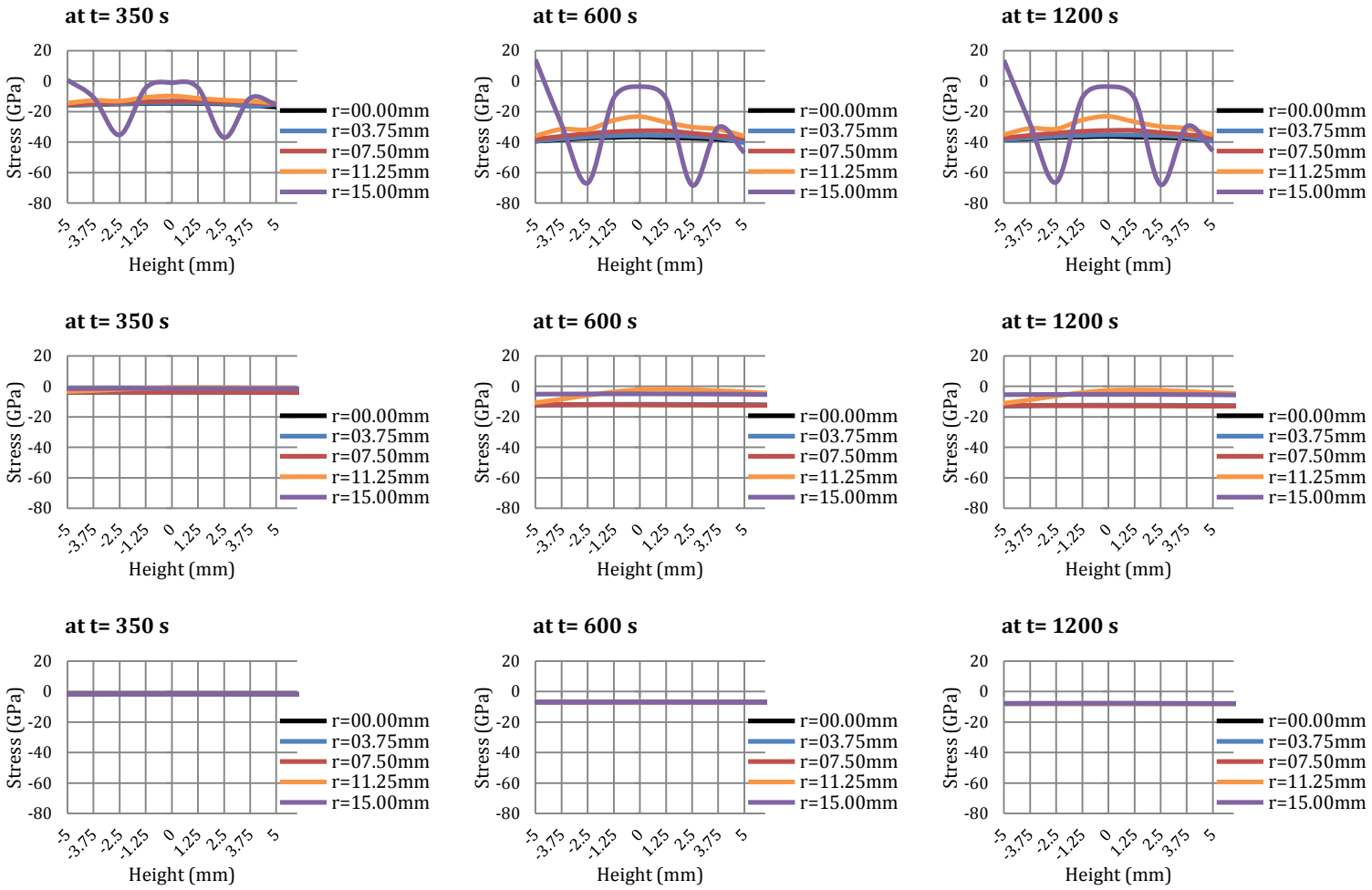

Figure 87: Height-wise radial stress distribution at different radial positions for different sample thicknesses: row1) height=10mm, row 2) height=50mm, & row 3) height=100mm

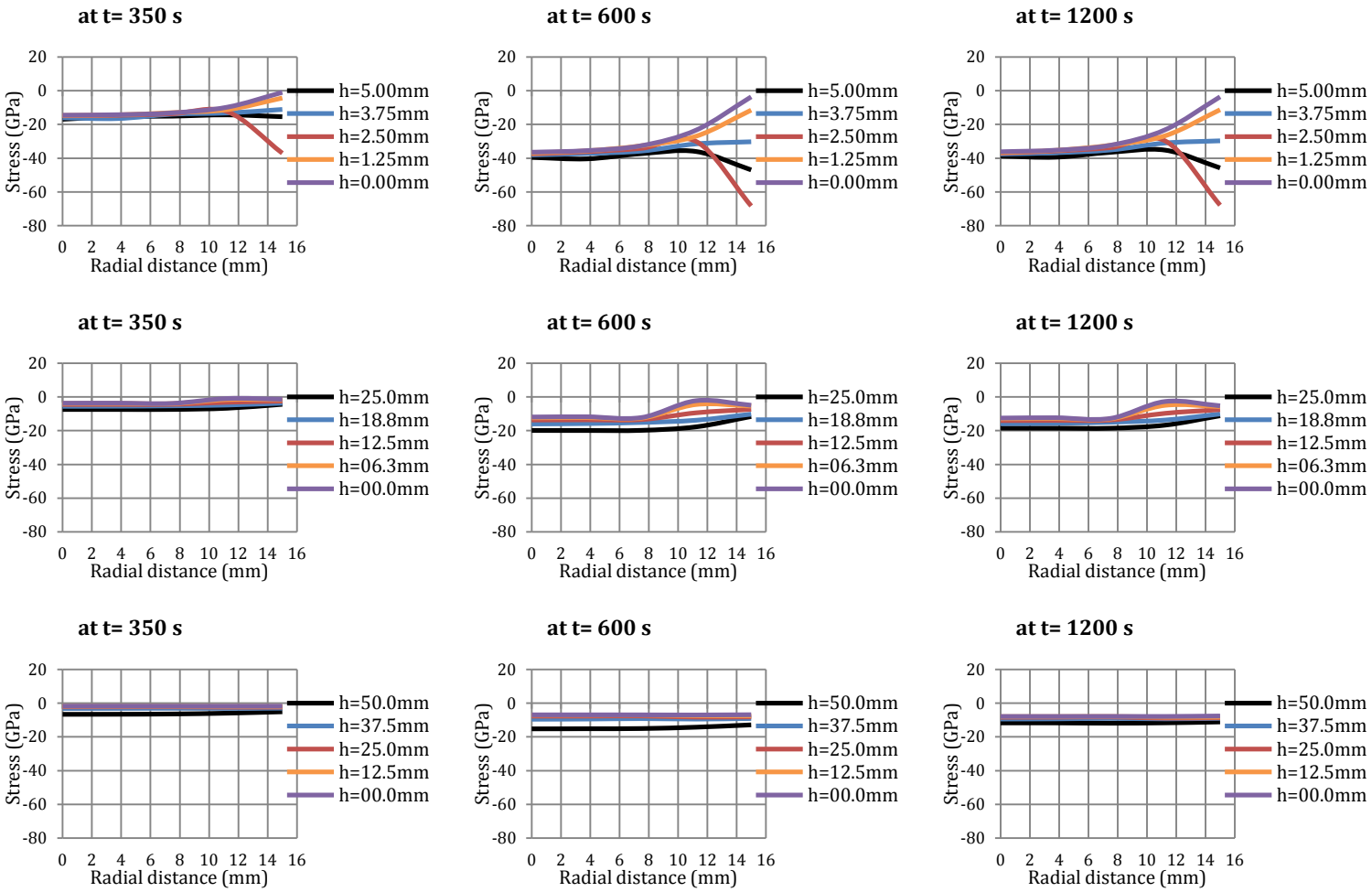

Figure 88: Radius-wise radial stress distribution at different axial positions for different sample thicknesses: row1) height=10mm, row 2) height=50mm, & row 3) height=100mm

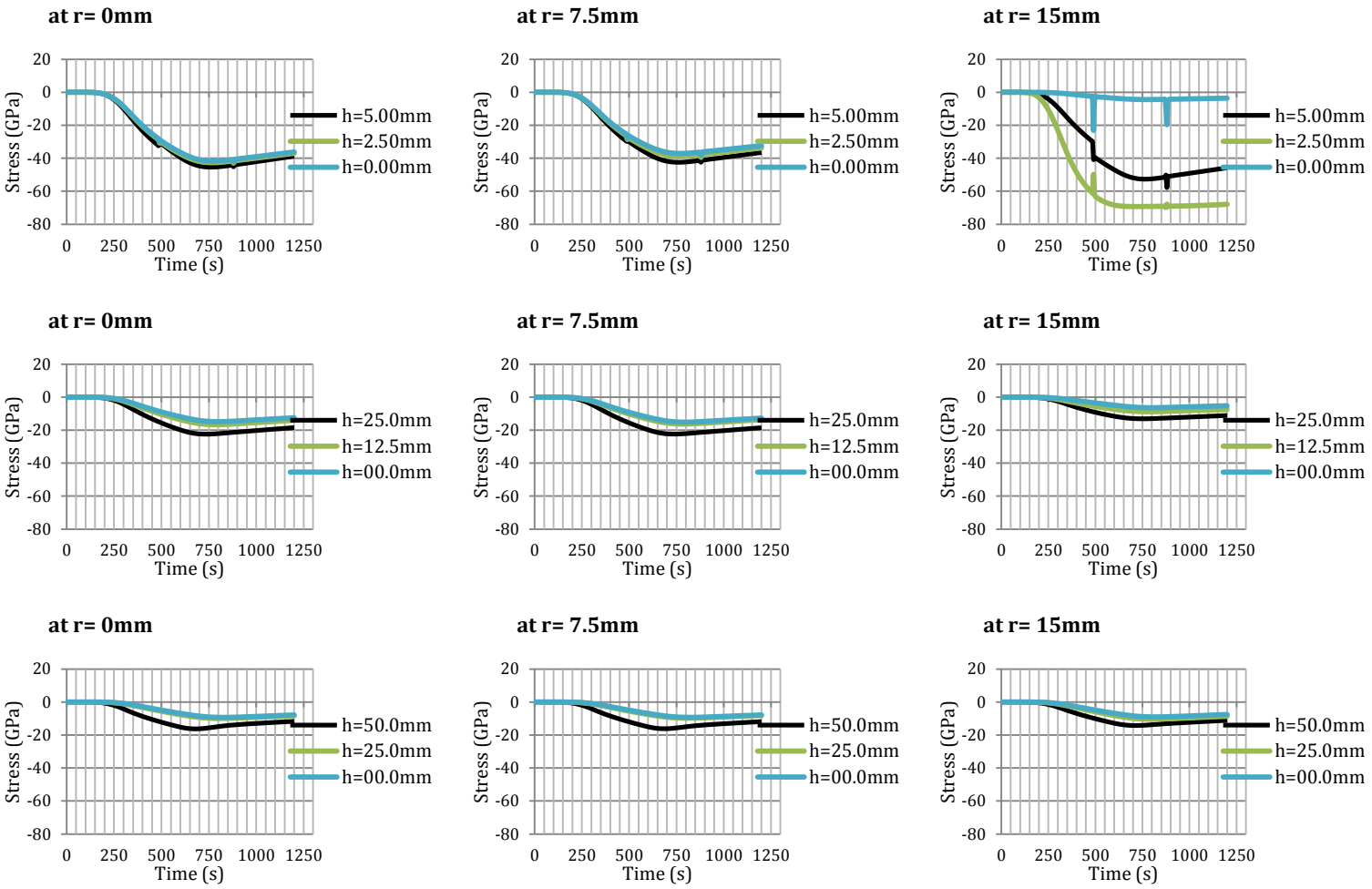

Figure 89: Radial stress evolution at different axial positions for different sample thicknesses: row1) height=10mm, row 2) height=50mm, & row 3) height=100mm

Shear stress distribution

From Figure 90, it is observed that the shear stress developed in the sample is non-symmetric along the axis of the sample. It is zero in the axis of symmetry and increases in the other planes. The maximum value exists in the sample-die boundary of the sample. At the end of the process, there are some minor residual stresses. In the radial direction, the shear stresses has increasing/decreasing trend. In the regions near to the top and bottom surfaces of the sample, the stresses are increasing while in the central regions, they have reducing trend (see Figure 91). Moreover, these stresses generally reach to a maximum value (either positive or negative), then reduce to the minimum value and at the end of the process leave behind some minor residual stresses (see Figure 92).

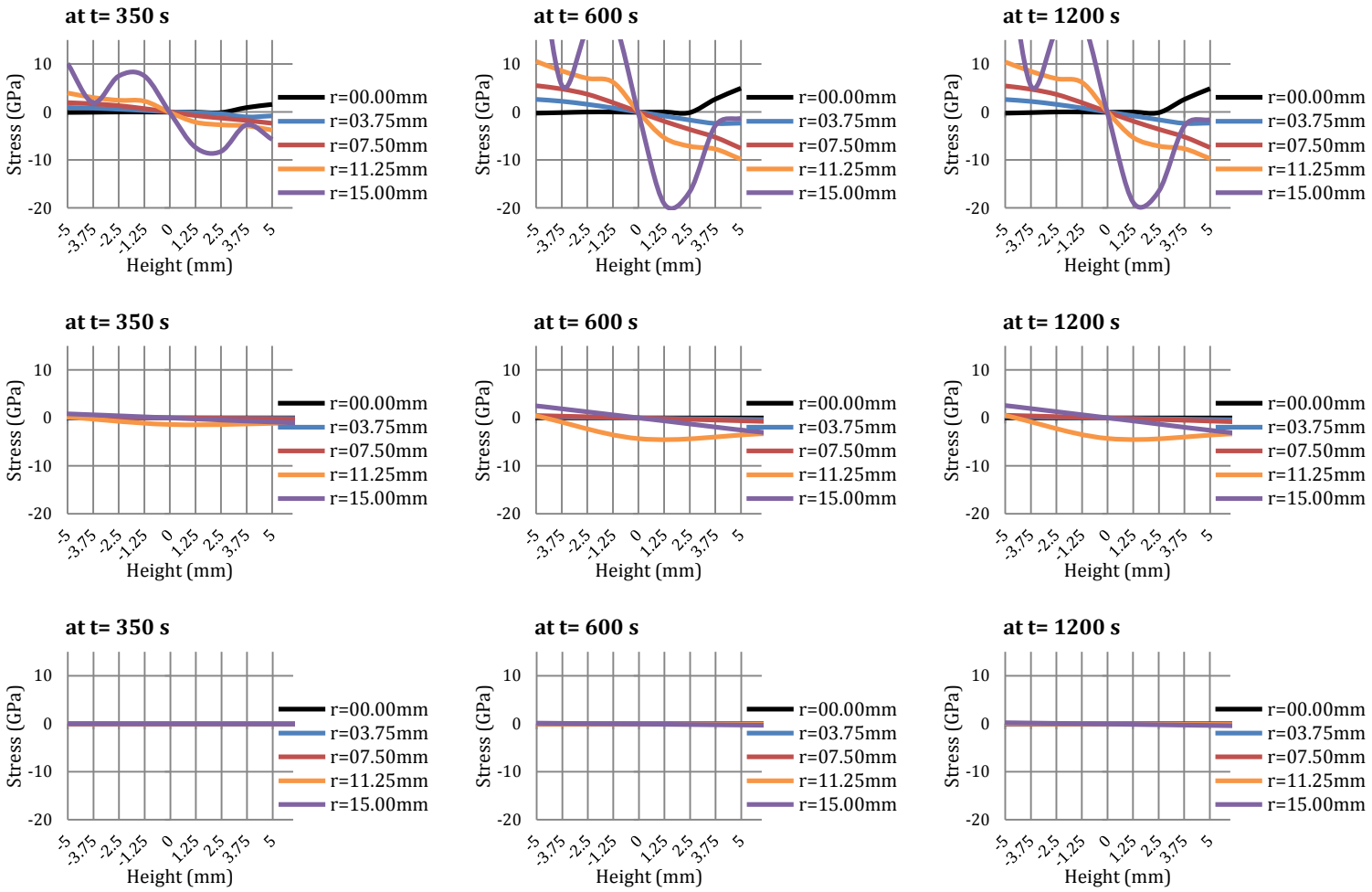

Figure 90: Height-wise shear stress distribution at different radial positions for different sample thicknesses: row1) height=10mm, row 2) height=50mm, & row 3) height=100mm

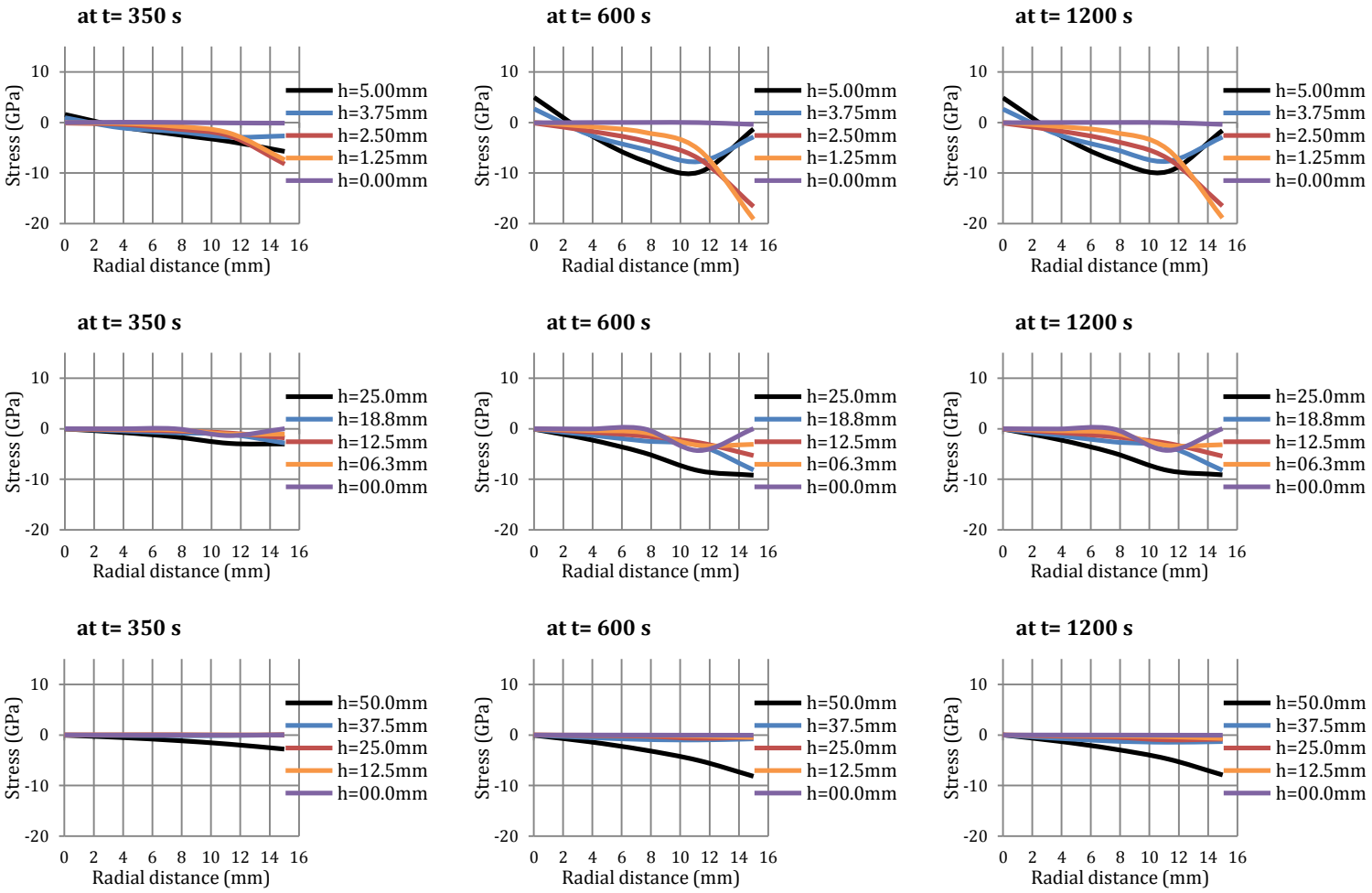

Figure 91: Radius-wise shear stress distribution at different axial positions for different sample thicknesses: row1) height=10mm, row 2) height=50mm, & row 3) height=100mm

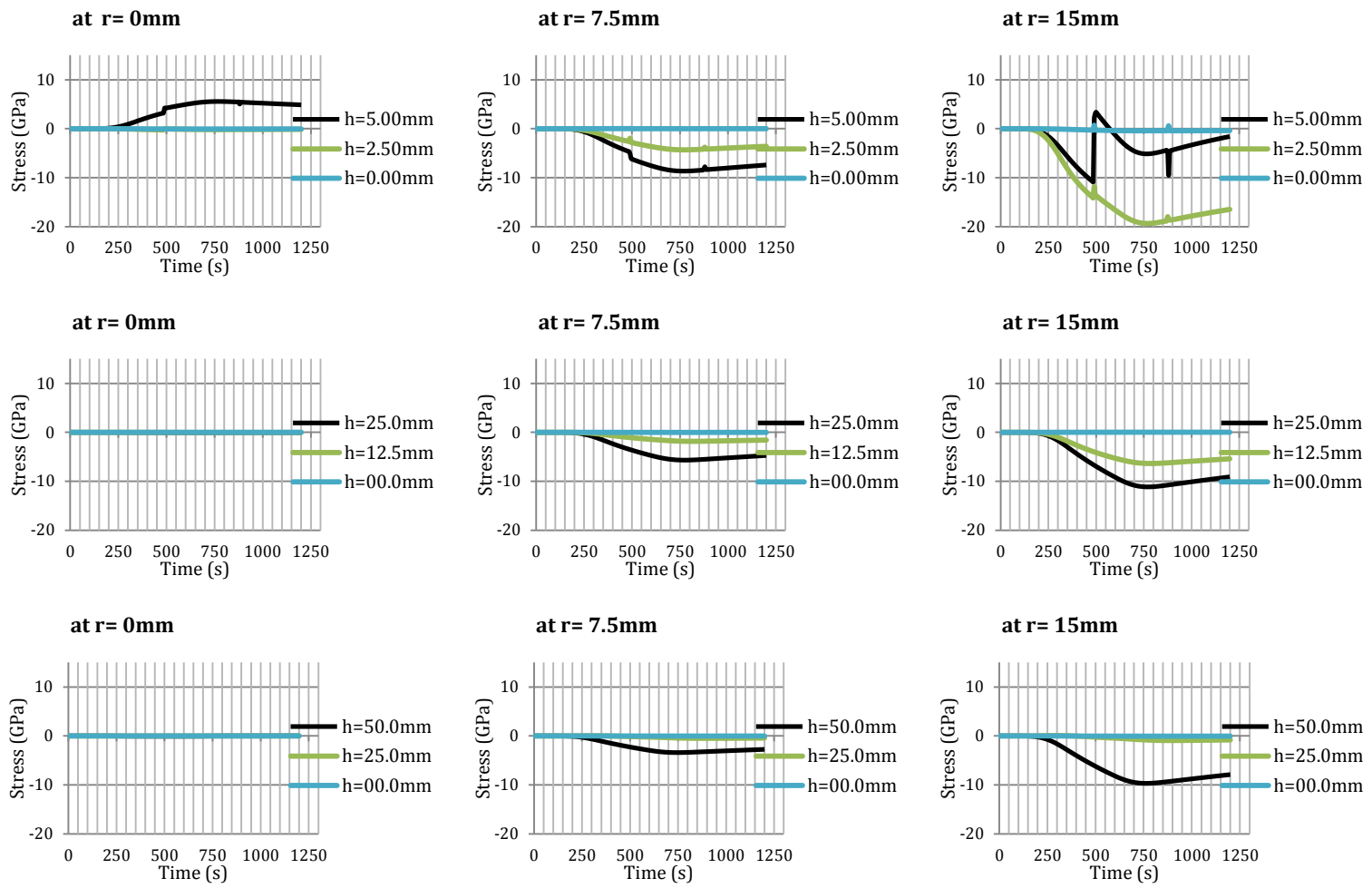

Figure 92: Shear stress evolution at different axial positions for different sample thicknesses: row1) height=10mm, row 2) height=50mm, & row 3) height=100mm

CHAPTER 6

CONCLUSIONS & RECOMMENDATIONS

In this study, a coupled electrical-thermal-mechanical Finite Element (FE) model for the Spark Plasma Sintering (SPS) process has been developed using COMSOL Multiphysics. The developed model is used to study the influence of the sintering temperature and the applied pressure on the mechanical property profile along the cross-section of sintered samples of varying aspect ratios. In this regard, the first step was the development of an electrical-thermal finite element model, which was later incorporated with factors related to sample geometry due to the existence of a coupling between the thermal and mechanical fields in the SPS process. The model was further validated using already published results in the literature.

In order to investigate the role of the intrinsic electrical conductivity of the sample on the effectiveness of the developed model, powders made up of two different types of materials have been selected for sintering. The first type is aluminum powder which is an electrical conductor and the second type is alumina powder which is regarded as an electrical insulator. Finally, the simulation results were validated by a small-scale experimental study concerning the mechanical property characterization of the sintered samples.

6.1 CONCLUSIONS

Although a simplified model has been used to build the computational scheme, inhomogeneities inside the sample were observed in current density and sintering temperature, and mechanical properties including von-Mises stress, axial stress, radial stress, and shear stresses in the sintered sample. In the case of alumina sample, a negligible amount of current flow was observed in the sample because of lower electrical conductivity. It was noticed that residual stresses developed along the sample cross-section in case of alumina are lesser in magnitude than in case of aluminum samples. However, the inhomogeneity observed in sintering temperature was observed to be much lower in case of aluminum sample than that in case of the alumina sample.

The results of the computational study indicated that the maximum radial stress is found in the top and bottom surfaces of sample for both types of materials, while the maximum temperature is found at the center of the top and bottom surfaces. However, the maximum current density in case of aluminum samples was observed at the sample edges, while the maximum axial stress was located at the quarter from the top and bottom surfaces. In case of alumina samples, the maximum von-mises stress was observed in the sample-die boundary; however, the exact location of the maximum stress was noticed to be a strong function of sample thickness. It was further observed that an increase in sample thickness resulted in a decrease in the magnitude of variation of sintering temperature as well as von Mises and radial stresses along the sample cross-section.

The experimental results of the study indicated that the hardness of both types of sintered samples decreased from a maximum value at the center of the sample to a minimum value at the sample edges.

6.2 RECOMMENDATIONS

Based on the computational and experimental results of this study, the following recommendations are proposed:

- In the stress-analysis portion of the computational scheme, it was observed that a few locations inside the sample are undergoing plastic deformation, whilst the developed model only assumes elastic deformation of the sample during the sintering process. A future model which incorporates both elastic as well as plastic deformation of the sample (depending on the magnitude of the localized stress) during the course of the sintering process is expected to yield more realistic conclusions regarding the effect of sintering parameters on the mechanical and structural properties of sintered materials.
- The simulation conducted in this study is based solely upon the built-in modeling approach in the COMSOL Multiphysics software. However, the theories of elasticity or plasticity utilized by the software to solve for the mechanical or thermal stresses as a consequence of the sintering process, cannot be identified. Hence for a deeper understanding of the effect of the sintering parameters on the material properties, the recommended approach is to develop the entire model using predefined elasticity/plasticity and heat flow theories, and then implement the developed model in a programming language like MATLAB or FORTAN.
- The model considered in this study is only applicable for simple shapes with constant cross-sections. In order to increase its computational flexibility, there exists a need to incorporate necessary modifications in the current model to render it applicable for relatively more complex geometries.

- The developed model only assumes small-sized samples, usually produced on a laboratory-scale. Hence for the model to be rendered applicable on a commercial scale, it needs to be equipped with modifications to extend the current approach towards modeling of the SPS kinetics for samples with relatively larger cross-sections than the ones considered in this study.

REFERENCES

[1] Zafar Iqbal, Abdullah Khalil, Abbas Saeed Hakeem, Nasser Al Aqeeli Nouari Saheb, "Spark Plasma Sintering of Metals and Metal Matrix Nanocomposites: A Review," *Journal of Nanomaterials*, 2012.

[2] Dat V. Quach and Manshi Ohyanagi Zuhair A. Munir, "Electric Current Activation of Sintering: A Review of the Pulsed Electric Current Sintering Process," vol. 94, no. 1, pp. 1-19, 2011.

[3] Mechanical Engineering. [Online]. http://www.mechanicalengineeringblog.com/tag/sintering/

[4] b, Roberta Licheri, Antonio Mario Locci, Alberto Cincotti, Giacomo Cao Roberto Orru` a, "Consolidation/synthesis of materials by electric current activated/assisted sintering," *Materials Science and Engineering*, pp. 127–287, 2009.

[5] Antonios Zavaliangos, Kyu C. Cho, and Robert J. Dowding Brandon McWilliams, "The Modeling of Electric-Current-Assisted Sintering to Produce Bulk Nanocrystalline Tungsten," *JOM*, vol. 58, no. 4, pp. 67-71, 2006.

[6] Jean Galy and Alicia Castro Teresa Hungria, "Spark Plasma Sintering as a Useful Technique to the Nanostructuration of Piezo-Ferroelectric Materials," *Advanced Engineering Materials*, vol. 11, no. 8, pp. 615-631, 2009.

[7] Bikramjit Basu, Koushik Biswas Devesh Tiwari, "Simulation of thermal and electric field evolution during spark plasma sintering," *Ceramics International*, vol. 35, no. 2, pp. 699–708, 2009.

[8] E. S. Chernikova A. I. Raichenko, "A mathematical model of electric heating of the porous medium using current-supplying electrode/punches," *Soviet Powder Metallurgy and Metal Ceramics*, vol. 28, no. 5, pp. 365-371 , 1989.

[9] E.S. Chernikova, E.A. Olevsky A.I. Raichenko, "The analysis of the electric heating of the WC-Co hard-alloy under under consideration of the dependence of it's characteristics on the temperature," *J. Phys. IV France*, vol. 3, no. 7, pp. 1235-1239, 1993.

[10] Michio Yoneya and Tamio Ikeshoji, "A Numerical Calculation Method Advantageous for Complex Boundary Problems -An Application to the Pulse Discharge Sintering Process.," *Materials Transactions*, vol. 42, no. 11, pp. 2165-2171, 2001.

[11] Fu Zhengyi Wang Yucheng, "Study of temperature field in spark plasma sintering,"

Materials Science and Engineering: B, vol. 90, no. 1-2, pp. 34-37, 2002.

[12] J. H. Jeon, K. H. Auh Y.T.Keum, "Computer simulation of ceramic sintering processes," *Journal of Ceramic Processing Research*, vol. 3, no. 3, pp. 195-200, 2002.

[13] H Kuramoto, T Hatayama, O Yanagisawa K Matsugi, "Temperature distribution at steady state under constant current discharge in spark sintering process of Ti and Al2O3 powders," *Journal of Materials Processing Technology*, vol. 134, no. 2, pp. 225-232, 2003.

[14] Jing Zhang, Martin Krammer, Joanna R. Groza Antonios Zavaliangos, "Temperature evolution during field activated sintering," *Materials Science and Engineering*, pp. 218-228, 2004.

[15] A. Laptev, J. Hennicke, J. Vleugels, O. Van der Biest K. Vanmeensel, "Modelling of the temperature distribution during field assisted sintering," *Acta Materialia*, pp. 4379–4388, 2005.

[16] S. Gennari, J.E. Garay, Z.A. Munir U. Anselmi-Tamburini, "Fundamental investigations on the spark plasma sintering/synthesis process II. Modeling of current and temperature distributions," *Materials Science and Engineering*, pp. 139–148, 2005.

[17] Fu Zhengyi, Wang Weimin, Zhang Jinyong Wang Yucheng, "Numerical simulation of the temperature field in sintering of TiB2-BN by SPS," *Journal of Wuhan University of Technology-Mater. Sci. Ed.*, vol. 21, no. 3, pp. 126-128, 2006.

[18] Eugene Olevsky and Ludo Froyen, "Constitutive modeling of spark-plasma sintering of conductive materials," *Scripta Materialia*, vol. 55, no. 12, pp. 1175-1178, 2006.

[19] Salvatore Grasso, Yoshio Sakka, Tetsuji Noda, Osamu Ohashi Giovanni Maizza, "Relation between microstructure, properties and spark plasma sintering (SPS) parameters of pure ultrafine WC powder," *Science and Technology of Advanced Materials*, vol. 8, pp. 644-654, 2007.

[20] K. Vanmeensel, L. Li, O. Van der Biest, J. Vleugels S.G. Huang, "Tailored sintering of VC-doped WC–Co cemented carbides by pulsed electric current sintering," *International Journal of Refractory Metals & Hard Materials*, vol. 26, no. 4, pp. 256-262, 2008.

[21] Lise Durand, Nikhil Karnatak, Sophie Le Gallet, Marc Thomas, Yannick Le Berre, Jean-Francois Castagné, Alain Couret Thomas Voisin, "Temperature control during Spark Plasma Sintering and application to up-scaling and complex shaping," *Journal of Materials Processing Technology*, vol. 213, no. 2, pp. 269-278, 2013.

[22] L. Silvaa , L. Durandb,c and M. Belleta P. Mondaleka, "Numerical Modelling of Thermal-Electrical Phenomena in Spark Plasma Sintering," in *Numiform 2010, 10th Int. Conf. on Numerical Methods in Industrial Forming Processes*, Pohang, South Korea, 2010, pp. 697-704.

[23] L. Durand, F. Ajustron, V. Bley, G. Chevallier, A. Peigney, C. Estournès A. Pavia, "Electro-thermal measurements and finite element method simulations of a spark plasma sintering device," *Journal of Materials Processing Technology*, pp. 1327–1336, 2013.

[24] Eugene A. Olevsky, Cristina Garcia-Cardona, Andrey L. Maximenko, Maria S. Yurlova, Christopher D. Haines, Darold G. Martin, Deepak Kapoor Diletta Giuntini, "Localized Overheating Phenomena and Optimization of Spark-Plasma Sintering Tooling Design," *Materials*, pp. 2612-2632, 2013.

[25] A. M. Locci, R. Orru` , and G. Cao A. Cincotti, "Modeling of SPS Apparatus: Temperature, Current and Strain Distribution with No Powders," *American Institute of Chemical Engineers*, vol. 53, no. 3, pp. 703-719, 2007.

[26] S.R. Casolco, G. Xu, J.E. Garay X. Wang, "Finite element modeling of electric current-activated sintering: The effect of coupled electrical potential, temperature and stress," *Acta Materialia*, vol. 55, no. 10, pp. 3611–3622, 2007.

[27] Brandon McWilliams and Antonios Zavaliangos, "Multi-phenomena simulation of electric field assisted sintering," *Journal of Materials Science*, vol. 43, no. 14, pp. 5031-5035, 2008.

[28] Yoshio Sakka and Giovanni Maizza Salvatore Grasso, "Pressure Effects on Temperature Distribution during Spark Plasma Sintering with Graphite Sample," *Materials Transactions*, vol. 50, no. 8, pp. 2111-2114, 2009.

[29] P. Scherrer, "Bestimmung der Grösse und der inneren Struktur von Kolloidteilchen mittels Röntgenstrahlen.," *Nachr. Ges. Wiss. Göttingen*, vol. 26, pp. 98-100, 1918.

[30] M. O. Bodunrin k. K. Alaneme, "mechanical behaviour of alumina reinforced aa6063 metal matrix composites developed by two step stir casting process," *acta technica corviniensis*, no. 3, pp. 105-110, 2013.

[31] Gendre Mathieu, Gilles Trolliard, and Alexandre Maıtre Guy Antou, "Spark plasma sintering of zirconium carbide and oxycarbide: Finite element modeling of current density, temperature, and stress distributions," vol. 24, no. 2, pp. 404-412, 2008.

[32] B. Pateyron, M. El Ganaoui and M. Kadja F. Mechighel, "Study of thermo-electrical and mechanical coupling during densification of a polycrystalline material using COMSOL," , Hannover, 2008.

[33] L. Durand, J. Galy, and A. Couret G.Mol´enat, "Temperature Control in Spark Plasma Sintering: An FEM Approach," *Journal of Metallurgy*, vol. 2010, 2010.

[34] U. Anselmi-Tamburini S. Munoz, "Temperature and stress fields evolution during spark plasma sintering processes," *Journal of Materials Science*, vol. 45, no. 23, pp. 6528-6539, 2010.

[35] Yuanyuan Li, Zhaoyao Zhou, Yangen Lai, Yongquan Ye Yi Song, "A multi-field coupled FEM model for one-step-forming process of spark plasma sintering considering local densification of powder material," *Journal of Materials Science*, vol. 46, no. 17, pp. 5645-5656, 2011.

[36] and Ludo Froyen Eugene Olevsky, "Constitutive modeling of spark-plasma sintering of conductive materials," *Scripta Materialia*, vol. 55, no. 12, pp. 1175-1178, 2006.

[37] Antonios Zavaliangos Brandon McWilliams, "Multi-phenomena simulation of electric field assisted sintering," *Journal of Materials Science*, vol. 43, no. 14, pp. 5031-5035, 2008.

[38] Veena Tikare, Terry Garino Eugene A. Olevsky, "Multi-Scale Study of Sintering: A Review," *Journal of the American Ceramic Society*, vol. 89, no. 6, pp. 1914-1922, 2006.

VITAE

Name	Muhammad Luqman
Nationality	Pakistani
Email	engrmuhammadluqman@hotmail.co.uk
Education	**Master of Science, Mechanical Engineering, March, 2014** Thesis: Multi-Physics Modeling of the Spark Plasma Sintering Process King Fahd University of Petroleum & Minerals, KSA **Bachelor of Engineering, Mechanical Engineering, Jan 2011** Final Year Project : Design and fabrication of a "Prototype Ocean Energy Converter Device" using Vortex Induced Vibration phenomenon National University of Sciences and Technology (NUST), Pakistan